Loughborough University

Mathematical Modelling of Solid Tumour Growth: A Dynamical Density Functional Theory Based Model

by

Hayder M. Al-Saedi

A thesis submitted in partial fulfilment of the requirements for the degree of Doctor of Philosophy in the

Mathematical Modelling
Department of Mathematical Sciences
Loughborough University
United Kingdom

October 2018

Supervisors: Prof. Dr. Andrew Archer and Dr. John Ward

CERTIFICATE OF ORIGINALITY

This is to certify that I am responsible for the work submitted in this thesis, that the original work is my own except as specified in acknowledgements or in footnotes, and that neither the thesis nor the original work contained therein has been submitted to this or any other institution for a degree.

Hayder Al-Saedi

ACKNOWLEDGEMENT

[All] praise is [due] to **Allah**, Lord of the worlds.

Then, I would like to express my deep and sincere gratitude to my supervisor, **Prof. Andrew Archer**, who is an extraordinary person, and has been very supportive and nice since the first day I arrived in Loughborough. Prof. Archer has made my PhD life worthwhile and unforgettable. I am very blessed to have been given the opportunity to work on a very interesting topic, mathematical modelling of cancer.

I also would like to thank the second supervisor **Dr. John Ward** who gave me great support, reassurance and valuable advices throughout the progress of this work.

Family, friends, and colleagues surely have provided support that I can never thank enough. I am very grateful with this life that I have been bestowed with, in which I have and know you all in my life.

In addition, I would also like to thank to the Iraqi ministry of higher education and scientific research, Iraqi cultural attache in London and Baghdad university for their financial support granted through doctoral scholarship.

Hayder Al-Saedi

DEDICATION

In appreciation of sacrifice,
this thesis is dedicated to my brother **Marwan**
and to all those Iraqis,
who,
sacrifice themselves to protect our country from the barbarous terrorists.

Hayder Al-Saedi

PUBLICATION

Al-Saedi, Hayder M., Andrew J. Archer, and John Ward. "Dynamical density-functional-theory-based modeling of tissue dynamics: Application to tumor growth." *Physical Review E*, vol. 98, no. 2, p. 022407, 2018.

ABSTACT

We present a theoretical framework based on an extension of dynamical density functional theory (DDFT) to describe the structure and dynamics of cells in living tissues and tumours. DDFT is a microscopic statistical mechanical theory for the time evolution of the density distribution of interacting many-particle systems. The theory accounts for cell pair-interactions, different cell types, phenotypes and cell birth and death processes (including cell division), in order to provide a biophysically consistent description of processes bridging across the scales, including the description of the tissue structure down to the level of the individual cells. Analysis of the model is presented for a single species and a two-species cases, the latter describing competition between a cancerous and healthy cells. In suitable parameter regimes, model results are consistent with biological observations. Of particular note, divergent tumour growth behaviour, mirroring metastatic and benign growth characteristics, are shown to be dependent on the cell pair-interaction parameters.

Contents

1 Introduction **1**

1.1 Introduction 1

1.2 Mathematical Growth Models 4

1.2.1 Microscopic Models 5

1.2.2 Macroscopic Models 5

1.2.3 Dynamic Density Functional Theory Models 6

1.3 Further Classification of Tumour Growth 7

1.3.1 Avascular Growth/Solid Tumour 7

1.3.2 Tumour-Induced Angiogenesis 8

1.3.3 Vascular Growth/ Invasive Tumour 8

1.3.4 Diffusion based Models 9

1.3.5 Mechanical Models 9

2 Literature Review on Tumour Growth: The Contribution of Mathematical Modelling **11**

2.1 Introduction 11

2.2 Models of tumour growth by diffusion 12

2.3 Models of avascular tumours growth 14

2.3.1 Continuum Models 15

2.3.2 Discrete Models 15

2.4 Models of tumour-induced angiogenesis 16

2.4.1 Continuum Models 17

2.4.2 Discrete Models 18

2.5 Models of vascular tumours and metastasis 18

2.5.1 Models of vascular tumours 19

2.5.2 Invasion and metastasis 20

2.6 Models of cell-cell interactions 22

3 Density Functional Theory (DFT) 25
3.1 Introduction 25
3.2 Thermodynamics of homogeneous fluids 26
3.3 Thermodynamics of inhomogeneous fluids 29
3.4 Microscopic statistical mechanical origin of DFT 34

4 Dynamical Density Functional Theory (DDFT) 37
4.1 Introduction 37
4.2 DDFT of solid tumour growth 39
4.2.1 Langevin equation 40
4.2.2 Smoluchowski equation 41
4.2.3 From Smoluchowski to DDFT 42
4.3 Cell birth/death processes 46
4.4 Model Formulation 47

5 Mathematical Model for a single species of cells 51
5.1 Introduction 51
5.2 Scaling and nondimensionalisation 53
5.2.1 Nondimensionalisation for the system of ODEs 53
5.2.2 Nondimensionalisation of the full model 55
5.3 Parameter values 57
5.3.1 Standard parameter set 59
5.4 Linear stability analysis 61
5.5 Numerical results for the cell evolution 65
5.5.1 Evaluating the convolution integral 66
5.5.2 Method of lines 67
5.5.3 Euler method 68
5.5.4 The Adams Methods 74

6 Model including competition between cancer and healthy cells 85
6.1 Introduction 85
6.2 Nondimensionalisation 89
6.3 Parameter values 92

6.4 Linear stability analysis for two species system 95
6.5 Results for cancer invading healthy tissue 101
6.5.1 Results with a homogeneous nutrient source 101
6.5.2 Results with inhomogeneous nutrient sources 118
6.5.3 A few cancer cells dispersed throughout healthy tissue 126
6.6 The effect of varying $\beta\varepsilon_{12}$ on the results 132

7 Model including haptotaxis **141**
7.1 Introduction 141
7.2 Mathematical model 142
7.3 Linear stability analysis for the system 144
7.3.1 No cell-cell interactions 148
7.3.2 Full model 149
7.4 Conclusion 151

8 Conclusions and future works **155**
8.1 Conclusions 155
8.2 Future works 158

Appendix A The Ito Calculus **161**
A.1 The Ito stochastic differential equations 161
A.2 The Ito formula 162
A.3 The Fokker–Plank Equation 163

Appendix B The Smoluchowski equation **165**

CHAPTER 1

INTRODUCTION

1.1 Introduction

Cancer is a disease that may be viewed as a complex system whose dynamics and growth results from nonlinear processes coupled across a wide range of spatiotemporal scales. Cancer is recognised as one of the major causes of premature death, soon to overtake heart diseases as the leading cause in the developed nations [1]. At current rates, in the USA a third of women and half of men will develop a cancer at some point in their life [2]. A recent report by the World Health Organisation's International Agency for Research on Cancer (IARC) [3] states that North America leads the world in the rate of cancers diagnosed in adults, followed closely by Western Europe, Australia and New Zealand [4]. In Britain, for example, according to Imperial Cancer Research Fund, one in three are expected to develop the disease over their lifetimes, with a likely increase to one in two in the near future based

on the trends at that time [5]. Similarly, in Australia it has been predicted that a third of men and a quarter of women will be affected by cancer by the age of 75 [4]. Though significant progress has been made in cancer treatment in recent decades, much research is still required in order to control all forms of the disease.

The human body is made up of order 10^{13} cells [6]. Genetic mutations are frequent, but most affected cells die by apoptosis (programmed cells death) which is a regulated process involving the systematic dismantling of cells into smaller bodies and then are removed by the immune system. However, a few may escape the regulatory process to produce an abnormally growing colony that in time recruits its own vascular system (via angiogenesis) and form a cancer. A tumour is a mass of tissue formed as a result of abnormal and uncontrolled cellular proliferation, the growth of which continues indefinitely and regardless of the mechanisms that control normal cellular proliferation [7]. Tumour growth varies depending on type, location and circumstance. Solid tumours can be develop to be either benign or malignant [8]. Cells in the former case are highly differentiated, usually uniform, grow slowly, and neither invade the adjacent tissues nor give rise to metastases elsewhere in the body. They proliferate locally, but their continued growth can cause atrophy and disappearance of cells of neighbouring healthy tissues due to the mechanical forces applied. Frequently, they are completely enclosed in a protective capsule of tissue. A benign tumour may remain in situ for years without causing ill effects and if detected it is easily removed by surgery. On the other hand, malignant tumours are less well differentiated and their cells tend to grow rapidly and show differences in size and shape. As they develop, individual cells are able to escape the main tumour mass (metastasis) and colonise elsewhere in the body; it is these cells that give rise to the greatest clinical concern. Malignant tumours can be removed by surgery if they are

recognised before the stage of metastasis [7]. Table 1.1 summarise the differences between the benign and malignant tumours.

Table 1.1: Contrasting Differences between Benign and Malignant Tumours

Features	Benign	Malignant
Pattern	Uniform	Not uniform
Growth rate	Slow	Rapid
Periphery	Encapsulated	Absence of encapsulation
Metastases	Never occur	Can occur
Treatment	Removed by surgery	Varied

Despite major scientific, medical and technology over the last few decades, a fundamental gap that is currently hampering progress in individualised cancer care is the extrapolation of patient-specific micro scale quantitative information into formulations of therapeutic and intervention strategies at clinically relevant scales (e.g., organ scales).

Tumour growth modelling is the study of the complex dynamics of cancer progression using mathematical descriptions. The internal dynamics of cancerous cells, their interactions with each other and with healthy tissue, nutrition and oxygen transport, extracellular matrix (ECM), properties of vascularisation, vascular network, chemicals signals secreted by tumour and host cells, properties of the underlying tissue are amongst the factors modelled using dynamical equations. These equations rely on biological and clinical observations coming from different sources at different scales. Experimental observations are key to create models depicting the tumour growth process precisely.

Mathematical growth models give important information for both clinical and specialists in oncology. Creating a mathematical framework that combines experimental results lead to enhanced understanding of the underlying mechanisms of

tumour growth. Experiments and simulations enable the impact of different treatments on cancerous cells to be assessed and can lead to improved treatments or suggestions for new ones. Personalised models adapted to patient specific cases, could in the future be used in therapy planning, e.g. model prediction can indicate focussed application of irradiation to minimise side effects in combination with optimally timed chemotherapy.

1.2 Mathematical Growth Models

Mathematical modelling of cells growth in tumours is one of the oldest and best developed topics in biomathematics [9]. Mathematical modelling of tumour growth can be classified into two broad groups: microscopic models and macroscopic models. The main difference between these two classes is the scale of observations they are trying to clarify and depict. Microscopic models focus on the cellular microscopic scale, often connecting to *in vitro* (in laboratory vessel) and *in vivo* (occur with a living organism) experiments. As a result, they formulate the growth phenomena at this scale. Macroscopic models on the other hand, concentrate on describing structures that are at the naturally visible scale like the ones provided by medical images. They formulate the average behaviour of tumour cells and their interactions with underlying tissue structures, which are visible at this scale of observation (grey matter, white matter, bones, etc). These models try to describe the behaviour of the tumour, consisting of millions of cells as a whole [4].

1.2.1 Microscopic Models

Microscopic growth models aim to describe the tumour growth process at the cellular level based on observations at this level from microscopy on biopsy samples and other such experiments. They take into account physical and chemical interactions between cancer cells, the extracellular matrix and the healthy cells. Mechanical phenomenon like pressure, cohesion and adhesion forces are often included in these descriptions. Mathematical models for these are usually very detailed because they try to take into account all the observed factors. As a consequence, the number of parameters in such models is very high. From the technical point of view, formulating such microscopic models requires a large variety of mathematical methods. The most commonly used are discrete stochastic models, such as cellular automata or agent based models, that are analysed through competition.

1.2.2 Macroscopic Models

Observations at the macroscopic scale consist of medical images like computed tomography scans (CT), magnetic resonance images (MRI) and MR diffusion tensor images (MR-DTI). Since the resolution of these imaging processes is limited, typically around $1mm \times 1mm \times 1mm$ in the best case, observable features are limited. Mathematical models at the macro-scale try to formulate the tumour growth using the observations coming from this scale. For this reason, these models include fewer factors and are mathematically simpler than the microscopic models discussed in Sec.1.2.1. From the mathematical point of view, all macroscopic models are mostly continuum formulations based on a continuous local density or proportion of tumour cells. As a result, these types of model formulations contain several ordinary and/or

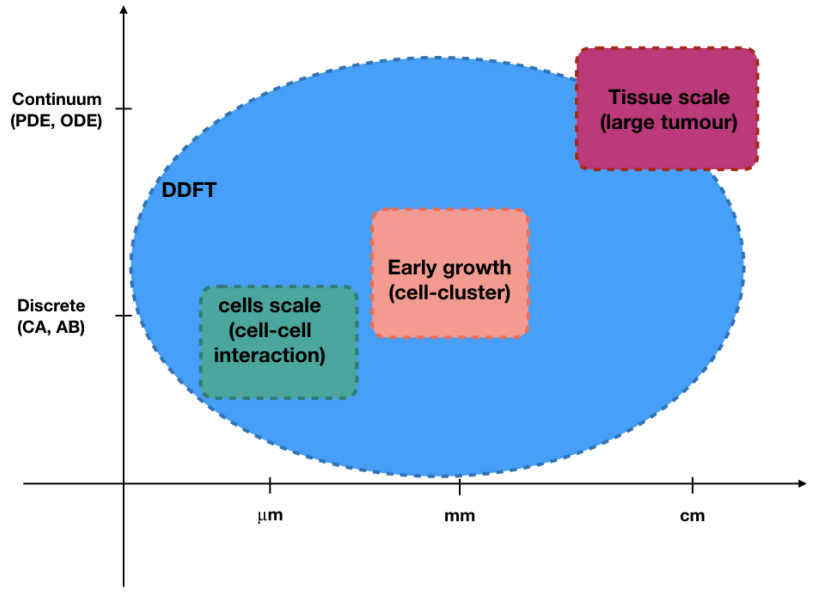

Figure 1.1: Diagram illustrating various aspects of different mathematical modelling approaches of tumour growth.

partial differential equations to describe the growth process [10, 11].

1.2.3 Dynamic Density Functional Theory Models

To help bridge this gap between micro and macro scale modelling, we propose a mathematical approach based on Dynamic Density Functional Theory (DDFT) [12], which provides a mesoscale continuum framework directly derived from a stochastic, discrete model as shown in Fig.1.1. Unlike standard mean-field models, the DDFT approach accounts for correlations and is able to describe the density distribution at the microscopic (cellular) level [12, 13]. We extend the approach to model the spatiotemporal dynamics of multicellular systems by including cell type and birth/death processes, which are major features of biological tissues. Whilst built on the principle of discrete statistical models, the approach leads to a system of integro-partial differential equations and thus makes available a greater range of mathematical tools

for their study.

1.3 Further Classification of Tumour Growth

Further classification within these groups can be made based on the tumour growth dynamics and mechanisms, such as diffusion, tumour cell invasion and mechanical properties and the stage of the tumour growth being analysed (i.e. avascular growth, angiogenesis or vascular growth).

1.3.1 Avascular Growth/Solid Tumour

Avascular growth (tumours without blood vessels) corresponds to the stage where the growth process is mostly governed by the proliferation of the tumour cells. In this stage the tumour takes the form of a solid mass, which is growing by mitosis (i.e. growth by individual cells splitting to create two identical copies of the original cell). Although not totally known, it is thought that at this stage there is no invasion of the healthy tissue. Furthermore the interactions between tumour cells and the healthy tissue are also thought to be limited [4]. The tumour cannot grow indefinitely in the avascular stage because as the tumour mass grows, less and less nutrition is available for the cells found at the centre of the avascular mass. As a result, necrosis begins, whereby tumour cells that are not getting enough nutrition die, and only cells on the outer perimeter of the tumour continue to proliferate. At some point necrosis and the proliferation balance each other out and the avascular tumour reaches a limit size, which is typically around 1–3 mm in diameter [14]. The building blocks for mathematical models of these are generally coupled ordinary and partial differential equations, such as population growth and reaction-diffusion models [15].

1.3.2 Tumour-Induced Angiogenesis

This is the stage where tumour cells in the avascular mass modify the existing vascular structure to make new blood vessels to feed the growing tumour. Through this process the tumour can overcome its size limit, grow much faster, and invade the surrounding tissue. Due to this crucial role of angiogenesis, the underlying mechanisms of this stage have captured attention and many models have been proposed. Tumour induced angiogenesis is a very complex process including lots of chemical and mechanical phenomena, which have not yet been totally understood. The building blocks of mathematical models for these processes are stochastic differential equations [16–19].

1.3.3 Vascular Growth/ Invasive Tumour

The intricacy of the tumour growth in this stage is higher because there are several processes going on at the same time. In addition to the cellular and chemical interactions going on as in the first two stages, tumour cells start to invade the surrounding tissue via mechanisms that are not clearly known yet. At this stage, parts of the tumour becomes diffusive and is not considered to be solid anymore. While the difference between cancerous and healthy regions is clear in the avascular stage, this difference vanishes during the vascular growth because tumour cells move towards healthy regions. Vessels inside the vascular tumour might have been formed by angiogenesis or the tumour might have grown around an existing vessel, as in the case of tumour cords. Unlike avascular tumours, the source of nutrition is not limited to diffusion from the perimeter. Thus, the formation of necrotic regions is much more complex, if they exist at all. For the same reasons, vascular tumours are not compact masses of cancerous cells, they do not have a size limit and can grow

indefinitely [20].

1.3.4 Diffusion based Models

Almost all diffusive macroscopic models use the reaction-diffusion formalism. This formalism models the invasive tumour by adding a diffusion term to simple solid tumour growth models, which describe the proliferation of cells [10]. The central building block of this approach is a partial differential equation (PDE) of the following form

$$\frac{\partial \rho}{\partial t} = \nabla \cdot (D \nabla \rho) + R(\rho, t), \tag{1.3.1}$$

with the Neumann boundary condition

$$\mathbf{n} \cdot \nabla \rho = 0, \tag{1.3.2}$$

where ρ is the tumour cell density, D is the diffusion tensor of tumour cells and $R(\rho, t)$ is the growth (or reaction) term. This equation incorporates two different characteristics of the tumour growth in the two terms: diffusion and proliferation. The first term on the right hand side describes the invasion of tumour cells by means of (a perhaps directed) Brownian motion, which is characterised by the diffusion tensor D. The second term in the equation, $R(\rho, t)$, describes the proliferation of tumour cells. The second equation represents a no flux boundary condition and $\mathbf{n}$ is the normal vector to the boundary [21].

1.3.5 Mechanical Models

Mechanical models concentrate on the mass displacement effects of the tumour growth on the surrounding structures. When the tumour grows, surrounding tissues

are deformed. This deformation is described by coupling the pressure caused by the change in tumour density with the material characteristics of the organ structures. Most of the models use rather a simpler formulation consisting only of mitosis causing an outward pressure. They focus on mechanical interaction between a growing tumour and the tissue [22].

This thesis is laid out as follows: In the next chapter, we discuss the relevant literature on the above topics in more detail. Chapter 3 gives an introduction to density functional theory (DFT), which is the basis of our model for the density distribution of the particles (i.e. cells). In chapter 4 we present a dynamical density functional theory (DDFT) of solid tumour growth with application of cell birth/death processes. In chapter 5, we present results from the DDFT for a single species of cells, including a linear stability analysis and some typical simulation results are discussed in details. The model presented in chapter 5 is further extended in chapter 6 in order to describe the competition between cancer cells and healthy cells. We also present a linear stability analysis and typical results from this model. In chapter 7 we present a preliminary analysis of a model to describe the haptotaxis process of cell movement in response to gradients in the extracellular matrix (ECM). Finally, in chapter 8, we present our conclusions and suggestions future works.

CHAPTER 2

LITERATURE REVIEW ON TUMOUR GROWTH: THE CONTRIBUTION OF MATHEMATICAL MODELLING

2.1 Introduction

Addressing the challenges posed by cancer, Perumpanani compares the research community taking these challenges to a military action in the war and adds that this has resulted in recent years in an expansion of our understanding of cancer [5]. Interestingly, Alberts et al. [23] observe that the emphasis given to cancer research has contributed greatly to a much wider area of medical knowledge than that of cancer alone, explaining that the effort to eradicate cancer has led to many fundamental discoveries in cell biology. Nevertheless, the study of cancer is not new.

Ward, in [24] asserts that various texts of ancient Greece, Egypt and Rome make clear that the early physicians were well aware of the nature of cancer and were able to make a correct diagnosis and perform successful therapy.

Clearly the study of tumour growth and the development of anti-cancer therapies have significant potential to enhance quality of life and increase life expectancies, which may, in turn, yield extensive financial and social advantages [4]. Experimentalists and clinicians are becoming increasingly aware of the role of mathematical modelling as a new way forward, recognising that current medical techniques and experimental approaches are often unable to distinguish between various possible mechanisms underlying important aspects of tumour growth [25].

The forthcoming literature review discusses some of the important mathematical contributions to the study of tumour growth. It gives a brief history, presenting some of the most notable mathematical models and their relationship to experimental studies, and illustrating how the field of cancer research has evolved due to these interactions between theoretical and experimental approaches.

2.2 Models of tumour growth by diffusion

The earliest mathematical studies in the early 1950s of tumours neglected the diffusion processes and focused purely on growth dynamics. Mayneord [26] in 1931, for instance, noticed that in the final stage of growth the tumours grew linearly with time through his experiments on the effects of X-radiations on the growth of Jensen's rat sarcoma. A perception corroborated by the study of spontaneous carcinomas of the mouse reported by Haddow [27] some six years later in 1938.

The diffusion processes would later become a crucial part of tumour models. Hill

was the one of the first work on diffusion in tissues in 1928 [28]. He set the scene for many mathematical models of solid tumours. Hill understood that the diffusion of dissolved substances through cells and tissues is a determining factor in a myriad of vital processes, for example, the diffusion of oxygen into a solid tumour where it is consumed by metabolic processes.

As experimental studies on radiotherapy continued, many researchers became interested in the role of hypoxic (oxygen deprived) tumour cells in the radiosensitivity of tumours, starting with the irradiation investigations of tumour slices in vitro by Cramer [29] and the in vivo studies culminating in an influential paper by Gray et al. [30], which first guided clinicians to try radiotherapy at increased oxygen pressures.

Several explanations have been advanced for the underlying mechanism of exponential retardation in tumour growth rates. While Laird [31] argued that "considering the data available at the present time, it seems likely that the observed deceleration of tumour growth is due at least in part to an actual increase in the mean generation time during tumour growth", Mayneord [26] in 1932 has shown that such a retardation could be achieved by the formation of a necrotic (messy cells death) region in the centre of a tumour, gradually reducing the region of active growth to a thin shell at the tumour surface. Burton [21] in 1966 favoured Mayneord's explanation, modelling the effects of a decreasing growth fraction, while the mitotic rate of viable cells stayed constant. The hypothesis of Mayneod is confirmed by Roose et al. [32] in 2007.

2.3 Models of avascular tumours growth

This section aims to describe the current state of mathematical modelling of avascular tumour growth. The *in vitro* version of these tumours, i.e. multi-cell spherical growth, can be readily produced and widely used in experimental studies. They are reproducible and are relatively easy to work with. Consequently they are easier to model than vascular tumours.

The study of avascular tumours continues to make a fundamental contribution to mathematical models devoted to solid tumour growth, for example, the sequence of papers by Ward and King [24,33–35] have made a worthy contribution to the recent literature on avascular tumour growth and are often cited. The first paper [24] presented a system of non-linear partial differential equations to model, within a continuum, the evolution of living and dead cells (depending on the concentration of a generic nutrient). The birth and death processes are assumed to create local volume change, generating movement which can be described by a velocity field, the aim being to make predictions about tumour heterogeneity and growth, without making any a priori assumptions about the spatial structure of the tumour. Though the model successfully predicts much of the growth of the pattern, it does not predict growth saturation.

An extension to the model was proposed [33] in order to permit a consideration of growth saturation by incorporating a necrotic volume loss by diffusion of extracellular material out of the tumour.

We will now present an overview of other models in this area, treating separately continuum and discrete models.

2.3.1 Continuum Models

In tumour modelling these models consider the interactions between the cell density and one or more chemical species that provide nutrients, typically resulting in a system of reaction-diffusion-advection equations. The first paper to propose that incorporated diffusion and nutrient consumption might be limiting solid tumor growth was by Burton [21], and since then a large number of studies have described the spatiotemporal interactions between tumour cells and nutrients [36–39]; whilst most of these considered one specie, Casciari et al. [40] examines the interaction of tumour cells with oxygen, glucose, lactate, carbon dioxide, chloride and pH. Early models of nutrient-limited tumour growth calculated the nutrient concentration profiles as a function of tumour spheroid radius that was changing due to the rate of cell proliferation [21, 36, 39, 41–43]. The later models have incorporated differing degrees of complexity for cell movement. For example, cells can be considered to move either via advection [24, 44–46], actively via diffusion [47–51] or via diffusion and chemotaxis [46, 47, 52].

2.3.2 Discrete Models

In contrast to the continuum models, discrete models can deal with the individual cells more efficiently so that it can include more details about cell movement and interaction with the surrounding tissues. With the huge advances in biotechnology, a lot of information on phenomena occurring on a single cell scale are presently accessible. This, combined with *in vitro* experiments using high power confocal or multi-photon laser microscopy that enables tracking of individual cells in space and time, has brought about the possibility of modelling single-cell-scale phenomena and then using the techniques of upscaling to obtain information about the large-

scale phenomena of tumour growth. There are several upscaling techniques; the most popular ones are cellular automata [53–60], lattice Boltzmann methods [61,62], agent based [63, 64], extended Potts [65] and the stochastic (Markov chain combined with Fokker–Planck equations) approach [64, 66–68, 68]. As in the case of phase-averaged continuum models discussed in the previous section, the main difficulty with the discrete cell-based models lies in their parameterisation, and thus these models are more appropriate for giving qualitative insights, instead of detailed quantitative predictions.

2.4 Models of tumour-induced angiogenesis

Initially, solid tumours are avascular and depend on diffusion from adjacent vessels to supply them with oxygen and nutrients and to remove waste products. As the tumour grows, nutrient demand increases so that eventually the flux of nutrients through the surface of the tumour is not enough to supply the whole mass of cells. In time, a necrotic centre of dead cells emerges in the middle and ultimately limits the tumour growth to a steady state size of 1–3 mm, whereby the number of dying cells counterbalances the number of proliferating cells [32]. Growth can resume only if the tumour becomes vascularised. A response of cells, including tumour cells to hypoxia (the reduction of oxygen levels) is the expression of genes that code for signalling molecules, e.g. growth factors, primarily vascular endothelial growth factor (VEGF), and basic fibroblast growth factor (bFGF; also called FGF-2) that are used to induce nearby vessels to grow new capillaries that infiltrate and ultimately vascularise the tumour through a process called angiogenesis [69]. Thus angiogenesis is the essential condition for cancer development and clinical

significance, and understanding the mechanisms that control it will provide the basis for rational therapeutic interventions.

Mathematical models of tumour-induced angiogenesis fall into two main categories: (i) continuum models that treat the endothelial cell EC density and chemical species as continuous variables that evolve according to a reaction-diffusion system, (ii) discrete, cell-based models in which cells are treated as units and move, grow, and divide according to prescribed rules.

2.4.1 Continuum Models

The first model that addresses the question of site location is due to Orme and Chaplain [14]. This model is based on reaction-diffusion and haptotaxis mechanisms and invokes equations on a one-dimensional domain, which are coupled nonlinearly with the set of mass balances describing selected factors in the endothelial cells (EC) environment. In [70] the site is determined from the interaction of ECs and ECM, while in [71] the dynamics of angiostatin, pericytes, and macrophages are included.

Anderson and Chaplain in [72] developed a one-dimensional continuum model to describe the dynamics of the endothelial cells density, migrating toward a tumour and forming angiogenesis in response to a specific chemical signal, the tumour angiogenic factors (TAF). Later, Anderson and Chaplain extended the one-dimensional work in [72] to two space dimensions in order to obtain a more realistic picture of the angiogenic process [73, 74].

Holmes and Sleeman in [75] developed a mechanochemical model to study the role of the extracellular matrix in a more direct way by including the dynamics of the ECM displacement in the model and by considering the ECM to be an active participant in the process. The model represents an attempt to actively investigate

the role of the extracellular matrix in the angiogenic process.

2.4.2 Discrete Models

One of the first and most successful models to approach the problem using a discrete framework was that of Stokes and Lauffenburger in [76]. This model is discrete in the sense that it treats buds individually and tracks the motion of the tip of a growing bud in two space dimensions. Each bud is characterised by the position and velocity of its tip cell at a given point in time, and the average density of buds is computed. The evolution of the tip velocity is governed by a stochastic differential equation that comprises a viscous damping term, a white noise term to model random motion of the cells, and a chemotactic component.

Anderson & Chaplain [73] and Chaplain [74] used an alternative approach. They started by discretising a two dimensional continuum using finite differences and explicit Euler and they used this discrete form to assign probabilities of cells moving to different grid points at the next time step. These probabilities obviously contain contributions from diffusion, chemotaxis, and haptotaxis.

2.5 Models of vascular tumours and metastasis

Despite the fact that some research deals with a vascular growth and metastatic tumour as different types of tumours, in this study, we consider that the metastasis tumour is an advanced stage from the vascular tumours.

2.5.1 Models of vascular tumours

A number of noteworthy attempts have been made to model vascular tumour growth, though notably less in number when compared with models of avascular tumour growth. Byrne and Chaplain [18] developed a model of non-necrotic tumour growth which studies the roles of nutrients and growth-inhibitory factors being supplied to tumour cells by both diffusion and a source term representing blood-tissue transfer by the vasculature. This was an important contribution to the theoretical study of growth inhibition.

Hahnfeldt et al. [77], on the other hand, developed a quantitative theory of vascular tumour growth and treatment response under angiogenic stimulator and inhibitor control by investigating the effects of the angiogenic inhibitors endostatin, angiostatin on tumour growth dynamics. Angiostatin is a naturally occurring protein found in several animal species, including humans. It is an endogenous angiogenesis inhibitor, and it is currently undergoing clinical trials for its use in anticancer therapy. In addition, the analysis offered a ranking of the relative effectiveness of the inhibitors.

In contrast to many other studies, Breward et al. [78, 79] proposed a model of the vascular tumour, considering the interactions between a compliant vessel and the live and dead tumour cells in its neighbourhood. Here, the oxygen levels in the tumor tissue depended on the spacing of the blood vessels as well as their thickness, with larger vessels supplying greater levels of oxygen.

A poroelastic description of a vascular tumour was developed by Netti et al. [80] such that microscopic and macroscopic descriptions of transvascular and interstitial fluid movement were united, with a view to providing a theoretical tool to complement experimental investigations of drug delivery in solid tumours.

2.5.2 Invasion and metastasis

Ruoslahti [81] explained that metastasis, the spread of cancer to distant sites in the body, is in fact what makes cancer so deadly. A surgeon can remove a primary tumour relatively easily, but a cancer that has divided usually reaches so many places that surgery alone cannot be a cure. For that reason, he concludes, metastasis and the invasion of normal tissue by cancer cells are the hallmarks of malignancy.

It was not until the 1970s that quantitative experimental work and mathematical models were proposed to elucidate the dynamics of the metastatic process. An experimental model was first developed by Liotta et al. [82]. In a later study, Liotta et al. [83] confirmed the presence of tumour cells (both singly and in clumps) in the perfusate shortly after the appearance of the tumour vascular network, with the concentration of tumour cells increasing quite rapidly initially and later diminishing.

2.5.2.1 Continuum Models

Orme and Chaplain [14] extended the study of Liotta et al. [84] to consider, in more detail, the interactions between tumour cells and capillary vessels. Whereas the earlier work had proposed coupled diffusion equations with source and sink terms to describe the density of the tumour cells and vessel surface areas, the new model assumed that tumour cells react to the presence of blood vessels in a similar manner to that of 'taxis', so that tumour cells move up a gradient of capillary vessels. Moreover, a crucial aspect of the model was the assumption that a necrotic core develops as a consequence of the overcrowding of tumour cells and eventual collapse of blood vessels, in contrast to the hypothesis by Liotta et al. [84] that necrosis occurs due to the inability of the process of neovascularisation (new blood vessel formation in abnormal tissue) to keep pace with tumour cell proliferation.

The theoretical studies by Perumpanani and co-workers [5, 85, 86] have made a significant contribution to the recent mathematical literature pertaining to malignant invasion. These models followed a more detailed phenomenological understanding of tumour cell invasion by incorporating mathematical descriptions of biological processes ignored from the majority of previous studies. They also contrasted with previous mathematical models of cell motility which focused on the angiogenesis.

In the 1990s, Gatenby [87, 88], Gatenby and Gawlinski [89] and Webb et al. [90] wrote a number of important mathematical papers on tumour invasion which contrasted quite markedly with the former publications, investigating alternative mechanistic bases for experimentally-observed behaviour.

2.5.2.2 Discrete Models

Cellular automata for multiscale modelling of tumour growth and invasion has been used to a large extent, for example, in models by Alarcon et al. [91,92]; Betteridge et al. [93]; Byrne et al. [94, 95]; Deroulers et al. [96]. In their model Alarcon et al. [91] couple cell growth to the environmental conditions and intracellular processes. They used a hybrid cellular automaton as a basic theoretical framework to combine and couple models from the tissue scale, such as vascular structural adaptation, to the intracellular scale, such as the cell cycle.

Agent-based models are also widely used in multi scale cancer modelling. Zhang et al. [97] present a 3-dimensional multi scale agent-based model to simulate the cellular decision process to either proliferate or migrate in the context of brain tumours. The same cell modelling technique used in Athale et al. [98] is adopted and each 3-dimensional fixed grid point can be occupied by only one cell at each time step.

Rubenstein and Kaufman [99] use the Potts model for their multi scale modelling of glioma invasion, cell adhesion and cell-matrix adhesion.

2.6 Models of cell-cell interactions

Much work has gone into developing mathematical models of cancers. Of particular interest here is the spatiotemporal dynamics, which can be described using continuum, discrete or hybrid models. Continuum approaches usually result in a system of coupled partial differential equations and have been used to describe avascular growth [21, 24, 36, 100–103], vascular growth [11, 14, 20, 21, 78], angiogenesis [16, 18, 19] and treatment [104–106]. Most of these consider the overall growth as being dependent on nutrient(s) that diffuses in from the outside, whilst more sophisticated extensions of these models treat the tumour as a poro-viscous [81–83] or poro-elastic [18, 20, 37, 107] structure. In such models the cell-cell interactions enter via coefficients in the mass conservation terms and (usually) linear constitutive relations describing the macroscale material properties of the tissue, rather than via any genuine microscale description of the interaction between cells. Of course, the advantage of such models is that they are amenable to analytical techniques and relatively small-scale computation. However, the microscopic cell-cell interactions play a crucial role in the development and function of multicellular organisms [108], so it is desirable to incorporate cell-cell interaction effects in the modelling. These interactions determine the structural integrity of tissue and allow cells to communicate with each other in response to changes in their micro-environment, which is essential for the survival of the cells and the host. Such communications include that from physical contact and chemical signals, transported directly through gap

junctions between cells or by passive diffusion. Some of these aspects can differ between healthy and cancer cells, so modelling these differences can be important.

Greater detail of the cell-cell interactions are routinely incorporated in discrete models for tumour growth, such as cellular-automata [109–112], agent-based models [113–115] and Potts models [112, 116–118]. In these, cells are described at a microscopic level as entities that move and respond to neighbours via a set of biologically motivated rules. Simulating the action of a group of many of these cells then gives the evolution of a tumour on the macroscale. Cellular automata models consists of a regular grid of cells, each in one of a finite number of states, such as 'on' or 'off'. In agent based models their actions typically follow discrete event cues or a sequential schedule of interactions, rather than simultaneously performing actions at constant time-steps, as in cellular automata models. Potts type models are able to incorporate how internal elements of the cells respond to one another based on certain characteristics that each possess [110, 115, 117]. Though discrete models are good for incorporating the biology and physics of cell-cell interactions, they are designed for computation and are generally difficult to study analytically.

A continuum theory that also incorporates the cell-cell interactions at a microscopic level was proposed (but not analysed) by Chauviere and his group in [119]. The central idea is to base the model on dynamical density functional theory (DDFT) [12, 13, 120], which is a theory for the dynamics of interacting Brownian (colloidal) particles, able to describe the time evolution of variations of the density distribution of the particles over length scales comparable with the size of the individual particles. This is the approach we extend and implement in this thesis. DDFT provides a systematic means of obtaining a continuum description of the density distribution of the cells that also incorporates a description of the microscale interactions

between cells. One can solve the DDFT numerically for large enough systems to enable a macroscopic description at the population level, but perhaps more importantly is amenable to mathematical analysis (e.g. determination of linear stability thresholds) that gives good insight into the population collective behaviour. DDFT is itself based on equilibrium density functional theory (DFT), an approach that has long been used to describe the structure of matter, be it (crystalline) solid, liquid or gas [121–123]. We analyse in detail a version of the DDFT proposed in [119] (here we specify a particular model for the interaction potential between cells) and also extend the model to describe the dynamics of systems representing multiple cell types, incorporating the various different pair interactions between pairs of healthy cells, between pairs of cancer cells and the cancer-healthy pair interaction. The DDFT we use is based on a DFT able to describe both the fluid and (crystalline) solid phases of soft particles. In the latter, the density distribution corresponds to a regular array of peaks, defining where the particles are located. It is in this regime, where the peaks represent the loci of cell centres, that the theory is relevant to describing the microscopic density distribution of both cancer and healthy cells, which are treated as soft particles.

In the model of tumour growth discussed in this thesis, cells are viewed as colloid particles so that liquid state theory dynamic density functional theory is applicable as a basis for this model. In the next chapter, we will present this theory with application to cell birth/death processes.

CHAPTER 3

DENSITY FUNCTIONAL THEORY (DFT)

3.1 Introduction

Classical density functional theory (DFT) is a theory for the density distribution of the atoms, molecules, colloids, etc (henceforth referred to as "particles") under the influence of an external potential [121–123]. It is a theory built on statistical mechanics and thermodynamics. We use DFT as a basis for modelling cells with each of the particles being a cell. The particles interact via a pair potential. We begin this chapter by recalling some of the relevant background. We develop the thermodynamics of a system by considering a number of different ensembles. In statistical mechanics we are interested in average statistical properties of a system. This can be obtained by making a time-average on a single system, or by making

many copies of the system (an ensemble) and averaging over these. It was Gibbs in 1878 who introduced the concept of considering an ensemble. This is an idealisation in which one considers making a large number of copies (or replicas) of the system, each one of which represents a possible state the system could be in. There are a variety of different ensembles that tend to be used in thermodynamics, but the three that are of interest here are:

(1) The microcanonical ensemble: an ensemble of systems that each have the same fixed total energy U, volume V and number of particles in the system N.

(2) The canonical ensemble: an ensemble of systems, each of which can exchange energy with a large reservoir of heat; this fixes the temperature T of the system. Also, V and N are fixed.

(3) The grand canonical ensemble: an ensemble of systems, each of which can exchange both energy and number of particles with a large reservoir. This fixes the system's temperature T and the system's chemical potential μ (the energy needed to insert a particle into the system). V is also fixed.

3.2 Thermodynamics of homogeneous fluids

The first law of thermodynamics states that energy is conserved in macroscopic bodies, which leads to the identity [124]

$$dU = dQ + dW, \tag{3.2.1}$$

where dU is a change in the internal energy brought about by heat transfer to the system dQ and work done on the system dW [125]. We also have the following thermodynamic relations [124]

$$dW = -PdV, \tag{3.2.2}$$

$$dQ \leq TdS, \tag{3.2.3}$$

where P is the pressure, dV is the change in volume, T is the temperature and dS is the change in entropy. The equalities hold when the changes are reversible.

We initially consider a system in the microcanonical ensemble i.e. where U, V and N are all fixed. From the definition of this ensemble we see that $dU = 0$ and $dV = 0$. There is no work done $dW = 0$, due to the constant volume of the system. Substituting these values into the conservation of energy law Eq. (3.2.1) we find that $dQ = 0$ and therefore, from the identity Eq. (3.2.3) we obtain $dS \geq 0$.

This tells us that spontaneous change in the system might increase the entropy and so the equilibrium configuration of this system is the one which maximises the entropy S. This is a statement of the second law of thermodynamics; entropy, which in simple terms is often a measure of the disorder, increases monotonically as the system relaxes towards equilibrium.

An alternative set up is the canonical ensemble, where particles cannot cross the heat conducting boundary of the system. The volume V of the system and the number of particles N are fixed as before, but now we also fix the temperature T by coupling the system to a thermal bath and allow the internal energy U to fluctuate through the coupling to the bath. The constant volume means that there is no work done, i.e. $dW = 0$. Combining the two thermodynamic identities Eqs. (3.2.1)and (3.2.3) we obtain

$$dU - TdS \leq 0, \tag{3.2.4}$$

which can be re-written as

$$dF \leq 0, \tag{3.2.5}$$

where $F = U - TS$ is the Helmholtz free energy and dF is the change in the Helmholtz free energy. Any spontaneous changes will decrease F. This therefore tells us that the equilibrium configurations of the system in the canonical ensemble corresponds to minima in the Helmholtz free energy.

We can modify the canonical ensemble by retaining the fixed volume V and temperature T but now allowing particles to pass in and out of the system. Thus, the number of particles N in the system is no longer fixed, but is regulated by the chemical potential μ of the bath. The chemical potential defines the energy associated with adding or removing particles from the system and so it contributes to the conservation of energy identity Eq. (3.2.1) by adding the term μdN, where dN is the change in the number of particles. Following similar arguments to the previous case and including the μdN term to account for the change in energy when adding or removing a particle, we arrive at the following expression [124]

$$dU - TdS - \mu dN \leq 0, \tag{3.2.6}$$

which can be re-written as

$$d\Omega \leq 0, \tag{3.2.7}$$

where $\Omega = F - \mu N$ is the grand potential free energy of the system and $d\Omega$ is the change in the grand potential. So in a similar manner to the canonical ensemble, a system in the grand canonical ensemble reaches equilibrium when the grand potential Ω is at a minimum. We now introduce the number density of the system, which is the number of particles per unit volume $\rho = \frac{N}{V}$, which allows us to rewrite the

grand potential as $\Omega = fV - \mu\rho V$, where f is the Helmholtz free energy per unit volume. Equivalently we may calculate these volumes as integrals over the system, leading to the following notation:

$$\Omega = \int_V d\mathbf{r} f - \int_V d\mathbf{r} \mu\rho, \tag{3.2.8}$$

where $\mathbf{r}$ is a continuous vector representing the cartesian coordinates of points in the system. So far we have only considered homogeneous systems, which are found in the bulk, where there are no spatial variations in any external fields influencing the system.

3.3 Thermodynamics of inhomogeneous fluids

The density distribution becomes inhomogeneous when there is a spatially varying external field acting on it, such as that due to the wall of a container. The wall introduces inhomogeneity into the system causing for example in a liquid the particles to pack into layers near the wall. Thus, the local density is a quantity which is a function of the position $\mathbf{r}$ in the system, i.e. $\rho = \rho(\mathbf{r})$, the Helmholtz free energy per unit volume, the grand potential become functionals of the density, $f[\rho(\mathbf{r})]$ and $\Omega[\rho(\mathbf{r})]$, so Eq. (3.2.8) becomes [121–123]

$$\Omega[\rho(\mathbf{r})] = \int d\mathbf{r} f[\rho(\mathbf{r})] - \mu \int d\mathbf{r} \rho(\mathbf{r}). \tag{3.3.1}$$

As previously discussed, the equilibrium configuration corresponds to the minimum of the grand potential. Therefore we may state that density profiles $\rho^*(\mathbf{r})$ which minimise the functional $\Omega[\rho(\mathbf{r})]$ must be equilibrium density profiles; i.e. the equilibrium

density profile satisfies the Euler–Lagrange equation

$$\left.\frac{\delta\Omega[\rho(\mathbf{r})]}{\delta\rho(\mathbf{r})}\right|_{\rho(\mathbf{r})=\rho^*(\mathbf{r})} = 0. \tag{3.3.2}$$

Given a suitable approximation for the Helmholtz free energy term $\mathcal{F}[\rho(\mathbf{r})] = \int d\mathbf{r} f[\rho(\mathbf{r})]$ in Eq. (3.3.1) we now have a formalism to enable us to describe the structure of fluids or any other state of matter under the influence of a given external potential. Using the minimisation principle in Eq. (3.3.2), we can calculate the equilibrium density profile for a given external potential. For an ideal gas, i.e. a fluid composed of non-interacting particles, the Helmholtz free energy functional $F[\rho(\mathbf{r})]$ is known exactly [121]

$$\mathcal{F}[\rho(\mathbf{r})] = k_B T \int d\mathbf{r}\rho(\mathbf{r}) \left[\ln \Lambda^d \rho(\mathbf{r}) - 1\right] + \int d\mathbf{r} V_{ext}(\mathbf{r})\rho(\mathbf{r}), \tag{3.3.3}$$

where d is the dimensionality of the space in which the system exist, k_B is the Boltzmann constant, Λ is the thermal de Broglie wavelength (this quantity is irrelevant and one may assume Λ=1 [121,122]) and V_{ext} is the external potential. The ideal gas is worth briefly considering to give greater insight when below consider the influence of the interactions between particles. Using the minimisation principle in Eq. (3.3.2) for the ideal gas free energy in Eq. (3.3.3) we obtain:

$$k_B T \ln\left(\Lambda^d \rho^*(\mathbf{r})\right) + V_{ext}(\mathbf{r}) - \mu = 0, \tag{3.3.4}$$

which can be solved for $\rho^*(\mathbf{r})$ to give:

$$\rho^*(\mathbf{r}) = \Lambda^{-d} e^{\beta\mu} e^{-\beta V_{ext}(\mathbf{r})}, \tag{3.3.5}$$

where $\beta = \frac{1}{k_B T}$ is the inverse temperature. Thus, if we consider an ideal gas under the influence of an external potential that only varies in one direction, the density profile will only vary in that direction. An example of this is the external field above the surface of the Earth due to gravity (i.e. substitute $V_{ext} = mgz$ into Eq. (3.3.5), where z is the vertical distance from the earth's surface), then the resulting density profile abides by the barometric law

$$\rho(\mathbf{r}) = \rho(z) = \rho_o e^{\frac{-mgz}{k_B T}}, \tag{3.3.6}$$

where $\rho_o = \Lambda^{-d} e^{\beta\mu}$ is the density at $z = 0$.

Usually the interactions between the particles have a significant impact on the equilibrium density profiles and so one must add an additional term $\mathcal{F}_{ex}[\rho(\mathbf{r})]$ to the free energy which takes these interactions into consideration. Thus, the Helmholtz free energy in general is of the form [121–123]

$$\mathcal{F}[\rho(\mathbf{r})] = \mathcal{F}_{id}[\rho(\mathbf{r})] + \mathcal{F}_{ex}[\rho(\mathbf{r})] + \int d\mathbf{r} V_{ext}(\mathbf{r})\rho(\mathbf{r}), \tag{3.3.7}$$

where

$$\mathcal{F}_{id}[\rho(\mathbf{r})] = k_B T \int d\mathbf{r}\rho(\mathbf{r}) \left[\ln \Lambda^d \rho(\mathbf{r}) - 1\right] \tag{3.3.8}$$

is the ideal gas contribution to the free energy. Applying the minimisation principle (3.3.2) we find that the equilibrium density profile takes the form

$$\rho^*(\mathbf{r}) = \Lambda^{-d} e^{\beta\mu} e^{-\beta V_{ext}(\mathbf{r}) + c^{(1)}(\mathbf{r})}, \tag{3.3.9}$$

where the one body direct correlation function is defined as

$$c^{(1)}(\mathbf{r}) = -\beta \frac{\delta \mathcal{F}_{ex}[\rho(\mathbf{r})]}{\delta \rho(\mathbf{r})}. \tag{3.3.10}$$

The external potential V_{ext} is a potential which acts on each particle of the system individually. However, if we were to consider an effective external potential V_{ext}^{eff} which is the potential 'felt' by an individual particle, we need to consider a contribution from the neighbouring particles in the system. It is clear from Eq. (3.3.9) that the effective external potential felt by an individual particle is $V_{ext}^{eff}(\mathbf{r}) = V_{ext}(\mathbf{r}) - k_B T c^{(1)}(\mathbf{r})$ and so the one body direct correlation function can be thought of as a correction to the external potential V_{ext} that describes the effective potential due to all the other particles in the system.

Alternatively, one could consider the effective force acting on a particle located at position $\mathbf{r}$ in the system, due to the other particles in the system, which is simply given by the gradient of the one body direct correlation function $k_B T \nabla c^{(1)}(\mathbf{r})$ and so if we assume that the particles interact only via pair potentials $V_{int}(\mathbf{r}, \mathbf{r}')$, where $\mathbf{r}$ and $\mathbf{r}'$ are the locations of the two interacting particles, then the following sum rule applies [121],

$$-k_B T \nabla c^{(1)}(\mathbf{r}) = \int d\mathbf{r}' \rho^{(2)}(\mathbf{r}, \mathbf{r}') \nabla V_{int}(\mathbf{r}, \mathbf{r}'), \tag{3.3.11}$$

where $\rho^{(2)}(\mathbf{r}, \mathbf{r}')$ is the two-body density distribution which gives the probability of there being a particle at $\mathbf{r}'$, given there is another particle at $\mathbf{r}$. Similar sum rules may be derived when the particles do not just interact via pair potentials, but there are also higher body potentials [120].

The excess free energy term $\mathcal{F}_{ex}[\rho(\mathbf{r})]$ is usually unknown. There are many

different approximations which may be used, with some being more appropriate than others, depending on the nature of the interactions between the particles. In the low density limit the following is a good approximation for the excess free energy [123]

$$\mathcal{F}_{ex}[\rho(\mathbf{r})] = \frac{1}{2}\int d\mathbf{r}\int d\mathbf{r}' f_m(|\mathbf{r}-\mathbf{r}'|)\rho(\mathbf{r})\rho(\mathbf{r}') + O(\rho^3), \tag{3.3.12}$$

where $f_m(\mathbf{r}) = e^{-\beta V_{int}(\mathbf{r})} - 1$ is the Mayer function and $V_{int}(\mathbf{r})$ is the now assumed (spherically symmetric) pair potential used to model the interactions between the particles in the system. There are many other different approximations that can be used to take the particle interactions into account, for example a gradient expansion

$$\mathcal{F}_{ex}[\rho(\mathbf{r})] = \int d\mathbf{r}\int d\mathbf{r}'[f_o(\rho(\mathbf{r})) + f_2(\rho(\mathbf{r}))\left|\nabla\rho(\mathbf{r})\right|^2 + O(\nabla^4)], \tag{3.3.13}$$

or a Taylor series expansion

$$\begin{aligned}\mathcal{F}_{ex}[\rho(\mathbf{r})] &= \mathcal{F}_{ex}[\rho_o] + \int d\mathbf{r}\left.\frac{\delta\mathcal{F}_{ex}}{\delta\rho(\mathbf{r})}\right|_{\rho_o}\Delta\rho(\mathbf{r}) \\ &\quad + \frac{1}{2}\int d\mathbf{r}\int d\mathbf{r}'\left.\frac{\delta^2\mathcal{F}_{ex}}{\delta\rho(\mathbf{r})\delta\rho(\mathbf{r}')}\right|_{\rho_o}\Delta\rho(\mathbf{r})\Delta\rho(\mathbf{r}') + \cdots,\end{aligned} \tag{3.3.14}$$

where $\Delta\rho(\mathbf{r}) = \rho(\mathbf{r}) - \rho_o$ and where ρ_o is some reference uniform density.

For discussions on these and other approximations for the excess Helmholtz free energy, see Refs. [122,123]. For soft purely repulsive particles the following is a good approximation for the excess free energy [123]

$$\mathcal{F}_{ex}[\rho(\mathbf{r})] = \frac{1}{2}\int d\mathbf{r}\int d\mathbf{r}' V_{int}(|\mathbf{r}-\mathbf{r}'|)\rho(\mathbf{r})\rho(\mathbf{r}'). \tag{3.3.15}$$

Note that this is the functional which generates the following random-phase approx-

imation (RPA) for the pair direct correlation function

$$c_{eq}^{(2)}(|\mathbf{r}-\mathbf{r}'|;\rho_0) = -\beta \frac{\delta^2 \mathcal{F}_{ex}[\rho]}{\delta\rho(\mathbf{r})\delta\rho(\mathbf{r}')}\bigg|_{\rho(\mathbf{r})=\rho_0} = -\beta V_{int}(|\mathbf{r}-\mathbf{r}'|). \tag{3.3.16}$$

3.4 Microscopic statistical mechanical origin of DFT

Density functional theory may also be derived from the statistical mechanics of a system of interacting particles. Using statistical mechanics, thermodynamic quantities (such as those discussed previously in Sec.3.3; density ρ, chemical potential μ, etc) can be calculated by performing an ensemble average for the system. Since the system is in equilibrium, the resulting quantities are statistical average quantities, and so do not depend on the degrees of freedom of the individual particles nor the form of the equations of motion. Here we closely follow Evans' formalism [121] and neglect the details and proofs. For more details see the Refs. [121, 122].

We start by considering a system treated in the grand canonical ensemble, where the temperature T and the volume V are fixed and the system can exchange particles with a reservoir with a fixed chemical potential μ. The total energy of the N particles, each of mass m is given by the Hamiltonian [122, 123]

$$H_N = \sum_{i=1}^{N} \frac{{p_i}^2}{2m} + \Phi(\mathbf{r}_1, \cdots, \mathbf{r}_n) + \sum_{i=1}^{N} V_{ext}(\mathbf{r}_i), \tag{3.4.1}$$

where p_i is the momentum of particle i, $V_{ext}(\mathbf{r})$ is the one-body external potential and the total interatomic potential energy, $\Phi = \sum_{i,j} V_{int}(\mathbf{r}_i, \mathbf{r}_j) + \cdots$, where the "$\cdots$" denotes three-body interaction potential terms. The first term $K = \sum_{i=1}^{N} \frac{{p_i}^2}{2m}$ of the Hamiltonian represents the kinetic energy of the system.

The partition function (a sum over all the possible microscopic configurations) is an important statistical mechanical object, which allows us to obtain thermodynamics quantity from microscope information. The grand partition function, which corresponds to the sum over states in a grand canonical ensemble, is given by [121]

$$\Xi = Tr(e^{-\beta(H_N - \mu N)}), \tag{3.4.2}$$

where Tr is the trace operator which sums (integrates) over all possible microstates, incorporating the microscopic detail of the system

$$Tr(x) = \sum_{N=0}^{\infty} \frac{1}{h^{3N} N!} \int x d\mathbf{r}_1 \cdots d\mathbf{r}_N \int dp_1 \cdots dp_N, \tag{3.4.3}$$

where h is Planck's constant, $\mathbf{r}_i$ denotes the position of particle i and the factor $N!$ is present because particles are indistinguishable.

The grand potential is given by [121–123]

$$\Omega = -k_B T \ln \Xi. \tag{3.4.4}$$

The average one body density is the ensemble average of the density operator $\hat{\rho}(\mathbf{r}) = \sum_{i=1}^{N} \delta(\mathbf{r} - \mathbf{r}_i)$ and where $\delta(\mathbf{r} - \mathbf{r}_i)$ is the usual Dirac δ-function. Using the fact that $N = \int d\mathbf{r} \hat{\rho}(\mathbf{r})$, from Eqs. (3.4.4), (3.4.2) and (3.4.3) we see that the average density $\rho(\mathbf{r})$ can be obtained by a functional differentiation of Ω

$$\rho(\mathbf{r}) = -\frac{\delta \Omega}{\delta u(\mathbf{r})}, \tag{3.4.5}$$

where

$$u(\mathbf{r}) = \mu - V_{ext}(\mathbf{r}). \tag{3.4.6}$$

The density functional approach focuses on expressing thermodynamic quantities as a functional of $\rho(\mathbf{r})$, rather than $u(\mathbf{r})$, It is clear that $\rho(\mathbf{r})$ is a functional of $u(\mathbf{r})$, and so it follows that the probability density f_N, for observing the system at a certain point $(\{\mathbf{p}_i, \mathbf{r}_i\})$ in phase space

$$f_N = \Xi^{-1} e^{-\beta(H_N - \mu N)}, \tag{3.4.7}$$

where Ξ is the partition function given in Eq. (3.4.2), is uniquely determined by $\rho(\mathbf{r})$. The latter fixes $V_{ext}(\mathbf{r})$, which then determines f_N. Since f_N is a unique functional of $\rho(\mathbf{r})$, so is the quantity

$$F[\rho] = Tr\big[f_N(K + \Phi + \beta^{-1} \ln f_N)\big]. \tag{3.4.8}$$

Although this functional is usually unknown because the trace Tr can not be evaluated, this functional is defined exactly here using microscopic quantities. We may also consider the following functional, which is equal to the grand potential Ω when the density is at equilibrium $\rho = \rho^*$

$$\Omega[\rho] = F[\rho] + \int d\mathbf{r}\rho(\mathbf{r})V_{ext}(\mathbf{r}) - \mu \int d\mathbf{r}\rho(\mathbf{r}) \tag{3.4.9}$$

This is an alternative notation for the functional given in Eq. (3.3.1). As discussed in Sec. (3.3), the minimum of this functional corresponds to the equilibrium density profile and this lead to the minimisation principle Eq.(3.3.2). We can calculate the equilibrium density ρ^* for the given intrinsic Helmholtz free energy functional F and external potential $V_{ext}(\mathbf{r})$ by using the minimisation principle.

CHAPTER 4

DYNAMICAL DENSITY FUNCTIONAL THEORY (DDFT)

4.1 Introduction

Gradients in certain quantities can lead to fluxes. For example, a gradient in the temperature T leads to a flow of heat energy $\mathbf{j}_E = -\kappa\nabla T$, where $\mathbf{j}_E$ is a local heat flux density and κ is the material's thermal conductivity. On the other hand, a gradient in the chemical potential μ (the energy needed to insert a particle into the system) leads to a flux of particles

$$\mathbf{j} = -M\nabla\mu, \tag{4.1.1}$$

where the mobility M is a function of the local particle density ρ. Considering the dynamics of the density, if it is a conserved quantity, the time derivative of the density is equal to the divergence of the current, i.e. it is given by the continuity equation

$$\frac{\partial \rho}{\partial t} = -\nabla \cdot \mathbf{j}. \tag{4.1.2}$$

In the density functional theory [121, 123, 126] the equilibrium properties of the system are obtained by minimising the grand potential functional

$$\Omega[\rho(\mathbf{r})] = \mathcal{F}[\rho(\mathbf{r})] - \mu \int d\mathbf{r}\rho(\mathbf{r}), \tag{4.1.3}$$

where $\rho(\mathbf{r})$ is the one-body density profile, μ is the chemical potential and $\mathcal{F}$ is Helmholtz free energy functional given by Eq. (3.3.7).

Recall that the equilibrium density profile is given by the minimum of Ω, Eq. (4.1.3), which leads to

$$\mu = \frac{\delta \mathcal{F}[\rho]}{\delta \rho}. \tag{4.1.4}$$

For an equilibrium system, the chemical potential μ takes a constant value in space. DDFT assumes that (4.1.4) still holds out of equilibrium. Now, if we substitute Eqs.(4.1.1) and (4.1.4) into Eq.(4.1.2), yields

$$\frac{\partial \rho(\mathbf{r},t)}{\partial t} = \nabla \cdot \left[M \nabla \frac{\delta \mathcal{F}[\rho(\mathbf{r},t)]}{\delta \rho(\mathbf{r},t)} \right]. \tag{4.1.5}$$

Setting

$$M = \Gamma \rho(\mathbf{r},t), \tag{4.1.6}$$

we obtain

$$\frac{\partial \rho(\mathbf{r},t)}{\partial t} = \Gamma \nabla \cdot \left[\rho(\mathbf{r},t) \nabla \left(\frac{\delta \mathcal{F}[\rho(\mathbf{r},t)]}{\delta \rho(\mathbf{r},t)} \right) \right] \cdot \tag{4.1.7}$$

In the low density (ideal gas) limit, where the free energy is given by Eq.(3.3.3), we have $\frac{\delta \mathcal{F}[\rho]}{\delta \rho(\mathbf{r})} = k_B T \ln(\Lambda^d \rho(\mathbf{r})) + V_{ext}(\mathbf{r})$. Taking the gradient of this expression, we obtain

$$\nabla \frac{\delta \mathcal{F}[\rho]}{\delta \rho(\mathbf{r})} = \frac{k_B T}{\rho(\mathbf{r})} \nabla \rho(\mathbf{r}) + \nabla V_{ext}(\mathbf{r}). \tag{4.1.8}$$

Substituting Eq.(4.1.8) into Eq.(4.1.7) and imposing $V_{ext}(\mathbf{r}) = 0$, we obtain the diffusion equation

$$\frac{\partial \rho(\mathbf{r},t)}{\partial t} = D \nabla^2 \rho(\mathbf{r},t), \tag{4.1.9}$$

where the diffusion coefficient $D = \Gamma k_B T$. Thus we see that Eq.(4.1.6) is the correct form for the mobility function M. Recall that the diffusion equation describes the time evolution of the density distribution of Brownian particles. Thus, in applying this theory, we treat the particles as Brownian particles with stochastic differential equations of motion. In the following, we make this connection more formally.

4.2 DDFT of solid tumour growth

We now apply the methods of the previous section to derive a Fokker–Plank equation for a set of interacting particles, namely the cells in a tissues. Our presentation is based on the discussion in Refs. [13, 119]. Thus, we seek to derive equations describing the spatiotemporal evolution of the tissue on a cellular–scale description.

4.2.1 Langevin equation

We model the motion of each of the N interacting cells (assuming all are of the same species) by the over-damped Langevin equation, which is a stochastic differential equation describing Brownian motion of the cells

$$\frac{d\mathbf{r}_i}{dt} = \Gamma\left(\sum_{j=1}^{N}\mathbf{F}_{ij}^{int} + \mathbf{F}_i^{ext}\right) + \sqrt{2D}\boldsymbol{\eta}_i(t), \tag{4.2.1}$$

where $\mathbf{r}_i = (r_i^\alpha)_{\alpha=1\cdots d} \in \Psi^d$ is the position of the centre of mass of the i-th cell in the d-dimensional physical domain Ψ^d, Γ is the cell motility coefficient linked to the diffusion coefficient D by the Einstein relation $D = \Gamma k_B T$ (T is the temperature and k_B is Boltzmann's constant). The forces

$$\sum_{j=1}^{N}\mathbf{F}_{ij}^{int} = -\sum_{j=1}^{N}\nabla_{\mathbf{r}_i}V_{int}(|\mathbf{r}_i - \mathbf{r}_j|), \tag{4.2.2}$$

model cell-cell interactions by a pair potential V_{int} that depends on the distance between two cells. The force

$$\mathbf{F}_i^{ext} = -\nabla V_{ext}(\mathbf{r}_i, t), \tag{4.2.3}$$

where V_{ext} is the external potential e.g. due to any confining walls of other structures present. The vector $\boldsymbol{\eta}_i(t)$=$(\eta_i^x(t), \eta_i^y(t))$ is a Gaussian random noise whose components satisfy $\langle\eta_i^\alpha(t)\rangle$=0 and $\langle\eta_i^\alpha(t)\eta_j^\beta(t')\rangle = \delta_{ij}\delta_{\alpha\beta}\delta(t-t')$ where $\langle.\rangle$ denotes the statistical average over different noise realisation, δ_{ij} and $\delta_{\alpha\beta}$ are Kronecker deltas, $\delta(t-t')$ is a Dirac delta function and α, β are coordinate indices. This random term models the stochastic motions of the cells. We assume there is no cell-cell friction, which would involve the inclusion of an additional viscous drag force in Eq. (4.2.1).

4.2.2 Smoluchowski equation

Let $P(\mathbf{r}_1, \cdots, \mathbf{r}_N, t)$ denote the probability density function (PDF) of the position coordinates $\{\mathbf{r}_i\}, i = 1, \cdots, N$ for all N cells in the system. The time evolution of this PDF is given by the Smoluchowski equation [127, 128], which we now derive. Eq. (4.2.1) can be rewriten as

$$d\mathbf{r}_i = \Gamma \left(\sum_{j=1}^{N} \mathbf{F}_{ij}^{int} + \mathbf{F}_i^{ext} \right) dt + \sqrt{2D}\, d\boldsymbol{W}_i(t), \tag{4.2.4}$$

where $d\boldsymbol{W}_i(t)$ is an n variable Wiener process: $d\boldsymbol{W}_i(t) = \boldsymbol{W}_i(t + dt) - \boldsymbol{W}_i(t) = \boldsymbol{\eta}_i(t)dt$. Then by using the multivariable Ito formula of stochastic calculus [129], i.e. the analogue of going from Eq. (A.2.2) to Eq. (A.3.5) in Appendix A, we obtain

$$\frac{\partial P(\mathbf{r}^N, t)}{\partial t} = -\sum_{i=1}^{N} \nabla_i \cdot \Gamma \mathbf{F}_i(\mathbf{r}^N, t) P(\mathbf{r}^N, t) + \frac{1}{2} \sum_{i=1}^{N} \sum_{j=1}^{N} \nabla_i \cdot \nabla_j \left[\left(\sqrt{2D} \right)^2 \delta_{ij} P(\mathbf{r}^N, t) \right]. \tag{4.2.5}$$

Simplifying Eq. (4.2.5), we obtain the Smoluchowski equation

$$\frac{\partial P(\mathbf{r}^N, t)}{\partial t} = \sum_{i=1}^{N} \nabla_i \cdot \Big[-\Gamma \mathbf{F}_i(\mathbf{r}^N, t) + D \nabla_i \Big] P(\mathbf{r}^N, t), \tag{4.2.6}$$

where $\mathbf{r}^N = \{\mathbf{r}_i\}_{i=1,\cdots,N}$ is the Nd-dimensional vector containing the position vectors of all the cells and $\mathbf{F}_i = \sum_{j=1}^{N} \mathbf{F}_{ij}^{int} + \mathbf{F}_i^{ext}$ denotes the sum of forces exerted on a single cell. Using Eqs. (4.2.2) and (4.2.3), we can rewrite Eq. (4.2.6) in the form

$$\frac{\partial P(\mathbf{r}^N, t)}{\partial t} = \Gamma \sum_{i=1}^{N} \nabla_i \cdot \Big[k_B T\ \nabla_i + \nabla_i U(\mathbf{r}^N, t) \Big] P(\mathbf{r}^N, t), \tag{4.2.7}$$

where $U(\mathbf{r}^N, t)$ is the potential energy due to the inter-particle interactions and any external potentials. Thus, from Eq. (4.2.1) we derived Eq. (4.2.7) which is the time evolution equation of the N–particle position probability distribution $P(\mathbf{r}^N, t)$. There is another way to derive Eq. (4.2.7); see Appendix B.

4.2.3 From Smoluchowski to DDFT

In this section we derive an equation for the time evolution of the one body density profile, $\rho(\mathbf{r}, t)$, from the Smoluchowski equation, Eq. (4.2.7). The one body density is merely the integral of the probability distribution function

$$\rho(\mathbf{r}_1, t) = N \int d\mathbf{r}_2 \cdots \int d\mathbf{r}_N P(\mathbf{r}^N, t), \tag{4.2.8}$$

similarly, the two-body density is

$$\rho^{(2)}(\mathbf{r}_1, \mathbf{r}_2, t) = N(N-1) \int d\mathbf{r}_3 \cdots \int d\mathbf{r}_N P(\mathbf{r}^N, t), \tag{4.2.9}$$

and in general the n-particle density is

$$\rho^{(n)}(\mathbf{r}^n, t) = \frac{N!}{(N-n)!} \int d\mathbf{r}_{n+1} \cdots \int d\mathbf{r}_N P(\mathbf{r}^N, t). \tag{4.2.10}$$

Above, we have assumed that the potential energy function can be expressed in terms of a one-body external potential acting on each particle, $V_{ext}(\mathbf{r}_i, t)$, and that the particle interactions are sums of pair potentials, $V_{int}(\mathbf{r}_i, \mathbf{r}_j)$, [see Eq. (4.2.2)], however the argument is more general and can be extended to systems with three body potentials, $v_3(\mathbf{r}_i, \mathbf{r}_j, \mathbf{r}_k)$, and higher body interactions, where the potential

energy is

$$\begin{aligned} U(\mathbf{r}^N, t) &= \sum_{i=1}^{N} V_{ext}(\mathbf{r}_i, t) + \frac{1}{2!}\sum_{j\neq i}\sum_{i=1}^{N} V_{int}(\mathbf{r}_i, \mathbf{r}_j) \\ &\quad + \frac{1}{3!}\sum_{k\neq j}\sum_{j\neq i}\sum_{i=1}^{N} v_3(\mathbf{r}_i, \mathbf{r}_j, \mathbf{r}_k) + \cdots . \end{aligned} \tag{4.2.11}$$

For appropriate boundary conditions, we integrate Eq. (4.2.7) by parts and assume either periodic boundary conditions or that $\rho(\mathbf{r}, t)$ is zero on the boundaries [120]

$$\begin{aligned} \Gamma^{-1}\frac{\partial \rho(\mathbf{r}, t)}{\partial t} &= k_B T \nabla_1^2 \rho(\mathbf{r}_1, t) \\ &\quad + \nabla_1 \cdot \left[\rho(\mathbf{r}_1, t)\nabla_1 V_{ext}(\mathbf{r}_1, t)\right] \\ &\quad + \nabla_1 \cdot \int d\mathbf{r}_2 \rho^{(2)}(\mathbf{r}_1, \mathbf{r}_2, t)\nabla_1 V_{int}(\mathbf{r}_1, \mathbf{r}_2) \\ &\quad + \nabla_1 \cdot \int d\mathbf{r}_2 \int d\mathbf{r}_3 \rho^{(3)}(\mathbf{r}_1, \mathbf{r}_2, \mathbf{r}_3, t)\nabla_1 v_3(\mathbf{r}_1, \mathbf{r}_2, \mathbf{r}_3) \\ &\quad + \cdots . \end{aligned} \tag{4.2.12}$$

where $\rho^{(2)}(\mathbf{r}, \mathbf{r}', t)$ is the two–particle density distribution function. Since $\rho^{(2)}$ depends on $\rho^{(3)}$, the three–particle distribution function, and so on, Eq.(4.2.12) is not closed. To close Eq.(4.2.12), the system needs to be truncated and $\rho^{(2)}$ needs to be approximated.

The approach taken in deriving DDFT is to recall that in equilibrium, there is an exact sum rule which relates the gradient of the one body direct correlation function to the interparticle forces acting on a particle (recall that $-k_B T c^{(1)}(\mathbf{r})$ is the effective one-body potential due to interaction in the system). If the particles interact solely

via pair potentials

$$-k_BT\nabla c^{(1)}(\mathbf{r}_1) = \int d\mathbf{r}_2 \rho^{(2)}(\mathbf{r}_1, \mathbf{r}_2)\nabla_1 V_{int}(\mathbf{r}_1, \mathbf{r}_2). \tag{4.2.13}$$

This result can be generalised to systems where the particles interact via many-body potentials,

$$-k_BT\nabla c^{(1)}(\mathbf{r}_1) = \sum_{n=2}^{\infty} \int d\mathbf{r}_2 \cdots \int d\mathbf{r}_n \rho^{(n)}(\mathbf{r}^n, t)\nabla_1 v_n(\mathbf{r}^n). \tag{4.2.14}$$

From equilibrium statistical mechanics we also knows that $c^{(1)}(\mathbf{r})$ is equal to the functional derivative of the excess part of the Helmholtz free energy functional, Eq. (3.3.10). Making the approximation that these identities, Eqs. (4.2.14) and (3.3.10), valid for the equilibrium system, hold also for the non-equilibrium system and substituting into Eq. (4.2.12), we obtain the DDFT equation,

$$\frac{\partial \rho(\mathbf{r}, t)}{\partial t} = \Gamma\nabla \cdot \left[\rho(\mathbf{r}, t)\nabla\left(\frac{\delta \mathcal{F}[\rho(\mathbf{r}, t)]}{\delta \rho(\mathbf{r}, t)}\right)\right], \tag{4.2.15}$$

where $\mathcal{F}[\rho(\mathbf{r}, t)]$ is the equilibrium Helmholtz free energy functional in Eq. (3.3.7).

There are other alternative ways to derive Eq. (4.2.15), the first one is that given in Ref. [130], which uses a free energy minimisation principle. The second one, in Ref. [12], is obtained by defining a coarse geared density $\bar{\rho}$ which takes the form of a sum of noise averaged Dirac delta functions, without appealing to a free energy minimisation principle. For more details, see Refs. [12, 130]

To summarise in deriving Eq.(4.2.8) we have assumed that

$$\rho(\mathbf{r}, t)\nabla\frac{\delta \mathcal{F}^{ex}[\rho(\mathbf{r}), t]}{\delta \rho(\mathbf{r}, t)} = \int d\mathbf{r}' \rho^{(2)}(\mathbf{r}, \mathbf{r}', t)\nabla_{\mathbf{r}} V_{int}(|\mathbf{r} - \mathbf{r}'|). \tag{4.2.16}$$

In addition, we must in practice make a further approximation, since $\mathcal{F}[\rho]$ is in general unknown. The simple mean-field approximation [131] used here is

$$\begin{aligned}\mathcal{F}[\rho] &= k_B T \int d\mathbf{r}\rho\big(\mathbf{r}\big)(\ln \rho(\mathbf{r}) - 1\big) + \frac{1}{2}\int d\mathbf{r}\int d\mathbf{r}'\rho(\mathbf{r})\rho(\mathbf{r}')V_{int}(|\mathbf{r}-\mathbf{r}'|) \\ &\quad + \int d\mathbf{r}V_{ext}(\mathbf{r})\rho(\mathbf{r}). \end{aligned} \tag{4.2.17}$$

One may view this approximation as having stemmed from assuming that $\rho^{(2)}(\mathbf{r},\mathbf{r}',t) \approx \rho(\mathbf{r},t)\rho(\mathbf{r}',t)$. However, this view is somewhat simplistic, for the reasons discussed in [132]. Using Eq. (4.2.17), Eq.(4.2.15) becomes [12]

$$\begin{aligned}\frac{\partial\rho(\mathbf{r},t)}{\partial t} &= D\nabla^2\rho(\mathbf{r},t) + \Gamma\nabla\cdot[\rho(\mathbf{r},t)\nabla V_{ext}(\mathbf{r},t)] \\ &\quad +\Gamma\nabla\cdot\left[\rho(\mathbf{r},t)\int d\mathbf{r}'\rho(\mathbf{r}',t)\nabla_{\mathbf{r}}V_{int}(|\mathbf{r}-\mathbf{r}^{'}|)\right]. \end{aligned} \tag{4.2.18}$$

The mean-field approximation which is used in Eq. (4.2.17) can only be used when $V_{int}(\mathbf{r})$ is finite for all values of $\mathbf{r}$ and also fails when the particle density is low, where the particles largely interact two at a time and so the mean-field assumption that many particles interact simultaneously breaks down. It may also be the case that when the system is far from equilibrium the adiabatic approximation $\rho^{(2)}(\mathbf{r},\mathbf{r}',t) \approx \rho^{(2)}_{eq}(\mathbf{r},\mathbf{r}')$ fails, where $\rho^{(2)}_{eq}$ is a two-particle density distribution function evaluated for a system with equilibrium density $\rho_o(\mathbf{r}) = \rho(\mathbf{r},t)$. An alternative expression that could be used together with the expression in Eq. (3.3.14), is a Taylor expansion

truncated, at $\mathrm{O}(\Delta\rho^2)$. This series expansion gives

$$\begin{aligned}\mathcal{F}^{ex}[\rho(\mathbf{r},t)] &= \mathcal{F}^{ex}[\rho_0] + \mu_0^{ex}\int d\mathbf{r}\Delta\rho(\mathbf{r},t) \\ &\quad -\frac{k_BT}{2}\int d\mathbf{r}\Delta\rho(\mathbf{r},t)\int d\mathbf{r}'\Delta\rho(\mathbf{r}',t)c_{eq}^{(2)}(|\mathbf{r}-\mathbf{r}'|;\rho_0) \\ &\quad +\cdots, \end{aligned} \tag{4.2.19}$$

where $\Delta\rho(\mathbf{r},t) = \rho(\mathbf{r},t) - \rho_0$, $c_{eq}^{(2)}(|\mathbf{r}-\mathbf{r}'|;\rho_0) = -\beta\frac{\delta^2\mathcal{F}_{ex}[\rho]}{\delta\rho(\mathbf{r})\delta\rho(\mathbf{r}')}\Big|_{\rho(.)=\rho_0}$ is the direct two-point correlation function of the uniform system and μ_0^{ex} is the excess chemical potential. With this approximation Eq. (4.2.18) becomes

$$\begin{aligned}\frac{\partial\rho(\mathbf{r},t)}{\partial t} &= D\nabla^2\rho(\mathbf{r},t) + \Gamma\nabla\cdot[\rho(\mathbf{r},t)\nabla V_{ext}(\mathbf{r},t)] \\ &\quad -D\nabla\cdot\left[\rho(\mathbf{r},t)\int d\mathbf{r}'(\rho(\mathbf{r}',t)-\rho_0)\nabla_{\mathbf{r}}c_{eq}^{(2)}(|\mathbf{r}-\mathbf{r}'|;\rho_{\mathbf{0}})\right]. \end{aligned} \tag{4.2.20}$$

We note that in both of these models, the nonlocal terms may be further approximated using a gradient expansion [121].

4.3 Cell birth/death processes

We may extend the DDFT framework developed above to describe cells, which additionally have a non-conserved component to the dynamics due to birth/death (BD) processes. We consider combining BD and cell-movement processes. Then Eq. (4.2.15) becomes

$$\frac{\partial\rho(\mathbf{r},t)}{\partial t} = \Gamma\nabla\cdot\left[\rho(\mathbf{r},t)\nabla\left(\frac{\delta\mathcal{F}[\rho(\mathbf{r},t)]}{\delta\rho(\mathbf{r},t)}\right)\right] + D_{BD}[\rho(\mathbf{r},t)] \tag{4.3.1}$$

which describes both BD processes and cell movement simultaneously in a multicellular system, $D_{BD}[\rho(\mathbf{r},t)]$ represent the non-conserved dynamics duo to birth/death processes. We describe below in Sec. 4.4 how we use approximate this term.

4.4 Model Formulation

We present an example that contains the basic phenomenology of tumour growth to clarify the DDFT modeling framework. We assume that tumour cells move in response to cell-cell interaction forces, cell-extracellular matrix ECM (a complex network of proteins such as collagen secreted by support cells, which serves as a structural element in tissues [133]) interactions, which can be modelled as an external force $V_{ext} = -\xi_E E$, where E denote the density of the ECM. We assume that ECM is degraded and produced by tumour cells.

As a simple model for the cell-cell forces, we assume the cells interact via a soft, purely repulsive and radially symmetric pair potential

$$V_{int}(r) = \varepsilon \exp[-(r/R)^{\mathcal{N}}], \tag{4.4.1}$$

where r is the distance between the centres of the cells and the parameters ε and R define the strength and range of the potential, respectively. This is the so called generalised exponential model with exponent $\mathcal{N}$, or 'GEM-$\mathcal{N}$' potential [134–142]. Here, we set the exponent $\mathcal{N} = 4$ (see Fig.4.1). Such soft potentials arise as the coarse-grained effective potential between soft polymeric macromolecules in solution [134]. In this study, the parameter R typically represents the radius of a cell, so cells strongly repulse each other when the distance between their centres becomes

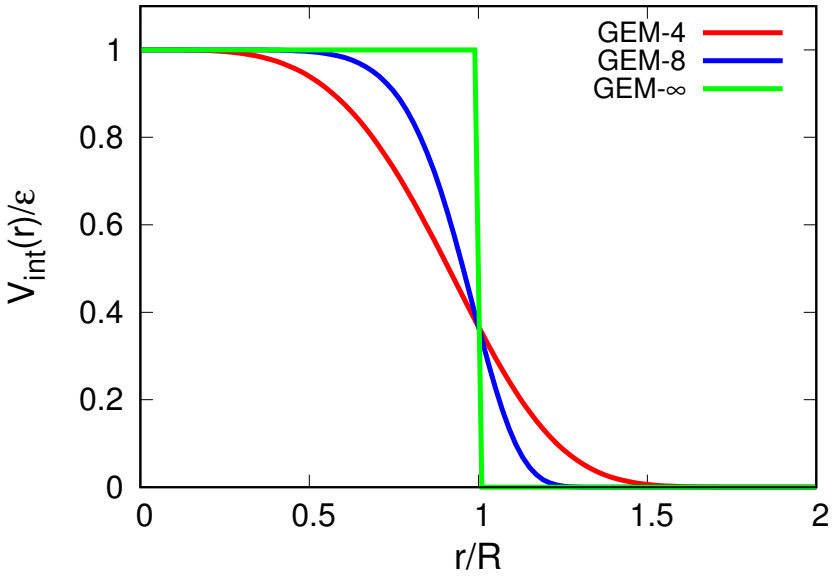

Figure 4.1: The GEM-$\mathcal{N}$ pair potential between the particles, for $\mathcal{N} = 4, 8, \infty$.

$\lesssim 2R$. Whilst this property of V_{int} is necessary for biological relevance, longer range effects (for distances $\gtrsim 2R$), such as cell-cell adhesion [113, 115, 118], can be straightforwardly built into the interaction function [121–123]. We consider this model because the bulk structure and phase behaviour of the GEM-$\mathcal{N}$ systems are well understood in both two-dimensions (2D) and three-dimensions (3D).

Accordingly, the over-damped Langevin equation (4.2.1) becomes

$$\frac{d\mathbf{r}_i}{dt} = \Gamma \sum_{j=1}^{N} \nabla V_{int}(|\mathbf{r}_i - \mathbf{r}_j|) + \chi_E \nabla E(\mathbf{r}_i) + \sqrt{2D}\boldsymbol{\eta}_i(t), \tag{4.4.2}$$

where χ_E is the diffusion coefficient of the external potential and defined as $\chi_E = \Gamma\xi_E$ and E is the density of the extracellular matrix (EMC). The ECM evolves according to

$$\frac{dE}{dt} = \lambda_E \sum_{i=1}^{N} \delta(\mathbf{r} - \mathbf{r}_i(t)), \tag{4.4.3}$$

where λ_E is the net rate of ECM production. In this model if we assume that $E = 0$, Eq. (4.4.2) reduces to Eq. (4.2.1).

The proliferation of tumour cells is dependent on the availability of nutrient (e.g. dissolved O_2) with concentration n. As a simple model of BD, we assume that a single cell can undergo mitosis with a nutrient-dependent rate $a_m = a_m(n)$. We model cell death (apoptosis) as occurring with a rate constant λ_d. This can be implemented as a Markov process and affects the number of cells in the population $N = N(t)$. The nutrient provided by the vascular system, diffuses through the microenvironment and is up-taken by tumour cells, and thus satisfies the reaction-diffusion equation

$$\frac{\partial n(\mathbf{r},t)}{\partial t} = D_n \nabla^2 n + S_n f(\mathbf{r}) - \tilde{\lambda}_n \sum_{i=1}^{N(t)} \delta(\mathbf{r} - \mathbf{r}_i(t)), \tag{4.4.4}$$

where D_n is the nutrient diffusion coefficient, S_n represent the amplitude of the nutrient source and $f(\mathbf{r})$ is a function that defines where in space the nutrient source is located and $f(\mathbf{r})$=1 corresponds to a uniform source. We consider a Gaussian

$$f(\mathbf{r}) = e^{-(x-L/2)^2}, \tag{4.4.5}$$

which corresponds to a source of nutrient along the line $x = \frac{L}{2}$ where L is the domain width, e.g. due to a capillary being there. $\tilde{\lambda}_n$ is the nutrient uptake rate assumed to be proportional to n, $\tilde{\lambda}_n = \lambda_n n$.

From the fact that the BD process is the result of two mass action laws gives $D_{BD}[\rho] = a_m(n)\rho - \lambda_d \rho$, where $a_m(n)$ is a nutrient-dependent growth rate and λ_d is the death rate. We assume that $a_m(n) = \lambda_m n$. We can derive the corresponding deterministic equation for the cell density. Taking correlations into account and

using the approximation (4.2.19), the cell density equation becomes

$$\begin{aligned}\frac{\partial \rho(\mathbf{r},t)}{\partial t} &= D\nabla^2\rho(\mathbf{r},t) + [\lambda_m(n(\mathbf{r},t)) - \lambda_d]\rho(\mathbf{r},t) \\ &\quad +\Gamma\nabla\cdot\left[\rho(\mathbf{r},t)\int d\mathbf{r}'\rho(\mathbf{r}',t)\nabla_{\mathbf{r}}V_{int}(|\mathbf{r}-\mathbf{r}'|)\right]. \qquad (4.4.6)\end{aligned}$$

Finally, when we average over all realisations of the noise in (4.2.1), since $\rho(\mathbf{r},t) = \langle\sum_{i=1}^{N(t)}\delta(\mathbf{r}-\mathbf{r}_i(t))\rangle$, we obtain the following equation for the nutrient concentration

$$\frac{\partial n(\mathbf{r},t)}{\partial t} = D_n\nabla^2 n(\mathbf{r},t) + S_n f(\mathbf{r}) - \lambda_n n(\mathbf{r},t)\rho(\mathbf{r},t). \qquad (4.4.7)$$

CHAPTER 5

MATHEMATICAL MODEL FOR A SINGLE SPECIES OF CELLS

5.1 Introduction

The model system of integro-partial differential equations derived in Sec.4.4, is

$$\frac{\partial \rho(\mathbf{r},t)}{\partial t} = D_c \nabla^2 \rho(\mathbf{r},t) + [\lambda_m n(\mathbf{r},t) - \lambda_d]\rho(\mathbf{r},t) + \Gamma \nabla \cdot \left[\rho(\mathbf{r},t) \int d\mathbf{r}' \rho(\mathbf{r}',t) \nabla_{\mathbf{r}} V_{int}(|\mathbf{r}-\mathbf{r}'|) \right], \tag{5.1.1}$$

$$\frac{\partial n(\mathbf{r},t)}{\partial t} = D_n \nabla^2 n(\mathbf{r},t) + S_n f(\mathbf{r}) - \lambda_n \rho(\mathbf{r},t) n(\mathbf{r},t). \tag{5.1.2}$$

The variables in the above system and their descriptions are summarised in Table 5.1. In this chapter we analyse this model using a linear stability analysis and by solving the model numerically. To solve the above model numerically, the convo-

lution integral is evaluated using Fourier transforms to turn the the above system to a system of partial differential equations. The second step is using the method of lines to discretise a partial differential equations to obtain system of ordinary differential equations. We use both Euler's Method and Adam's Method for the time stepping as a final step as explained in the Sec. 5.5. However, before this we nondimensionalise the model.

Table 5.1: Summary of the key quantities and model parameters in the one component model for cells plus nutrient, with governing equations Eqs.(5.1.1) and (5.1.2).

Quantity	Description
$\rho(\mathbf{r},t)$	Local number density of the cells
$n(\mathbf{r},t)$	Local concentration of nutrients
$V_{int}(\mathbf{r})$	Interaction potential between cells
$f(\mathbf{r})$	Nutrient source function
$N(t)$	The total number of cells in the population
$\bar{\rho}(t)$	Average cell number density
$\bar{n}(t)$	Average nutrient density
λ_m	Nutrient-dependent growth rate constant
λ_d	Cell death rate constant
λ_n	Nutrient uptake rate constant
D_c	Cell diffusion coefficient
D_n	Nutrient diffusion coefficient
Γ	Cell motility coefficient
k_BT	Thermal energy
ε	Cell-cell interaction energy
R	Cell radius
ρ_0	Constant reference density
$\mathcal{N}$	The exponent in the GEM-$\mathcal{N}$ pair interaction
S_n	The nutrient source amplitude
Λ	Thermal de Broglie wavelength
L^2	System domain area

5.2 Scaling and nondimensionalisation

5.2.1 Nondimensionalisation for the system of ODEs

Nondimensionalisation, or rescaling, refers to the process of transforming a series of equations (usually ODEs or PDEs) to dimensionless (i.e. unitless) forms by rescaling the model variables. To help choose the most appropriate rescaling, we first consider the case where the density and nutrients are spatially uniform, i.e. $\rho(\mathbf{r}, t) = \rho(t)$ and $n(\mathbf{r}, t) = n(t)$. From Eq. (5.1.1) and Eq. (5.1.2) we then obtain

$$\frac{d\rho}{dt} = [\lambda_m n - \lambda_d]\rho,$$

$$\frac{dn}{dt} = S_n - \lambda_n \rho n. \tag{5.2.1}$$

Note that Eq. (5.1.1) and Eq. (5.1.2) are now ODEs since there is now only one independent variable, t. This (dimensional) system of ODEs has 4 model parameters. λ_m is the nutrient-dependent growth rate, λ_d is the cell death rate constant, λ_n is the nutrient uptake rate constant and S_n is the nutrient source rate.

For the model variables shown in Table 5.1, we rescale the density of the cancer cells ρ, the local concentration of nutrients, n and time t as follows, denoting the respective dimensionless variables ρ^*, n^* and t^*, and corresponding rescaling variables are $\hat{\rho}$, $\hat{n}$ and $\hat{t}$, i.e.

$$\rho = \rho^* \hat{\rho}, \quad n = n^* \hat{n} \quad \text{and} \quad t = t^* \hat{t}. \tag{5.2.2}$$

First we substitute for ρ, n and t in our original equations.

$$\frac{\hat{\rho} d\rho^*}{\hat{t} dt^*} = [\lambda_m n^* \hat{n} - \lambda_d]\rho^* \hat{\rho}, \tag{5.2.3}$$

$$\frac{\hat{n}dn^*}{\hat{t}dt^*} = S_n - \lambda_n \rho^* \hat{\rho} n^* \hat{n}. \tag{5.2.4}$$

Next we rearrange so that we only have the derivatives of the rescaled variables on the left-hand side. In other words, we multiply each side of the first equation by $\frac{\hat{t}}{\hat{\rho}}$ and the second equation by $\frac{\hat{t}}{\hat{n}}$, and cancel similar terms on the right hand side, yielding

$$\frac{d\rho^*}{dt^*} = \hat{t}[\lambda_m n^* \hat{n} - \lambda_d]\rho^*, \tag{5.2.5}$$

$$\frac{dn^*}{dt^*} = \frac{\hat{t}}{\hat{n}}[S_n - \lambda_n \rho^* \hat{\rho} n^* \hat{n}]. \tag{5.2.6}$$

Our aim is to choose values of $\hat{\rho}$, $\hat{n}$ and $\hat{t}$ that simplify the model structure by reducing the total number of parameters. For the uniform system (5.2.1) the natural next step is to define our three parameters $\hat{\rho} = \frac{S_n \lambda_m}{\lambda_n \lambda_d}$, $\hat{n} = \frac{\lambda_d}{\lambda_m}$ and $\hat{t} = \frac{\lambda_d}{S_n \lambda_m}$. to get dimensionless equations

$$\frac{d\rho^*}{dt^*} = c[n^* - 1]\rho^*, \tag{5.2.7}$$

$$\frac{dn^*}{dt^*} = 1 - \rho^* n^*, \tag{5.2.8}$$

where $c = \frac{(\lambda_d)^2}{S_n \lambda_m}$. The above exercise nondimensionalising the homogeneous ODE model gives good insight to the behaviour of the model. We now proceed to consider the inhomogeneous case. We should also mention that in the inhomogeneous model, there are additional length and energy scales, so there are better choices for $\hat{\rho}$ and $\hat{t}$.

5.2.2 Nondimensionalisation of the full model

We now nondimensionlise the system of integro-partial differential equations given in Eqs. (5.1.1) and (5.1.2). These can be rewritten as

$$\frac{\partial \rho(\mathbf{r},t)}{\partial t} = \nabla \cdot \left[\Gamma \rho(\mathbf{r},t) \nabla \left(k_B T \ln \rho(\mathbf{r},t) + \int d\mathbf{r}' \rho(\mathbf{r}',t) V_{int}(|\mathbf{r}-\mathbf{r}'|) \right) \right] + [\lambda_m n(\mathbf{r},t) - \lambda_d] \rho(\mathbf{r},t) \tag{5.2.9}$$

$$\frac{\partial n(\mathbf{r},t)}{\partial t} = D_n \nabla^2 n(\mathbf{r},t) + S_n f(\mathbf{r}) - \lambda_n \rho(\mathbf{r},t) n(\mathbf{r},t). \tag{5.2.10}$$

We rescale each of the variables as $\rho = \rho^* \hat{\rho}$, $n = n^* \hat{n}$, $t = t^* \hat{t}$, $x = x^*/R$, $y = y^*/R$ and $V_{int}(r/R) = \varepsilon \tilde{V}_{int}(r^*)$, where the asterisked quantities are dimensionless variables and $\tilde{V}_{int}(r) = \exp(-r^{\mathcal{N}})$ is the dimensionless pair potential, we obtain from Eq. (5.2.9)

$$\frac{\partial(\rho^*(\mathbf{r},t)\hat{\rho})}{\partial(t\hat{t})} = \frac{1}{R}\nabla^* \cdot \left[\frac{\Gamma\hat{\rho}}{R} \rho^*(\mathbf{r},t) \nabla^* \left(k_B T \ln(\hat{\rho}\rho^*(\mathbf{r},t)) + R^2 \hat{\rho} \varepsilon \int d\mathbf{r}' \rho^*(\mathbf{r}',t) \tilde{V}_{int}(|\mathbf{r}-\mathbf{r}'|) \right) \right] + [\lambda_m n^*(\mathbf{r},t)\hat{n} - \lambda_d] \rho^*(\mathbf{r},t)\hat{\rho}. \tag{5.2.11}$$

We integrate over two dimensional space, so from the integral we get R^2 in the second term in the above equation. This can be simplified to

$$\frac{\partial \rho^*(\mathbf{r},t)}{\partial t} = \left(\frac{\hat{t}}{\hat{\rho}} \frac{\Gamma k_B T \hat{\rho}}{R^2} \right) \nabla^* \cdot \left[\rho^*(\mathbf{r},t) \nabla^* \left(\ln \rho^*(\mathbf{r},t) + R^2 \hat{\rho} \beta \varepsilon \int d\mathbf{r}' \rho^*(\mathbf{r}',t) \tilde{V}_{int}(|\mathbf{r}-\mathbf{r}'|) \right) \right] + \hat{t}\lambda_d \left[\left(\frac{\lambda_m \hat{n}}{\lambda_d} \right) n^*(\mathbf{r},t) - 1 \right] \rho^*(\mathbf{r},t), \tag{5.2.12}$$

where $\Gamma k_B T = D_c$, the cell diffusion coefficient and $\beta = 1/k_B T$. By choosing $\hat{t} = \frac{R^2}{D_c}$, $\hat{\rho} = \frac{1}{R^2}$ and $\hat{n} = \frac{\lambda_d}{\lambda_m}$, dropping the superscript * for clarity and noting that $\ln \hat{\rho}$ does

not feature because of ∇, we obtain

$$\begin{aligned}\frac{\partial\rho(\mathbf{r},t)}{\partial t} &= \nabla^2\rho(\mathbf{r},t) + \nabla\cdot\left(\rho(\mathbf{r},t)\nabla\int d\mathbf{r}'\rho(\mathbf{r}',t)\beta\varepsilon\tilde{V}_{int}(|\mathbf{r}-\mathbf{r}'|)\right)\\ &\quad +c_1\left[n(\mathbf{r},t)-1\right]\rho(\mathbf{r},t),\end{aligned} \tag{5.2.13}$$

where

$$c_1 = \frac{R^2\lambda_d}{D_c}. \tag{5.2.14}$$

Now consider Eq. (5.2.10). We obtain

$$\frac{\partial(n^*(\mathbf{r},t)\hat{n})}{\partial(t^*\hat{t})} = \frac{D_n}{R^2}\nabla^{*2}n^*(\mathbf{r},t)\hat{n} + S_n f(\mathbf{r}) - \lambda_n\rho^*(\mathbf{r},t)\hat{\rho}n^*(\mathbf{r},t)\hat{n}.$$

$$\frac{\partial n^*(\mathbf{r},t)}{\partial t^*} = \frac{D_n\hat{t}}{R^2}\nabla^{*2}n^*(\mathbf{r},t) + \frac{S_n\hat{t}}{\hat{n}}f(\mathbf{r}) - \lambda_n\rho^*(\mathbf{r},t)\hat{\rho}n^*(\mathbf{r},t)\hat{t}.$$

from the definition of $\hat{n}, \hat{t}$ and $\hat{\rho}$, we get

$$\frac{\partial n^*(\mathbf{r},t)}{\partial t^*} = \left(\frac{D_n}{D_c}\right)\nabla^{*2}n^*(\mathbf{r},t) + \left(\frac{R^2S_n\lambda_m}{\lambda_d D_c}\right)f(\mathbf{r}) - \left(\frac{\lambda_n R^2}{D_c R^2}\right)\rho^*(\mathbf{r},t)n^*(\mathbf{r},t).$$

Writing

$$\tilde{D} = \frac{D_n}{D_c},\ \tilde{S}_n = \frac{R^2S_n\lambda_m}{\lambda_d D_c} \text{ and } \tilde{\lambda}_n = \frac{\lambda_n}{D_c}, \tag{5.2.15}$$

and omitting the superscript *, we get

$$\frac{\partial n(\mathbf{r},t)}{\partial t} = \tilde{D}\nabla^2 n(\mathbf{r},t) + \tilde{S}_n f(\mathbf{r}) - \tilde{\lambda}_n\rho(\mathbf{r},t)n(\mathbf{r},t). \tag{5.2.16}$$

The above equation together with Eq.(5.2.13) constitutes the non-dimensionalised model equations that we study.

5.3 Parameter values

We now consider what are suitable parameter values for our model. For the homogeneous system (5.2.1), we know that

$$\rho(t) = \rho_0 e^{(\lambda_m n^* - \lambda_d)t}. \tag{5.3.1}$$

If we assume a typical value that after 12 h the population density ρ is assumed to double in time [143], i.e. $\rho(t{=}12 \text{ h}) = 2\rho(t = 0)$, then Eq. (5.3.1) implies

$$\ln \frac{2\rho(0)}{\rho(0)} = (\lambda_m n^* - \lambda_d)12 \text{ h},$$

from which we can deduce the following estimate for $\lambda_m n^* - \lambda_d$,

$$\ln 2 = 12(\lambda_m n^* - \lambda_d) \text{ h} \Rightarrow (\lambda_m n^* - \lambda_d) = \frac{\ln 2}{12} \text{ h}^{-1}. \tag{5.3.2}$$

According to [144], a typical value for the concentration of oxygen in fresh water $[O_2] = n^* = 6.383$ mg/L, so we estimate that the critical level n_d for $[O_2]$ is approximately $\frac{n^*}{20} = \frac{6.383}{20} \approx 0.32$ mg/L (equivalent to about 1% of atmospheric levels). Hence, $\lambda_m n_d - \lambda_d = 0$ leads to

$$\lambda_m = \frac{\lambda_d}{0.32 \text{ mg/L}}. \tag{5.3.3}$$

Substituting Eq.(5.3.3) into Eq.(5.3.2) gives

$$\left(\frac{\lambda_d}{0.32} 6.383 - \lambda_d\right) = \frac{\ln 2}{12} \text{ h}^{-1} \Rightarrow \left(\frac{6.383}{0.32} - 1\right) \lambda_d = \frac{\ln 2}{12} \text{ h}^{-1},$$

hence,

$$\lambda_d = \frac{\ln 2}{12 \times 18.95} = 0.003 \text{ h}^{-1} = 0.00005 \text{ min}^{-1},$$

and from Eq.(5.3.3) we find that

$$\lambda_m = \frac{\lambda_d}{0.32} = \frac{0.00005}{0.32} = 0.00015 \text{ min}^{-1}. \tag{5.3.4}$$

The length scale R is the mean radius of the cells, so from Table 5.2 we have $R \approx 10\mu$m=0.001 cm and in 2 dimensions the typical diffusion distance in time t, is estimated from the average distance diffused squared over time, $\langle r^2 \rangle = 4D_c t$. Assuming the time taken to travel a distance of order the diameter of the cell R is 12 hours, then

$$(2R)^2 = 4D_c \times 12 \text{ h} \Rightarrow R^2 = 12D_c$$

hence,

$$D_c = \frac{R^2}{12hrs.} = \frac{0.001^2}{12 \times 60min} = 1.3 \times 10^{-9} \text{ cm}^2/\text{min}.$$

The population growth constant is $c_1 = \frac{R^2 \lambda_d}{D_c}$, so we get $c_1 = 0.038$. From the definition of $\tilde{D}_c = \frac{D_n}{D_c}$, and $D_n = 2 \times 10^{-5}$ cm^2/sec ($D_n = 12 \times 10^{-4}$ cm^2/min) [24], this leads to

$$\tilde{D} = \frac{12 \times 10^{-4}}{13 \times 10^{-10}} \approx 1 \times 10^6. \tag{5.3.5}$$

The nutrient source term $\tilde{S}_n = \frac{R^2 S_n \lambda_m}{\lambda_d D_c}$ is estimated to be O(10^6) so that in Eq. (5.2.16) $\bar{n}$ is in balance with the diffusion term. Hence $\frac{3}{13} \times 10^4 S_n \approx (10^6)$ $\Rightarrow S_n = 433$. From Eq. (5.2.16) we also see that the term involving $\tilde{\lambda}_n$ also must balance with diffusion, hence from Eq. (5.2.15) we see λ_n must be O(10^{-4}) to ensure that $\tilde{\lambda}_n$ is of O(10^6).

Thus, typical choices for the initial conditions might be

$$\rho^*(\mathbf{r},0) = \frac{\rho(\mathbf{r},0)}{\hat{\rho}(\mathbf{r},0)} = \frac{10^6}{1/R^2} = 1, \tag{5.3.6}$$

$$n^*(\mathbf{r},0) = \frac{n(\mathbf{r},0)}{\hat{n}(\mathbf{r},0)} = \frac{1}{\lambda_d/\lambda_m} = \frac{\lambda_m}{\lambda_d} = \frac{15\times10^{-5}}{5\times10^{-5}} = 3. \tag{5.3.7}$$

Recall that the number density of the system, is the number of cells per unit area $\rho = \frac{N}{A}$. Since $R \approx 10\mu$m =0.001 cm, this implies that the area covered by one cell = $\pi R^2 \approx 3\times10^{-6}$ cm^2. This then implies that a typical cell density is $\rho \approx \frac{1}{3}\times10^6$ cm^{-2} i.e. 3×10^5 cm^{-2}.

We summarise the values of the various dimensional parameters in Table 5.2 and the dimensionless parameter values in Table 5.3.

5.3.1 Standard parameter set

The ratio of diffusion coefficients in Eq. (5.3.5) is large which means that quantities take dimensionless values covering several order of magnitudes O(10^{-2}) – O(10^6). This is because the nutrient evolves on much faster time scales than the cells, which creates challenges for the numerical methods. Since the algorithm must run over a long time, the (nutrient) terms associated with the O(10^6) parameters values equilibrate very rapidly O(10^{-6}), compared to the slower (cells evolution) processes O(10^2). Consequently, tempering the large valued parameters, say (10^6) $\to$ 1, has little effect on the long term results, but greatly helps in the running of the numerical code. See below in Sec. 5.5.4.1, where we vary $\tilde{D}$ over the range $[1, 10^3]$ and see very little effect on the results. We therefore select the parameter set given in Table 5.3 and henceforth use these as our standard parameter set, where $\gamma(\mathbf{r})$ is a random

Table 5.2: Model parameters and their units. Values marked with asterisk (*) are estimates from Sec. 5.3.

Symbol	Description	typical value	Unit	Source
$\rho(\mathbf{r},t)$	The number density of the cells	$3\times10^5*$	cm^{-2}	estimated
$n(\mathbf{r},t)$	The local concentration of nutrients	3 *	mg/L	estimated
$V_{int}(\lvert\mathbf{r}-\mathbf{r}'\rvert)$	Interaction potential between cells	ε/k_BT	dimensionless	§3.3
$N(t)$	The total number of cells in the population	ρ_0L^2	dimensionless	§5.5.3.1
R	The radius of the cells	0.001	cm	[145]
λ_m	The nutrient-dependent growth rate	0.00015 *	min^{-1}	estimated
λ_d	The cell death rate constant	0.00005 *	min^{-1}	estimated
λ_n	The nutrient uptake rate	3 *	min^{-1}	estimated
D_c	The diffusion coefficient of cells	$1.3\times10^{-9}*$	cm^2min^{-1}	estimated
D_n	The diffusion coefficient of nutrient	0.0012	cm^2min^{-1}	[24]
Γ	The cell motility coefficient	3×10^{10} *	$ming^{-1}$	estimated
T	The temperature	310	K	[145]
k_B	Boltzmann's constant	1.38×10^{-23}	$Joule/K$	[146]
ε	Energy scale in interaction potential between cells	k_BT	$Joule$	§3.3
ρ_0	A constant reference density	3×10^5 *	cm^{-2}	§5.5.3.1
L^2	The area of the system	6×10^{-4}	cm^2	§5.5.3.1
S_n	The nutrient source	433 *	$mgL^{-1}min^{-1}cm^{-2}$	estimated

Table 5.3: Dimensionless parameter values of the model.

Nondimensional parameter	Dimension form	Value	Used value
c_1	$R^2\lambda_d/D_c$	0.038	1
$\tilde{D}$	D_n/D_c	10^6	$1, 10, 10^2, 10^3$
$\tilde{S}_n$	$R^2 S_n \lambda_m/\lambda_d D_c$	10^6	10, 35, 65
$\tilde{\lambda}_n$	λ_n/D_c	10^6	1
ρ^*	$\rho/\hat{\rho}$	1	$1+\gamma(\mathbf{r})$
n^*	$n/\hat{n}$	3	1
$\varepsilon\tilde{V}_{int}(r^*)$	$V_{int}(r/R)$	See Eq. (4.4.1)	ε/k_BT

variable with $\gamma(\mathbf{r}) \sim U(0,1)$, where U is a uniform distribution

5.4 Linear stability analysis

The aim of a linear stability analysis is to determine where in the phase diagram (parameter space) the uniform density state becomes unstable. We seek to locate the region of the phase diagram in which the modulated (periodic) state occurs, since this is the state modelling the distribution of cells.

For $\tilde{S}_n > 0$ and $f(\mathbf{r})$=1 there is a unique uniform density steady state that is a stationary solution of Eqs. (5.2.13) and (5.2.16), that is

$$n = n_o = 1, \quad \rho = \rho_o = \tilde{S}_n/\tilde{\lambda}_n. \tag{5.4.1}$$

We now investigate the linear stability of the uniform density state (ρ_o, n_o) to non-uniform perturbations $(\delta\rho(\mathbf{r},t), \delta n(\mathbf{r},t))$, with $\|\delta\rho\|_\infty = \xi$ and $\|\delta n\|_\infty = \chi\xi$, where $\xi \ll 1$. The analysis also applies more generally to determine the growth or decay of a perturbation about a uniform density state (ρ_o, n_o), with values different to those in Eq. (5.4.1), i.e. the timescale for cell repositioning in response to the perturbation

is much faster than cell growth; we note $c_1 \ll 1$ from data, see Table 5.3. Note that it is the parameter values where the uniform system is unstable (and forms peaks) that are of biological relevance.

To determine the linear stability of the flat (uniform density) state in this model, we assume that the order parameter profile of both components takes the form

$$\begin{aligned} \rho &= \rho_o + \delta\rho(\mathbf{r}, t) \\ &= \rho_o + \xi e^{i(\mathbf{k}.\mathbf{r})+\omega t}, \end{aligned} \tag{5.4.2}$$

and

$$\begin{aligned} n &= n_o + \delta n(\mathbf{r}, t) \\ &= n_o + \chi\xi e^{i(\mathbf{k}.\mathbf{r})+\omega t}, \end{aligned} \tag{5.4.3}$$

where $0 < \xi \ll 1$ is the initial amplitude of the sinusoidal perturbation that has wavenumber $k = |\mathbf{k}|$, χ is the ratio between the amplitude of the modulation in the two components, and the growth or decay rate of the perturbations is given by the dispersion relation $\omega = \omega(k)$. Substituting Eqs. (5.4.2) and (5.4.3) into the dynamic equation (5.2.13), we get

$$\begin{aligned} \omega\delta\rho(\mathbf{r}, t) \;=\; & -k^2\delta\rho(\mathbf{r}, t) \\ & +\nabla \cdot \left[(\rho_o + \delta\rho(\mathbf{r}, t)) \nabla \left(\int d\mathbf{r}'(\rho_o + \delta\rho(\mathbf{r}', t))\beta\varepsilon\tilde{V}_{int}(|\mathbf{r} - \mathbf{r}'|) \right) \right] \\ & +c_1 \left([n_o + \chi\delta\rho(\mathbf{r}, t) - 1][\rho_o + \delta\rho(\mathbf{r}, t)] \right). \end{aligned} \tag{5.4.4}$$

Splitting the term in $\rho_o + \delta\rho(\mathbf{r},t)$ inside the integral in two separate terms, we get

$$\begin{aligned}\omega\delta\rho(\mathbf{r},t) &= -k^2\delta\rho(\mathbf{r},t) \\ &\quad +\nabla\cdot\Bigg[\big(\rho_o+\delta\rho(\mathbf{r},t)\big)\nabla\Bigg(\rho_o\int d\mathbf{r}'\beta\varepsilon\tilde{V}_{int}(|\mathbf{r}-\mathbf{r}'|) \\ &\quad +\xi e^{\omega t}\int d\mathbf{r}' e^{i(\mathbf{k}.\mathbf{r}')}\beta\varepsilon\tilde{V}_{int}(|\mathbf{r}-\mathbf{r}'|)\Bigg)\Bigg] \\ &\quad +c_1\left([n_o-1]\rho_o+(\rho_o\chi+n_o-1)\delta\rho(\mathbf{r},t)+O(\delta\rho^2)\right).\end{aligned} \tag{5.4.5}$$

writing $-\mathbf{r}+\mathbf{r}'=\mathbf{r}''$, and using the fact that $d\mathbf{r}'=d\mathbf{r}''$ and $e^{i(\mathbf{k}.\mathbf{r}')}=e^{i\mathbf{k}.(\mathbf{r}''+\mathbf{r})}$, we get

$$\begin{aligned}\omega\delta\rho(\mathbf{r},t) &= -k^2\delta\rho(\mathbf{r},t) \\ &\quad +\nabla\cdot\Big[\rho_o\nabla\Big(\rho_o\beta\varepsilon\hat{V}(0)+\xi e^{i(\mathbf{k}.\mathbf{r})+\omega t}\beta\varepsilon\hat{V}(k)\Big)\Big] \\ &\quad +c_1\left([n_o-1]\rho_o+(\rho_o\chi+n_o-1)\delta\rho(\mathbf{r},t)\right)+O(\delta\rho^2),\end{aligned} \tag{5.4.6}$$

where $\hat{V}(k)$ is 2D Fourier transform of the pair potential [147, 148]

$$\hat{V}(k)=\int d\mathbf{r}e^{i(\mathbf{k}.\mathbf{r})}\tilde{V}_{int}(\mathbf{r})=2\pi\int_0^\infty r\tilde{V}_{int}(\mathbf{r})J_0(kr)dr, \tag{5.4.7}$$

and $J_0(x)$ is the Bessel function of order 0. Using the fact that $\nabla\delta\rho(\mathbf{r},t)=ik\delta\rho(\mathbf{r},t)$ and that $\nabla^2\delta\rho(\mathbf{r},t)=-k^2\delta\rho(\mathbf{r},t)$, we obtain

$$\begin{aligned}\omega\delta\rho(\mathbf{r},t) &= -k^2\big[1+\rho_o\beta\varepsilon\hat{V}(k)\big]\delta\rho(\mathbf{r},t) \\ &\quad +c_1(n_o-1)\rho_o+c_1(\rho_o\chi+n_o-1)\delta\rho(\mathbf{r},t)+O(\delta\rho^2),\end{aligned} \tag{5.4.8}$$

recalling that $\delta\rho(\mathbf{r},t)=\xi e^{i(\mathbf{k}.\mathbf{r})+\omega t}$.

At the fixed points, the second term on the right hand side is zero. Dividing both

sides by $\delta\rho(\mathbf{r},t)$ then assuming $\delta\rho(\mathbf{r},t)$ is small, we arrive to the dispersion relation

$$\omega(k) \;=\; -k^2\left[1+\rho_o\beta\varepsilon\hat{V}(k)\right]+c_1\left(n_o+\rho_o\chi-1\right). \tag{5.4.9}$$

The limit of linear stability is defined as the locus of points in parameter space where the maximum in the dispersion relation (5.4.9) is at zero, i.e. $\omega(k=k_c)=0$, where k_c is the wave vector where $\omega(k)$ is maximum, where $\frac{d\omega}{dk}|_{k=k_c}=0$. In the case of $c_1 \ll 1$ we have

$$1+\rho_o\beta\varepsilon\hat{V}(k=k_c)\approx 0, \tag{5.4.10}$$

where $k_c = 5.1$ and $\hat{V}(k_c) = -0.16$ (recall that in the non dimensionalisation we effectively set the unit of length $R=1$), which implies that the locus of where the system becomes linearly unstable is

$$\rho_o \approx \frac{1}{\beta\varepsilon|\hat{V}(k_c)|} \tag{5.4.11}$$

which in the density ρ_o versus "dimensionless temperature" $k_BT/\varepsilon = 1/\beta\varepsilon$ plane is a straight line passing through the origin, as shown in Fig 5.1 (c.f Fig. 2 in Ref. [149] for comparison.) For densities greater than this value, the system is linearly unstable. Note that even though we have assumed $c_1 \ll 1$ in the derivation, it turns out that even when $c_1 \sim O(1)$, Eq. (5.4.11) gives a good estimate for where the system is linearly unstable. Given the data in Table 5.3, the analysis suggests that the dominant terms governing the instability are the cell density and the cell-cell interaction parameters; cell growth and nutrient consumption rates are secondary to this process.

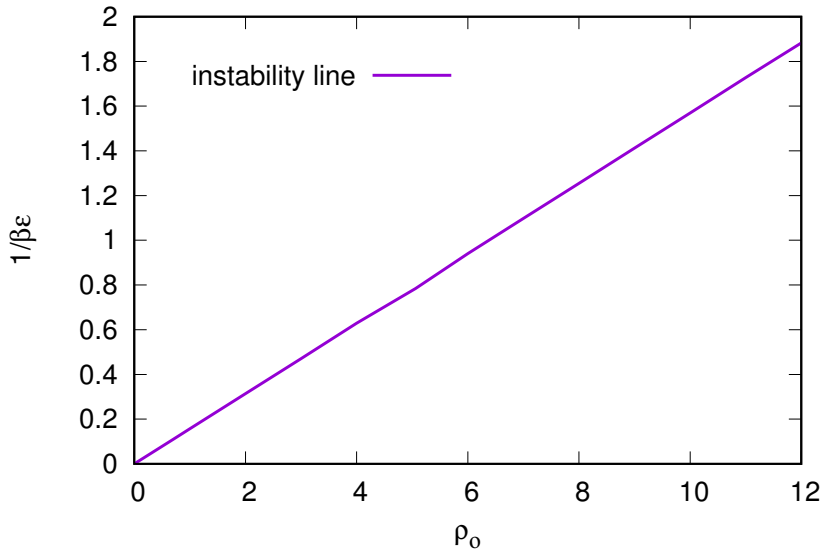

Figure 5.1: The linear stability threshold (5.4.11) for the one cell species model [see Eq. (5.2.13)] for $c_1 = 0$. To the right of this line the uniform density is linearly unstable, forming the modulated state used to model the cell distribution.

5.5 Numerical results for the cell evolution

The coupled equations (5.2.13) and (5.2.16) are solved numerically using the method of lines. The density profiles are discretised on a spatially uniform grid, with the convolution integral evaluated in Fourier space using fast Fourier transforms, whilst the time stepping is implemented through either an Euler method or an Adams–Bashforth method, via the freeware ODEPACK routine DLSODE [150, 151]. Here we compare two approaches for solving the model numerically. We note that the Adams–Bashforth time stepping method is significantly faster than the Euler time stepping routines used for the similar problem as explained in the next sections and also in [149]. The Euler method is described below in Sec. 5.5.3 and the Adams method is described in Sec. 5.5.4.

5.5.1 Evaluating the convolution integral

For each time step, the first step of our numerical algorithm is to evaluate the convolution integral term in Eq.(5.2.13), $\mathcal{C}(\mathbf{r}) = \int d\mathbf{r}'\rho(\mathbf{r}')\beta\varepsilon\tilde{V}_{int}(|\mathbf{r}-\mathbf{r}'|)$, by using Fourier transforms and the convolution theorem as follows:

- Computing the Fourier transform of each function $\rho(\mathbf{r}')$ and $\tilde{V}_{int}(|\mathbf{r}-\mathbf{r}'|)$,

$$\hat{\rho}(\mathbf{k}) = \int d\mathbf{r} e^{i(\mathbf{k},\mathbf{r})}\rho(\mathbf{r}), \tag{5.5.1}$$

$$\hat{V}(k) = \int d\mathbf{r} e^{i(\mathbf{k},\mathbf{r})}\tilde{V}_{int}(\mathbf{r}) = 2\pi\int_0^\infty r\tilde{V}_{int}(\mathbf{r})J_0(kr)dr,$$

  where $\hat{\rho}(\mathbf{k})$ and $\hat{V}(k)$ are 2D Fourier transforms of the density profile at that specific time and pair potential respectively.

- Computing the Fourier transform of the convolution integral is the product

$$\mathscr{F}\left(\int d\mathbf{r}'\rho(\mathbf{r}')\beta\varepsilon\tilde{V}_{int}(|\mathbf{r}-\mathbf{r}'|)\right) = \beta\varepsilon\hat{\rho}(\mathbf{k})\hat{V}(k), \tag{5.5.2}$$

- Computing the inverse Fourier transform of the product, gives the convolution integral

$$\mathscr{F}^{-1}\left(\beta\varepsilon\hat{\rho}(\mathbf{k})\hat{V}(k)\right) = \mathcal{C}(\mathbf{r}). \tag{5.5.3}$$

The integro-partial differential equation (5.2.13) then appears as a partial differential equation after the convolution integral has been evaluated,

$$\begin{aligned}\frac{\partial\rho(\mathbf{r},t)}{\partial t} &= \nabla^2\rho(\mathbf{r},t) + \nabla\cdot\left(\rho(\mathbf{r},t)\nabla\mathcal{C}(\mathbf{r},t)\right)\\ &\quad + c_1\left[n(\mathbf{r},t)-1\right]\rho(\mathbf{r},t).\end{aligned} \tag{5.5.4}$$

Eq. (5.5.4) together with Eq. (5.2.16) then forms a system of partial differential equations which we can deal with using the method of lines, as explained in the next section.

5.5.2 Method of lines

The method of lines (MOL) is a general way of discretising a partial differential equation (PDE) to obtain system of ordinary differential equations (ODEs). The basic idea of MOL is to replace the spatial derivatives in the partial differential equation with algebraic approximations. Once this is done, the spatial derivatives are no longer stated explicitly in terms of the spatial independent variables. Thus, in effect, only one remaining independent variable t remains and we have a system of ODEs that approximates the original PDE. We write Eq. (5.5.4) in the form

$$\begin{aligned}\frac{\partial \rho(\mathbf{r},t)}{\partial t} &= \nabla^2\rho(\mathbf{r},t) + \Big(\rho(\mathbf{r},t)\big(\mathcal{C}(\mathbf{r},t)\big)_x\Big)_x + \Big(\rho(\mathbf{r},t)\big(\mathcal{C}(\mathbf{r},t)\big)_y\Big)_y \\ &\quad + c_1\left[n(\mathbf{r},t)-1\right]\rho(\mathbf{r},t). \end{aligned} \tag{5.5.5}$$

We subdivide the xy-plane into a set of equal rectangles of sides Δx and Δy and let the coordinates (x, y) of the representative mesh points be $x = i\Delta x$ and $y = j\Delta y$ where i and j are positive integers. We denote the value of ρ and n at point(i, j) by $\rho_{i,j}$ and $n_{i,j}$ respectively, where $0 \leq i\ \Delta x \leq L$ and $0 \leq j\ \Delta y \leq L$. By using the finite difference equation and setting $\Delta x = \Delta y$, we can rewrite Eq (5.5.5) as

$$\begin{aligned}\frac{d\rho_{i,j}}{dt} &= \frac{\rho_{i-1,j}+\rho_{i+1,j}+\rho_{i,j-1}+\rho_{i,j+1}-4\rho_{i,j}}{\Delta x^2} \\ &+\frac{\rho_{i,j}\,\mathcal{C}_{i+1,j}-3\rho_{i,j}\,\mathcal{C}_{i,j}+\rho_{i+1,j}\,\mathcal{C}_{i,j}+2\rho_{i,j}\,\mathcal{C}_{i-1,j}-\rho_{i+1,j}\,\mathcal{C}_{i-1,j}}{\Delta x^2} \\ &+\frac{\rho_{i,j}\,\mathcal{C}_{i,j+1}-3\rho_{i,j}\,\mathcal{C}_{i,j}+\rho_{i,j+1}\,\mathcal{C}_{i,j}+2\rho_{i,j}\,\mathcal{C}_{i,j-1}-\rho_{i,j+1}\,\mathcal{C}_{i,j-1}}{\Delta x^2} \\ &+c_1\,[n_{i,j}-1]\,\rho_{i,j}. \end{aligned} \tag{5.5.6}$$

Let us denote the right hand side of Eqs.(5.5.6) by $f(\rho_{i,j}, n_{i,j})$, to obtain,

$$\frac{d\rho_{i,j}}{dt} = f(\rho_{i,j}, n_{i,j}). \tag{5.5.7}$$

By a similar technique, we can transform Eq. (5.2.16) into

$$\frac{dn_{i,j}}{dt} = g(\rho_{i,j}, n_{i,j}), \tag{5.5.8}$$

where $g(\rho_{i,j}, n_{i,j})$ is the spatial discretisation of the right hand side of Eqs.(5.2.16). In the next section we describe how to solve the system of ODEs (5.5.7) and (5.5.8) using the Euler method and in the section after how to do so using the Adams method.

5.5.3 Euler method

The explicit Euler method is perhaps the simplest algorithm to use to solve the model (5.5.7) and (5.5.8), which consists of a pair of coupled PDEs. If we assume that $t = m\Delta t$, where Δt is a small time increment and m is an integer, then $\rho(\mathbf{r}, t) = \rho^m(\mathbf{r})$, $n(\mathbf{r}, t) = n^m(\mathbf{r})$, we can iterate the following equations to obtain the

time-evolution of the profiles [152]

$$\rho^{m+1}(\mathbf{r}) = \rho^m(\mathbf{r}) + \Delta t \left[\frac{\partial \rho^m(\mathbf{r})}{\partial t}\right], \tag{5.5.9}$$

$$n^{m+1}(\mathbf{r}) = n^m(\mathbf{r}) + \Delta t \left[\frac{\partial n^m(\mathbf{r})}{\partial t}\right]. \tag{5.5.10}$$

These expressions come from forward finite difference approximations for the expression in the square brackets. The terms in the square brackets are then replaced by the right hand sides of Eqs.(5.5.7) and (5.5.8), respectively. To evaluate the spatial derivatives and convolution integrals we use spatial finite differences and fast Fourier transforms as explained in Sections 5.5.1 and 5.5.2, to obtain

$$\rho_{i,j}^{m+1} = \rho_{i,j}^m + \Delta t \left[f(\rho_{i,j}^m, n_{i,j}^m)\right], \tag{5.5.11}$$

$$n_{i,j}^{m+1} = n_{i,j}^m + \Delta t \left[g(\rho_{i,j}^m, n_{i,j}^m)\right]. \tag{5.5.12}$$

For the diffusion equation (i.e. the ideal gas limit), using central differences and a forward Euler time step, stability requires $\Delta t \leq (\Delta x^2 + \Delta y^2)/4$ [152]. From this we expect the method to be stable for small enough Δt. In the simulations that follow, we set $\Delta t = 0.002$. We found this to be a large enough suitable value that provides acurate results in all the test simulations.

5.5.3.1 Results using the Euler Method

We apply the Euler method which is explained in Sec. 5.5.3, with initial conditions

$$\rho(\mathbf{r}, 0) = 1 + \gamma(\mathbf{r}) \quad \text{and} \quad n(\mathbf{r}, 0) = 1, \tag{5.5.13}$$

where $\gamma(\mathbf{r})$ is a random variable with $\gamma(\mathbf{r}) \sim U(0,1)$, where U is a uniform distribution, as shown in the profile at t=0 in Fig. 5.2. We assume that the energy scale in the interaction potential between cells $\beta\varepsilon = 1$, that the population growth constant $c_1 = 1$, the nutrient source parameter $\tilde{S}_n = 35$ with the Gaussian function $f(\mathbf{r})$ given in Eq.(4.4.5), that corresponds to there being a nutrient source along the line $x = \frac{L}{2}$. The diffusion coefficient $\tilde{D} = 1$ and the nutrient uptake rate $\tilde{\lambda}_n = 1$. We set the grid spacing $\Delta x = 0.1$ the system size to be $(25.6)^2$ and time step $\Delta t = 0.002$. We use periodic boundary conditions on all sides. This system size is big enough to avoid significant effects due to the boundaries whilst being small enough to not make computations take too long.

In Fig. 5.2, the plots in the first column is the density profile of the cells at a series of different times (t=0, 0.5, 0.7 and 5), while the second column consists of plots of the local concentration of the nutrient and the last one displays plots of the logarithm of the density profile, $\ln \rho(\mathbf{r})$, which allows to see the details in the density profile away from the density peaks. From the last column, it is clear that we start with a small amplitude random cell distribution at t=0. By t=5.0 the cells further away from the nutrient source have died off, while the density profile near the nutrient source takes the form of a stripe pattern. This pattern is only temporary as the stripes break up into peaks (i.e. cells) arranged in a nearly hexagonal pattern. The cell ordering also impacts the nutrient concentration distribution.

We see that around the nutrient source, along the line $x = \frac{L}{2}$, there is a region where the peaks grow and then split –modelling cell division– and then move away from the nutrient source, where they subsequently die. In Fig. 5.3 we display a magnification of the cell density profile to highlight the mitotic events. The sequence of snapshots in Fig. 5.3 illustrates the cell splitting events that occurs between the

times t =2.05 and t =2.10 with time increments of 0.01. We observe that a peak first elongates and then splits to form new peaks which remarkably mirrors a mitotic event. In the fourth snapshot ($t = 2.08$) in Fig. 5.3, a peak spontaneously emerges between two existing ones, describing the average location of a new cell resulting from mitosis of one of the cells either side of it.

We plot in Fig. 5.4 the average cell density and nutrient density (over the whole system) as function of time. These are calculated as

$$\bar{\rho}(t) = \frac{1}{L^2} \int \int \rho(x, y, t) dx dy, \tag{5.5.14}$$

$$\bar{n}(t) = \frac{1}{L^2} \int \int n(x, y, t) dx dy. \tag{5.5.15}$$

Fig. 5.4 shows that the cell density reaches a maximum and the nutrient reaches a minimum when $t \approx 1$. As time further increases, both the cell and the nutrient densities vary over time, with an average cell density of approximately 5, while the nutrient density is approximately 0.5. Note that the small amplitude oscillations in $\bar{\rho}(t)$ for $t > 3$ are associated with the cell division, which is an approximately periodic process.

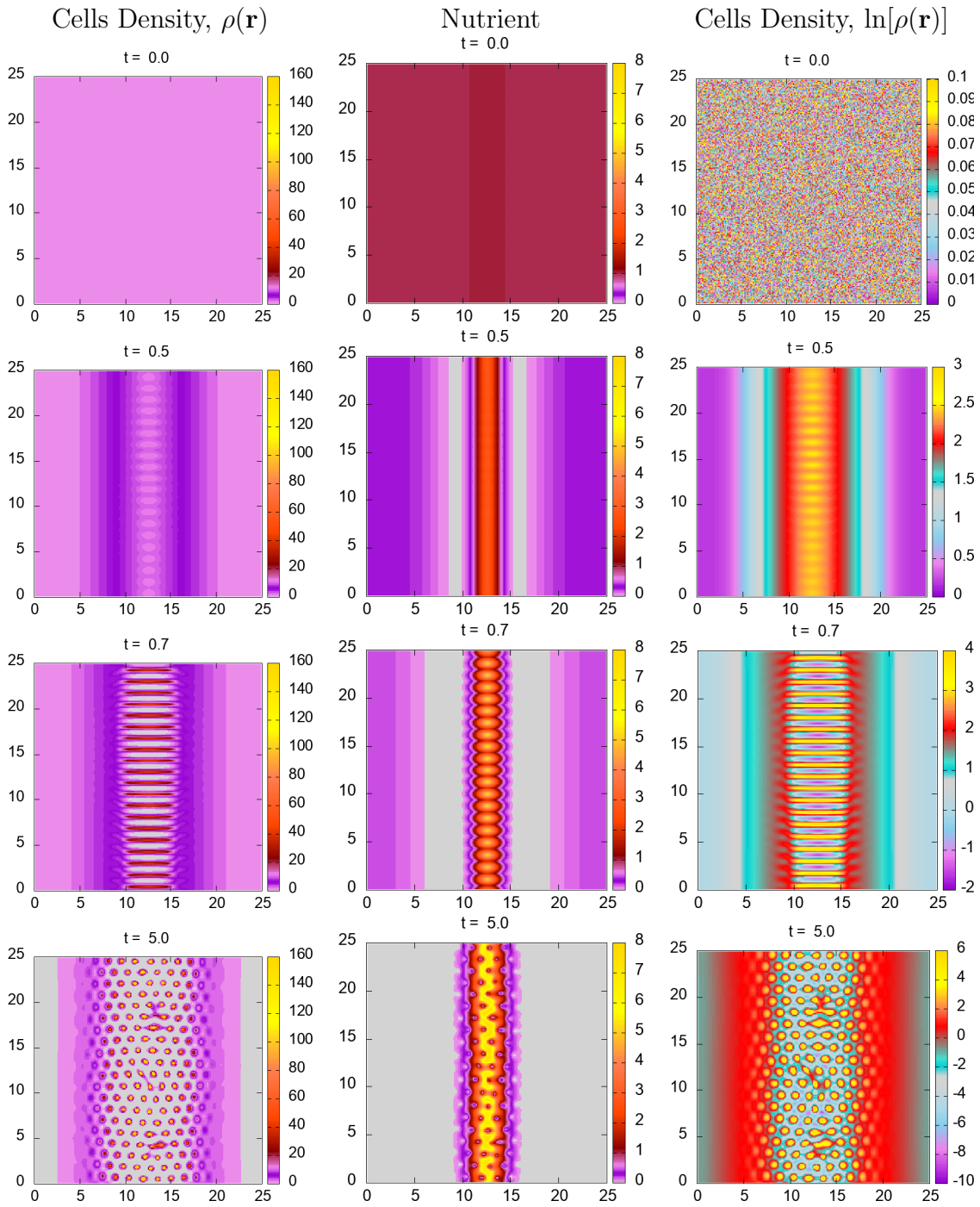

Figure 5.2: Density of cells and local nutrition concentration. We assume that the population growth constant c_1=1 and an energy scale in interaction potential between cells $\beta\varepsilon$=1. The diffusion coefficient $\tilde{D}$=1, nutrient source $\tilde{S}_n$=35 with $f(\mathbf{r})$ given in Eq.(4.4.5) and nutrient uptake rate $\tilde{\lambda}_n$=1. The area of the model is 25.6^2 and Δx=0.1. These results were obtained using Euler Method.

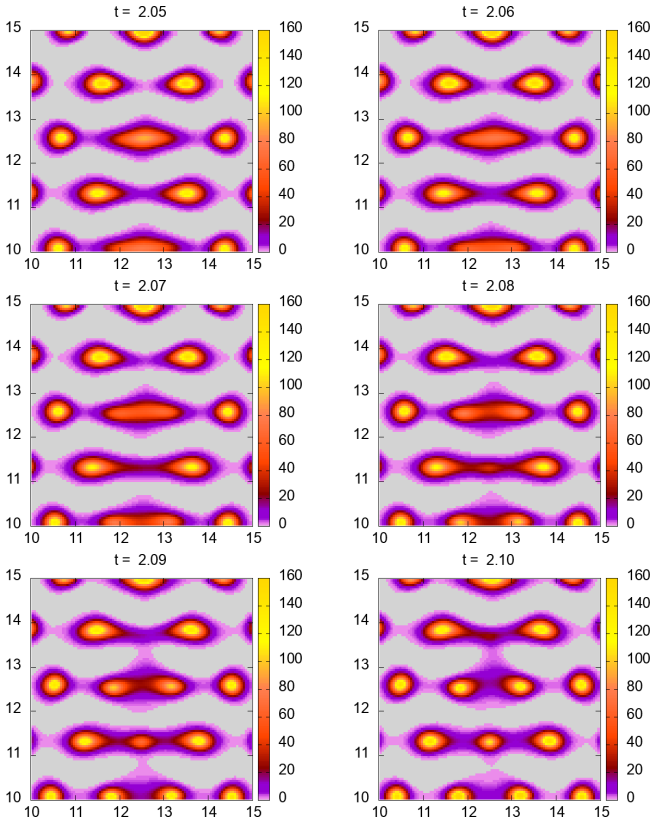

Figure 5.3: Snapshots of several peak splitting events that occur between the times $t = 2.05$ and $t = 2.10$. The figures above are in time increments of 0.01 going from top left to bottom right, corresponding to the profiles plotted in Fig. 5.2.

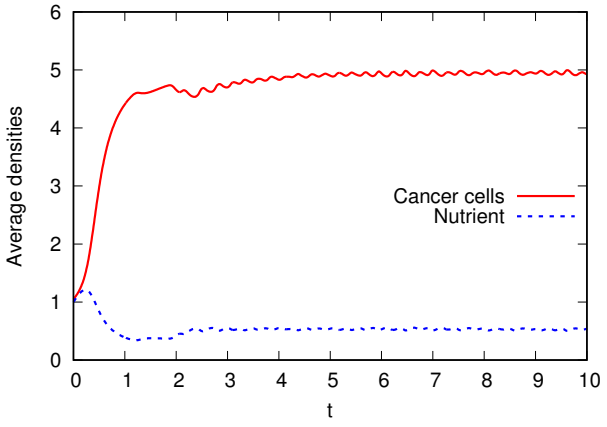

Figure 5.4: The average cell density, [see Eq.(5.5.14)] and the average nutrient density [see Eq.(5.5.15)], corresponding to the results in Fig. 5.2.

5.5.4 The Adams Methods

In this section we introduce the alternative Adams numerical method because the Euler method is very slow in time to get the results. For example, the results in Fig. 5.2 required the code to run for approximately one day. The Adams Methods is faster than the Euler's method, taking roughly half an hour to obtain the corresponding results using a desktop iMac with 3.2 GHz processor and 8 GB memory.

To derive the Adams–Bashforth method, we write Eqs. (5.5.9) and (5.5.10) as follows [152]

$$\rho^{m+1}(\mathbf{r}) = \rho^{m}(\mathbf{r}) + \int \frac{d\rho(\mathbf{r})}{dt} dt = \rho^{m}(\mathbf{r}) + \int f\big(\rho(\mathbf{r}), n(\mathbf{r}), t\big) dt, \tag{5.5.16}$$

$$n^{m+1}(\mathbf{r}) = n^{m}(\mathbf{r}) + \int \frac{dn(\mathbf{r})}{dt} dt = n^{m}(\mathbf{r}) + \int g\big(\rho(\mathbf{r}), n(\mathbf{r}), t\big) dt, \tag{5.5.17}$$

where the terms $f(\rho(\mathbf{r}), n(\mathbf{r}), t_m)$ and $g(\rho(\mathbf{r}), n(\mathbf{r}), t_m)$ are then replaced by the right hand sides of Eqs. (5.2.13) and (5.2.16) respectively. Adams methods are based on the idea of approximating the integrand by a polynomial within the interval (t_m, t_{m+1}). Using a kth order polynomial results in a $(k+1)$-th order method. There are two types of Adams methods, the explicit and the implicit types. The explicit type is called the Adams–Bashforth (AB) method and the implicit type is called the Adams–Moulton (AM) method. The first order AB and AM methods are simply the forward and the backward Euler methods respectively. The second order versions (obtained by using a linear interpolation) of these methods are quite popular. The second order Adams–Bashforth (AB2) method is given by [152]

$$\rho_{i,j}^{m+1} = \rho_{i,j}^{m} + \frac{\Delta t}{2}\Big[3f(\rho_{i,j}^{m}, n_{i,j}^{m}) - f(\rho_{i,j}^{m-1}, n_{i,j}^{m-1})\Big], \tag{5.5.18}$$

$$n_{i,j}^{m+1} = n_{i,j}^{m} + \frac{\Delta t}{2}\left[3g(\rho_{i,j}^{m}, n_{i,j}^{m}) - g(\rho_{i,j}^{m-1}, n_{i,j}^{m-1})\right]. \tag{5.5.19}$$

Note that the AB2 method is explicit and hence only conditional numerically stable. Moreover, the AB2 method requires the solution from the $(m-1)$-th and the m-th steps to find the solution at the $(m+1)$th step. The second order Adams–Moulton (AM2) is an implicit technique, sometimes referred to as the trapezoidal rule. The time-stepping equation for AM2 is given by [152]

$$\rho_{i,j}^{m+1} = \rho_{i,j}^{m} + \frac{\Delta t}{2}\left[f(\rho_{i,j}^{m+1}, n_{i,j}^{m+1}) + f(\rho_{i,j}^{m}, n_{i,j}^{m})\right], \tag{5.5.20}$$

$$n_{i,j}^{m+1} = n_{i,j}^{m} + \frac{\Delta t}{2}\left[g(\rho_{i,j}^{m+1}, n_{i,j}^{m+1}) + g(\rho_{i,j}^{m}, n_{i,j}^{m})\right], \tag{5.5.21}$$

We have to solve a non-linear algebraic equation at every time step. This is much more expensive compared to the explicit AB2 method. However, being an implicit technique, AM2 has more favourable stability properties than the AB2 for relatively large values of the time step. Once again, it is a trade-off between stability and computational cost, since both AM2 and AB2 are second order accurate. We note that the time step used by the ODEPACK routine is selected internally and adaptively.

5.5.4.1 Results with an inhomogeneous nutrient source

In this section we solve the system of integro-partial differential equations (5.2.13) and (5.2.16) using Adams method. We assume that the population growth constant $c_1 = 1$, the energy scale in interaction potential between cells $\beta\varepsilon = 1$, the nutrient uptake rate $\tilde{\lambda}_n = 1$ and the diffusion coefficient $\tilde{D} = 1$. We set the area of the domain in which the model is solved to be 25.6×25.6 and the nutrient source $\tilde{S}_n = 35$ with Gaussian $f(\mathbf{r})$ given in Eq. (4.4.5) along the line $x = \frac{L}{2}$. We use periodic boundary

conditions for both the sides and corners.

We plot in Fig. 5.6 the total cell density and nutrient density (over the whole system) as function of time, [see Eqs. (5.5.14) and (5.5.15)]. As time increases, the nutrient density varies, settling on a value of about 0.5, whereas the cell density oscillates around a constant cell density of 5. Note that the oscillations are less clearly visible than in Fig. 5.4 due to the longer time period over which results are displayed. Fig. 5.6 shows the total cell numbers and nutrient for different values of the grid spacing, showing that the solutions are robust to the change of grid.

Figs. 5.5, 5.7 and 5.9 show the results for the cell density profile time evolution for three different values of $\tilde{D} = 1$, 10 and 100. For example, the results in the left hand column of Fig. 5.5 shows the evolution of cell density, displaying snapshots for the times t=1.2, 2, 2.1 and 5 for the case $\tilde{D} = 1$. In these cases the nutrient source is located along the vertical mid line of the system [c.f. Eq. (4.4.5)]. From an initial randomised distribution, the cell density grows in the vicinity of central nutrient source. When the density is sufficiently large, an instability (c.f. Sec. 5.4) leads first to a striped pattern and then peaks. The density peaks (i.e. cells) are arranged in a roughly hexagonal pattern, which also impacts the nutrient distribution. the second column consists of plots of the local concentration of the nutrient and the last one displays plots of the logarithm of the density profile, $\ln \rho(\mathbf{r})$, which allows to see the details in the density profile away from the density peaks.

In Fig. 5.8 we display plots of the total cell density and nutrient density calculated using Eqs. (5.5.14) and (5.5.15), corresponding to Figs. 5.5, 5.7 and 5.9. These results are for three very different values of $\tilde{D} = 1$, 10 and 100. Nonetheless, we see that in all three cases the results are all qualitatively rather similar, which demonstrates that for $\tilde{D} \gtrsim 1$ the results do not qualitatively depend on the precise

value of $\tilde{D}$. Recall that in Sec. 5.3 we note that the true value is $\tilde{D} \approx 10^6$ [see Eq. (5.3.5)], but also argue that we do not need to have such a large value. Owing to the qualitative similarity of the results shown in Figs. 5.5, 5.7 and 5.9, we see that smaller values of $\tilde{D} \approx 10$ are acceptable.

The similarities for different values of the diffusion coefficient ratio $\tilde{D}$ can also be seen from the results in Fig. 5.8, whereby the steady value of $\bar{\rho} \approx 5$ and $\bar{n} \approx 0.5$ is reached by $t \approx 4$. Note that for the smaller $\tilde{D} = 1$ case there are small amplitude oscillations in both the cell and nutrient average densities for $t > 2$. These are due to new cells being formed and then dying in a periodic fashion.

5.5.4.2 Results with a homogeneous nutrient source

In this section we solve the system of integro-partial differential equations (5.2.13) and (5.2.16) with a uniform nutrient source with $f(\mathbf{r})$=1 and $\tilde{S}_n = 10$. All other parameters are the same as Fig. 5.5, i.e. we assume that the population growth constant c_1=1, the energy scale in the interaction potential between cells $\beta\varepsilon = 1$, the nutrient uptake rate $\tilde{\lambda}_n = 1$ and the diffusion coefficient $\tilde{D} = 1$. We set the grid spacing $\Delta x = 0.1$ and the system size to be $(25.6)^2$, with periodic boundary conditions on all sides. The time stepping is implemented via the Adams method.

In Fig. 5.10, the plots in the first column is the density profile of the cells at a series of different times (t=2.6, 2.7, 2.8 and 5.0), while the second column displays plots of the local nutrient concentration and the last column displays the logarithm of the density profile, $\ln(\rho(\mathbf{r}))$, which allows to see the details in the density profile away from the density peaks. From column 1, it is clear that the total density of

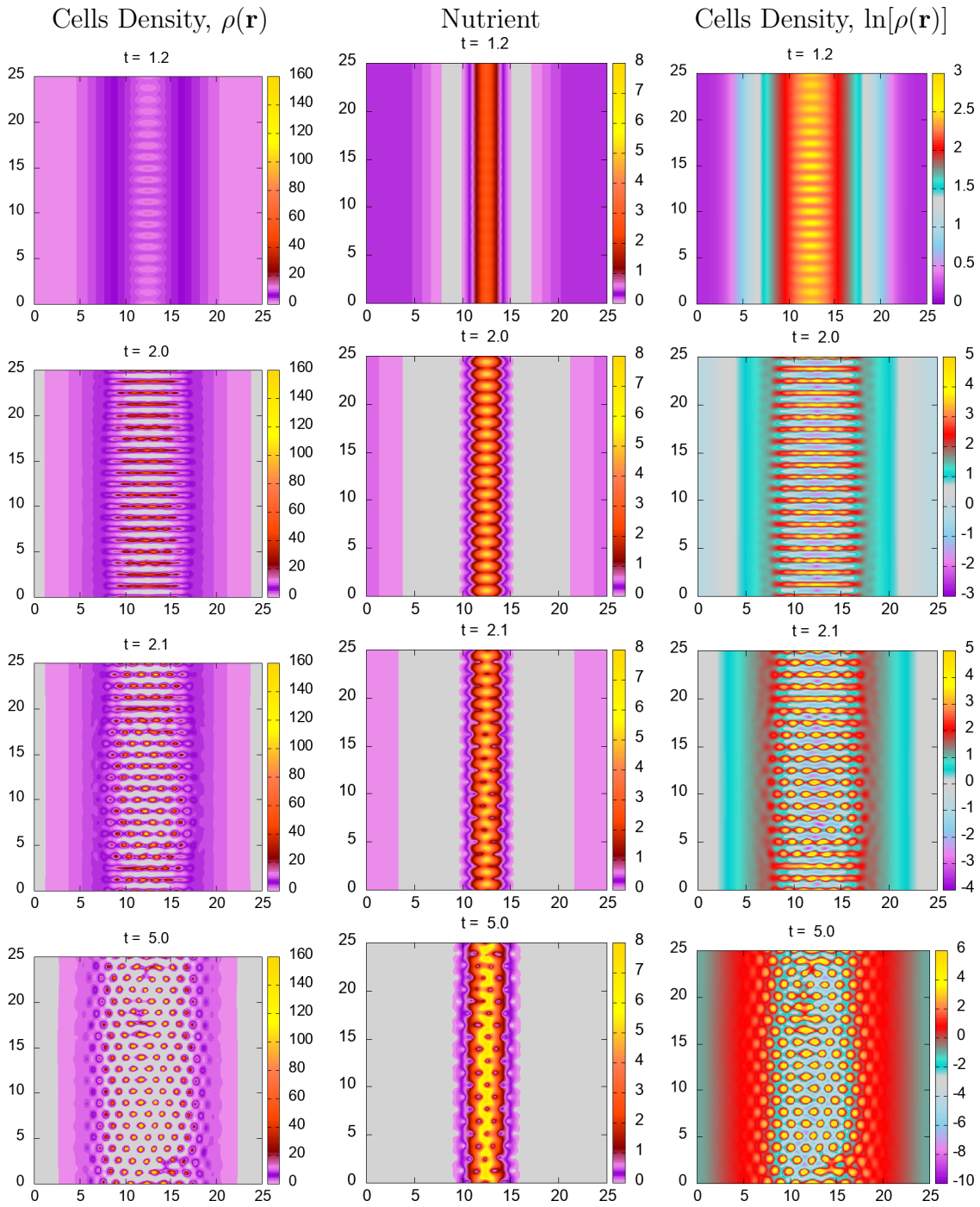

Figure 5.5: The local density of the cells (left column) for $\tilde{D}$=1, the nutrient density (middle column) and the logarithm of the cells density (right hand column). The population growth constant c_1=1 and the energy scale in the interaction potential between cells $\beta\varepsilon$=1. The nutrient source $\tilde{S}_n$=35 with $f(\mathbf{r})$ given in Eq.(4.4.5) and the nutrient uptake rate $\tilde{\lambda}_n$=1. The area of the model is 25.6^2 and Δx=0.05.

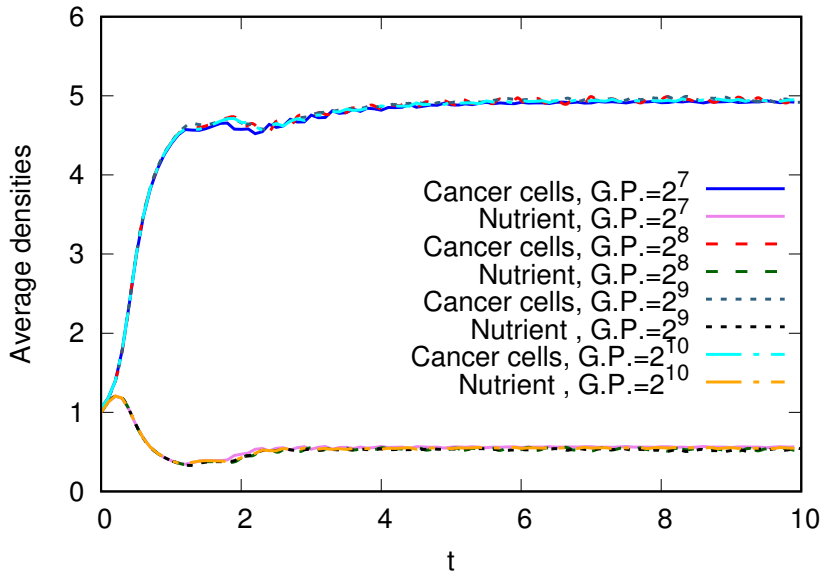

Figure 5.6: The average cell density, [see Eq.(5.5.14)] and the average nutrient density [see Eq.(5.5.15)], corresponding to the results in Fig. 5.5. These results are for varying numbers of grid points (G.P.), $= 2^7, 2^8, 2^9$ and 2^{10}.

cells increase with the time. We see the peaks (i.e. cells) grow and split to fill the entire domain, due the fact that there is a source of nutrient everywhere, in contrast to the behaviour seen e.g. in Figs. 5.5 or 5.7 where the source of nutrient is localised along the mid-line of the system. We plot in Fig. 5.11 the average cell density and nutrient density (over the whole system) as functions of time. Initially the nutrient density increases, due to the low initial average cell density. Then, as the cell density increases at $t \approx 0.5$, the nutrient density starts to decrease. During the time t=2–3 the peaks in the cells density distribution form. Consequently, the nutrient concentration then increases again at $t \approx 3$. After this, $\bar{n}(t)$ is a constant ≈ 1.2, as shown in Fig. 5.11. The cell density continues to slowly increase to plateau at a constant value ≈ 10 at time $t \approx 6$.

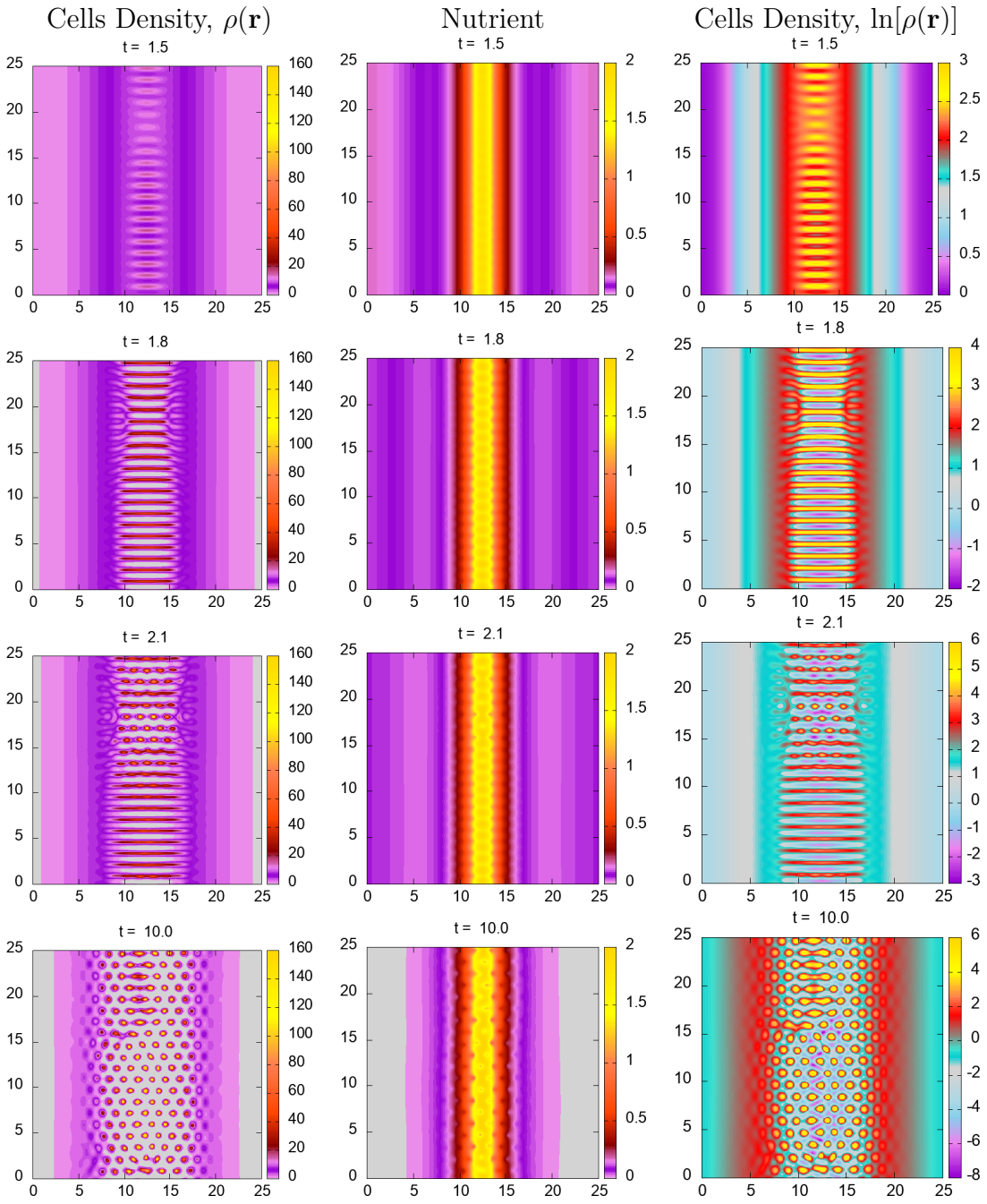

Figure 5.7: Profiles the same as in Fig. 5.5, except here $\tilde{D}$=10.

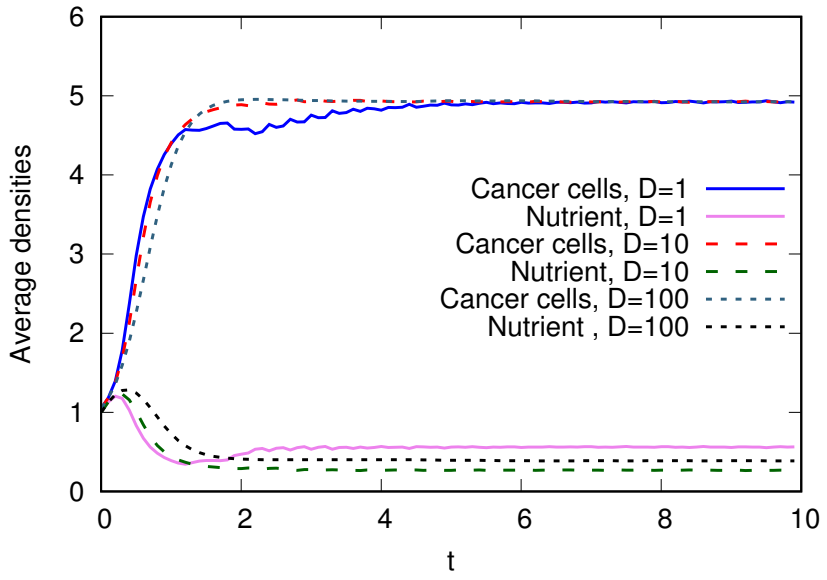

Figure 5.8: The average cell density, [see Eq.(5.5.14)] and the average nutrient density [see Eq.(5.5.15)], corresponding to the results in Figs. 5.5, 5.7 and 5.9 when the diffusion coefficient $\tilde{D}$=1, 10 and 100 respectively.

What the results in this chapter show is that we have developed a model that is able to describe cell dynamics, cell growth (including cell division), cell death due to a shortage of nutrients and also how the cell density field evolves coupled to the nutrient concentration field. In the following chapter we extend the model to describe two species of cells.

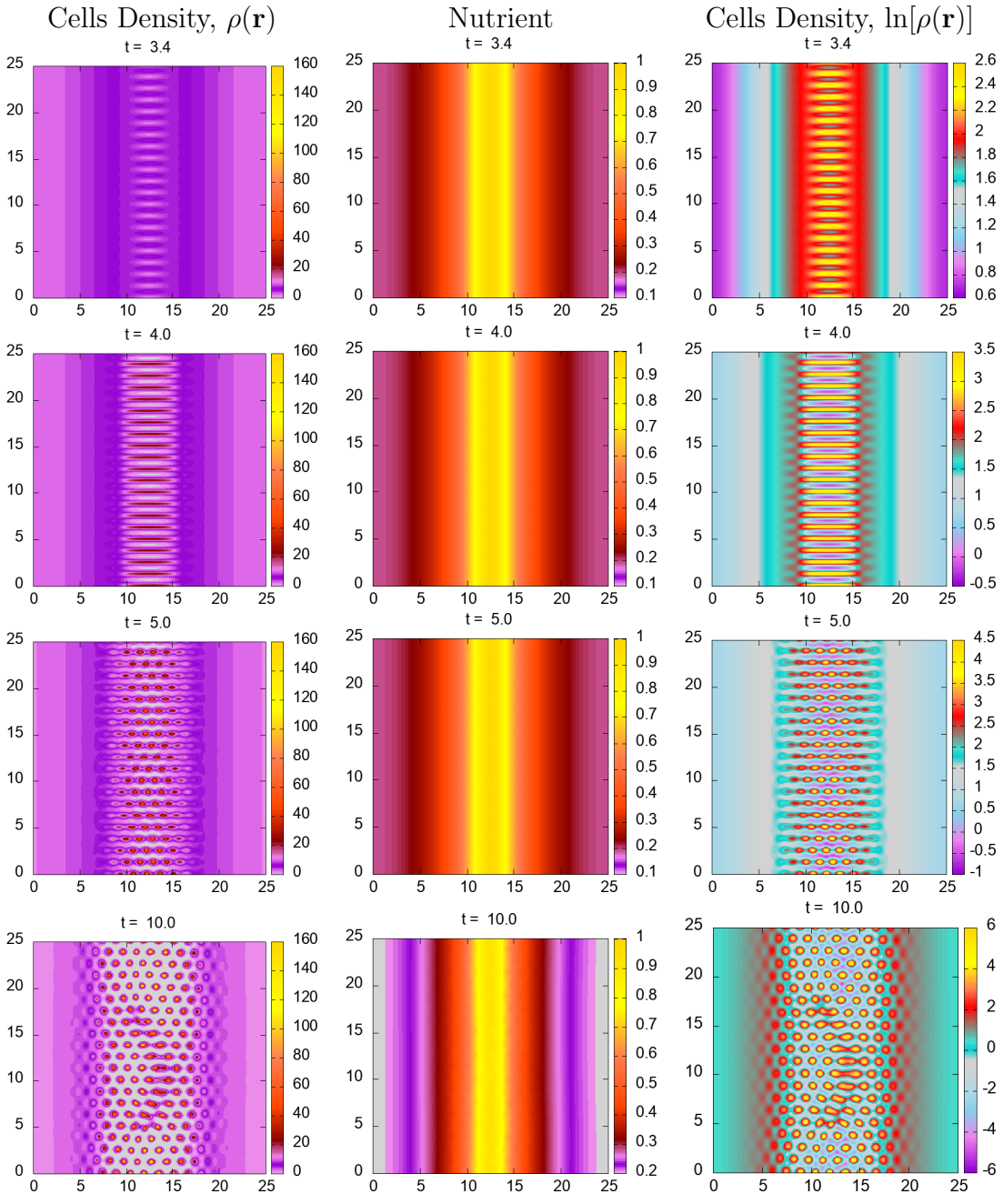

Figure 5.9: Profiles the same as in Figs. 5.5 and 5.7, except here $\tilde{D}$=100.

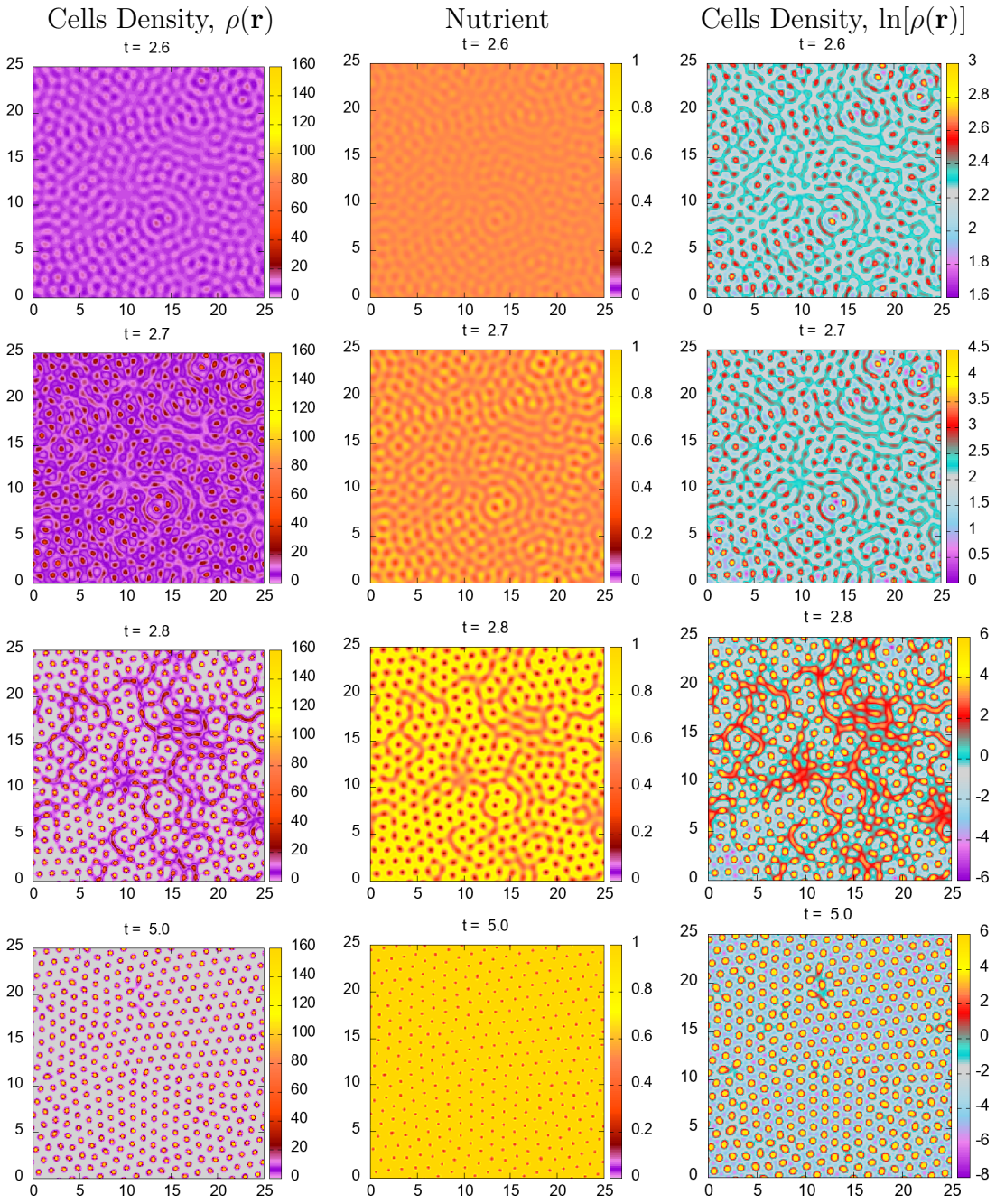

Figure 5.10: Profiles the same as in Fig. 5.5 which has $\tilde{D}$=1, except here the nutrient source is uniform with $f(\mathbf{r})$=1 and $\tilde{S}_n$=10.

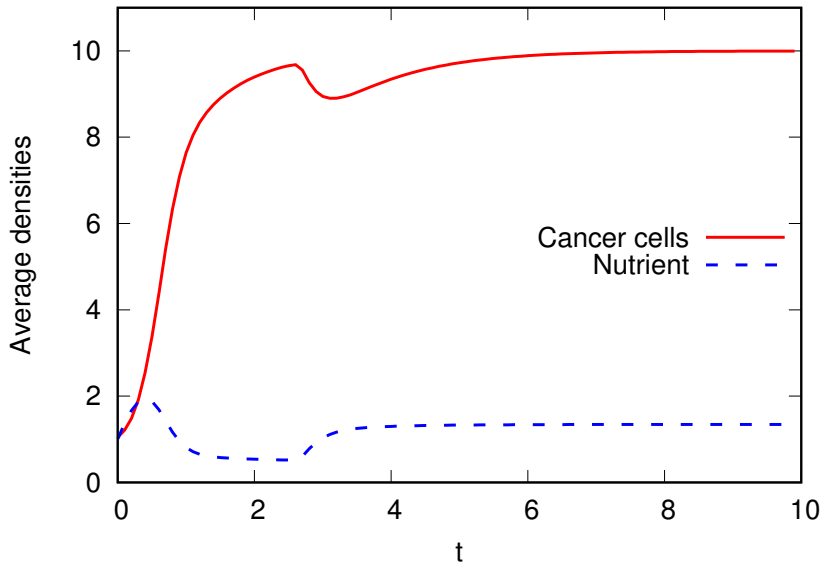

Figure 5.11: The average cell density, [see Eq.(5.5.14)] and the average nutrient density [see Eq.(5.5.15)], corresponding to the results in Fig. 5.10.

CHAPTER 6

MODEL INCLUDING COMPETITION BETWEEN CANCER AND HEALTHY CELLS

6.1 Introduction

In this chapter we extend the model discussed in chapter 5, to study the competition between cancer cells and healthy cells, i.e. we introduce a second species of cells. The model system of integro-partial differential equations for the time evolution of the density profile of the cancer cells, the healthy cells and nutrient is given by the following generalisation of Eqs. (4.3.1) and (4.4.7)

$$\frac{\partial \rho_1(\mathbf{r},t)}{\partial t} = \Gamma_1 \nabla \cdot \left[\rho_1(\mathbf{r},t) \nabla \left(\frac{\delta \mathcal{F}[\rho_1(\mathbf{r},t), \rho_2(\mathbf{r},t)]}{\delta \rho_1(\mathbf{r},t)} \right) \right] + [\lambda_{m1} n(\mathbf{r},t) - \lambda_{d1}] \rho_1(\mathbf{r},t),$$

$$\frac{\partial \rho_2(\mathbf{r},t)}{\partial t} = \Gamma_2 \nabla \cdot \left[\rho_2(\mathbf{r},t) \nabla \left(\frac{\delta \mathcal{F}[\rho_1(\mathbf{r},t), \rho_2(\mathbf{r},t)]}{\delta \rho_2(\mathbf{r},t)} \right) \right] + [\lambda_{m2} n(\mathbf{r},t) - \lambda_{d2}] \rho_2(\mathbf{r},t),$$

$$\frac{\partial n(\mathbf{r},t)}{\partial t} = D_n \nabla^2 n(\mathbf{r},t) + S_n f(\mathbf{r}) - \lambda_{n1} \rho_1(\mathbf{r},t) n(\mathbf{r},t)) - \lambda_{n2} \rho_2(\mathbf{r},t) n(\mathbf{r},t). \quad (6.1.1)$$

The generalisation of DDFT to two species of interacting Brownian particles was discussed in [153]. The above is the natural further generalisation to include cell birth and cell death and the coupling to the local nutrient concentration. The variables and parameters in the above system and their descriptions are summarised in Table 6.1.

For such a binary system we may approximate the intrinsic Helmholtz free energy as [134, 153]

$$\begin{aligned} \mathcal{F}[\{\rho_i(\mathbf{r},t)\}] &= k_B T \sum_{i=1}^{2} \int d\mathbf{r} \rho_i(\mathbf{r},t) \Big(\ln \left(\Lambda_i^2 \rho_i(\mathbf{r},t) \right) - 1 \Big) \\ &\quad + \frac{1}{2} \sum_{i,j=1}^{2} \int d\mathbf{r} \int d\mathbf{r}' \rho_i(\mathbf{r},t) \rho_j(\mathbf{r}',t) V_{ij}(|\mathbf{r} - \mathbf{r}'|). \end{aligned} \quad (6.1.2)$$

where V_{ij} are the pair interactions potentials, discussed further below. The indices $i, j = 1, 2$ label the two different species of particles (healthy and cancer); we assign 1 for cancer cells and 2 for healthy cells. The first variation of the free energy is

$$\frac{\delta \mathcal{F}}{\delta \rho_i(\mathbf{r},t)} = k_B T \ln \left(\Lambda_i^2 \rho_i(\mathbf{r},t) \right) + \sum_{j=1}^{2} \int d\mathbf{r}' \rho_j(\mathbf{r}',t) V_{ij}(|\mathbf{r} - \mathbf{r}'|). \quad (6.1.3)$$

Taking the gradient of Eq.(6.1.3) and substituting the result into Eq.(6.1.1), we

Table 6.1: Summary of the variables and parameters in the model given in Eqs. (6.1.4), (6.1.5) and (6.1.6).

State variables	Description
$\rho_1(\mathbf{r},t)$	Density of the cancer cells
$\rho_2(\mathbf{r},t)$	Density of the healthy cells
$n(\mathbf{r},t)$	Local concentration of nutrients
$N_1(t)$	Total number of cancer cells in the system
$N_2(t)$	Total number of healthy cells in the system
$\bar{\rho}_1(t)$	Average cancer cell density
$\bar{\rho}_2(t)$	Average healthy cell density
$\bar{n}(t)$	Average nutrient density
$V_{11}(\lvert\mathbf{r}-\mathbf{r}'\rvert)$	Interaction potential between cancer cells
$V_{12}(\lvert\mathbf{r}-\mathbf{r}'\rvert)$	Interaction potential between cancer and healthy cells
$V_{22}(\lvert\mathbf{r}-\mathbf{r}'\rvert)$	Interaction potential between healthy cells
$f(\mathbf{r})$	Function that defines where in space the nutrient source is located
λ_{d1}	Cancer cell death rate constant
λ_{d2}	Healthy cell death rate constant
λ_{n1}	Nutrient uptake rate constant for cancer cells
λ_{n2}	Nutrient uptake rate constant for healthy cells
λ_{m1}	Nutrient-dependent growth rate constant for cancer cells
λ_{m2}	Nutrient-dependent growth rate constant for healthy cells
D_c	Cancer cell diffusion coefficient
D_h	Healthy cell diffusion coefficient
Γ_1	Cancer cell motility coefficient
Γ_2	Healthy cell motility coefficient
T	Temperature
k_B	Boltzmann's constant
ρ_0	constant reference density
D_n	Nutrient diffusion coefficient
S_n	The nutrient source
Λ_1, Λ_2	Thermal de Broglie wavelengths

obtain

$$\frac{\partial \rho_1(\mathbf{r},t)}{\partial t} = \nabla \cdot \Bigg[\Gamma_1 \rho_1(\mathbf{r},t) \nabla \Bigg(k_B T \ln(\Lambda_1^2 \rho_1(\mathbf{r},t)) + \int d\mathbf{r}' \rho_1(\mathbf{r}',t) V_{11}(|\mathbf{r}-\mathbf{r}'|) + \int d\mathbf{r}' \rho_2(\mathbf{r}',t) V_{12}(|\mathbf{r}-\mathbf{r}'|) \Bigg) \Bigg] + \big[\lambda_{m1} n(\mathbf{r},t) - \lambda_{d1}\big] \rho_1(\mathbf{r},t), \quad (6.1.4)$$

$$\frac{\partial \rho_2(\mathbf{r},t)}{\partial t} = \nabla \cdot \Bigg[\Gamma_2 \rho_2(\mathbf{r},t) \nabla \Bigg(k_B T \ln(\Lambda_2^2 \rho_2(\mathbf{r},t)) + \int d\mathbf{r}' \rho_1(\mathbf{r}',t) V_{21}(|\mathbf{r}-\mathbf{r}'|) + \int d\mathbf{r}' \rho_2(\mathbf{r}',t) V_{22}(|\mathbf{r}-\mathbf{r}'|) \Bigg) \Bigg] + \big[\lambda_{m2} n(\mathbf{r},t) - \lambda_{d2}\big] \rho_2(\mathbf{r},t), \quad (6.1.5)$$

$$\frac{\partial n(\mathbf{r},t)}{\partial t} = D_n \nabla^2 n(\mathbf{r},t) + S_n f(\mathbf{r}) - \lambda_{n1} \rho_1(\mathbf{r},t) n(\mathbf{r},t)) - \lambda_{n2} \rho_2(\mathbf{r},t) n(\mathbf{r},t). \quad (6.1.6)$$

We model the interactions between the cells via pair potentials of the same form as in Chapter 5,

$$V_{ij}(r) = \varepsilon_{ij} e^{[-(r/R_{ij})^4]}, \quad (6.1.7)$$

where the indices $i, j = 1, 2$ labels the two different species of particles (cancer and healthy); we assign 1 for cancer cells and 2 for healthy cells. The parameter ε_{ij} specifies the strength of the repulsion between pairs of cells of species i and j and R_{ij} defines the range of the interaction. Thus we choose $R_{11} \leq R_{22}$, since cancer cells are generally a little smaller than the healthy cells and we choose $\varepsilon_{12} > \varepsilon_{11} = \varepsilon_{22}$ to make sure that density peaks of one species do not coincide with density peaks of the other. In some cases we choose $R_{12} = \frac{1}{2}(R_{11} + R_{22})$, but we also consider cases where $R_{12} > \frac{1}{2}(R_{11} + R_{22})$ since this promotes demixing of the two cell species and also $R_{12} < \frac{1}{2}(R_{11} + R_{22})$ which promotes penetration of the cancer cells in between the healthy cells [134, 153, 154].

6.2 Nondimensionalisation

We now nondimensionlise the system of integro-partial differential equations given in Eqs. (6.1.4), (6.1.5) and (6.1.6). We scale each of the variables as

$\rho_1 = \rho_1^*\hat{\rho}_1, \quad \rho_2 = \rho_2^*\hat{\rho}_2, \quad n = n^*\hat{n}, \quad t = t^*\hat{t}, \quad x = x^*/R_{11}, \quad y = y^*/R_{11}$ and $V_{ij}(r/R_{11}) = \varepsilon_{ij}\tilde{V}_{ij}(r^*)$,

where the quantities with a ˆ are the rescaling constants. As in Sec. 5.2.2, on substituting into Eq. (6.1.4) we obtain,

$$\begin{aligned}\frac{\partial(\rho_1^*(\mathbf{r},t)\hat{\rho}_1)}{\partial(t^*\hat{t})} &= \frac{1}{R_{11}}\nabla^*\cdot\left[\frac{\Gamma_1\hat{\rho}_1}{R_{11}}\rho_1^*(\mathbf{r},t)\nabla^*\Bigg(k_BT\ln\rho_1^*(\mathbf{r},t)\right.\\ &\quad +R_{11}^2\hat{\rho}_1\varepsilon_{11}\int d\mathbf{r}'\rho_1^*(\mathbf{r}',t)\tilde{V}_{11}(|\mathbf{r}-\mathbf{r}'|)\\ &\quad \left.+R_{11}^2\hat{\rho}_1\varepsilon_{12}\int d\mathbf{r}'\rho_2^*(\mathbf{r}',t)\tilde{V}_{12}(|\mathbf{r}-\mathbf{r}'|)\Bigg)\right]\\ &\quad +[\lambda_{m1}n^*(\mathbf{r},t)\hat{n}-\lambda_{d1}]\rho_1^*(\mathbf{r},t)\hat{\rho}_1, \qquad (6.2.1)\end{aligned}$$

noting that constants Λ_i drop out because $\nabla\ln\Lambda^2\rho = \frac{1}{\rho}\nabla\rho$. This can be simplified to

$$\begin{aligned}\frac{\partial\rho_1^*(\mathbf{r},t)}{\partial t^*} &= \left(\frac{\hat{t}}{\hat{\rho}_1}\frac{\Gamma_1k_BT\hat{\rho}_1}{R_{11}^2}\right)\nabla^*\cdot\left[\rho_1^*(\mathbf{r},t)\nabla^*\Bigg(\ln\rho_1^*(\mathbf{r},t)\right.\\ &\quad +R_{11}^2\hat{\rho}_1\beta\varepsilon_{11}\int d\mathbf{r}'\rho_1^*(\mathbf{r}',t)\tilde{V}_{11}(|\mathbf{r}-\mathbf{r}'|)\\ &\quad \left.+R_{11}^2\hat{\rho}_1\beta\varepsilon_{12}\int d\mathbf{r}'\rho_2^*(\mathbf{r}',t)\tilde{V}_{12}(|\mathbf{r}-\mathbf{r}'|)\Bigg)\right]\\ &\quad +\hat{t}\lambda_{d1}\left[\left(\frac{\lambda_{m1}\hat{n}}{\lambda_{d1}}\right)n^*(\mathbf{r},t)-1\right]\rho_1^*(\mathbf{r},t), \qquad (6.2.2)\end{aligned}$$

where the cancer cells diffusion coefficient $D_c = \Gamma_1k_BT$ and the healthy cells diffusion coefficient $D_h = \Gamma_2k_BT$. By choosing $\hat{t} = \frac{R_{11}^2}{D_c}$, $\hat{\rho}_1 = \hat{\rho}_2 = \frac{1}{R_{11}^2}$ and $\hat{n} = \frac{\lambda_{d1}}{\lambda_{m1}}$, dropping

the superscript * for clarity, we obtain

$$\begin{aligned}\frac{\partial\rho_1(\mathbf{r},t)}{\partial t} &= \nabla^2\rho_1(\mathbf{r},t)+\nabla\cdot\left(\rho_1(\mathbf{r},t)\nabla\int d\mathbf{r}'\rho_1(\mathbf{r}',t)\beta\varepsilon_{11}\tilde{V}_{11}(|\mathbf{r}-\mathbf{r}'|)\right)\\ &\quad+\nabla\cdot\left(\rho_1(\mathbf{r},t)\nabla\int d\mathbf{r}'\rho_2(\mathbf{r}',t)\beta\varepsilon_{12}\tilde{V}_{12}(|\mathbf{r}-\mathbf{r}'|)\right)\\ &\quad+c_1\big[n(\mathbf{r},t)-1\big]\rho_1(\mathbf{r},t),\end{aligned}\tag{6.2.3}$$

where the dimensionless growth constant for cancer cells is

$$c_1=\frac{R_{11}^2\lambda_{d1}}{D_c}.\tag{6.2.4}$$

Now by the same technique for Eq.(6.1.5), we get

$$\begin{aligned}\frac{\partial(\rho_2^*(\mathbf{r},t)\hat{\rho}_2)}{\partial(t^*\hat{t})} &= \frac{1}{R_{11}}\nabla^*\cdot\left[\frac{\Gamma_2\hat{\rho}_2}{R_{11}}\rho_2^*(\mathbf{r},t)\nabla^*\Big(k_BT\ln\rho_2^*(\mathbf{r},t)\right.\\ &\quad+R_{11}^2\hat{\rho}_2\varepsilon_{21}\int d\mathbf{r}'\rho_1^*(\mathbf{r}',t)\tilde{V}_{21}(|\mathbf{r}-\mathbf{r}^{'}|)\\ &\quad\left.+R_{11}^2\hat{\rho}_2\varepsilon_{22}\int d\mathbf{r}'\rho_2^*(\mathbf{r}',t)\tilde{V}_{22}(|\mathbf{r}-\mathbf{r}^{'}|)\Big)\right]\\ &\quad+\big[\lambda_{m2}n^*(\mathbf{r},t)\hat{n}-\lambda_{d2}\big]\rho_2^*(\mathbf{r},t)\hat{\rho}_2.\end{aligned}\tag{6.2.5}$$

This can be simplified to

$$\begin{aligned}\frac{\partial\rho_2^*(\mathbf{r},t)}{\partial t^*} &= \left(\frac{\hat{t}}{\hat{\rho}_2}\frac{\Gamma_2k_BT\hat{\rho}_2}{R_{11}^2}\right)\nabla^*\cdot\left[\rho_2^*(\mathbf{r},t)\nabla^*\Big(\ln\rho_2^*(\mathbf{r},t)\right.\\ &\quad+R_{11}^2\hat{\rho}_2\beta\varepsilon_{12}\int d\mathbf{r}'\rho_1^*(\mathbf{r}',t)\tilde{V}_{21}(|\mathbf{r}-\mathbf{r}^{'}|)\\ &\quad\left.+R_{11}^2\hat{\rho}_2\beta\varepsilon_{22}\int d\mathbf{r}'\rho_2^*(\mathbf{r}',t)\tilde{V}_{22}(|\mathbf{r}-\mathbf{r}^{'}|)\Big)\right]\\ &\quad+\hat{t}\big[\lambda_{m2}n^*(\mathbf{r},t)\hat{n}-\lambda_{d2}\big]\rho_2^*(\mathbf{r},t),\end{aligned}\tag{6.2.6}$$

where the healthy cells diffusion coefficient $D_h = \Gamma_2 k_B T$ and using the previously defined cell diffusion coefficients, dropping the superscript *, we obtain

$$\begin{aligned}\frac{\partial \rho_2(\mathbf{r},t)}{\partial t} &= \tilde{D}_1 \nabla^2 \rho_2(\mathbf{r},t) + \nabla \cdot \left(\rho_2(\mathbf{r},t) \nabla \int d\mathbf{r}' \rho_1(\mathbf{r}',t) \beta \varepsilon_{21} \tilde{V}_{21}(|\mathbf{r}-\mathbf{r}'|) \right) \\ &\quad + \nabla \cdot \left(\rho_2(\mathbf{r},t) \nabla \int d\mathbf{r}' \rho_2(\mathbf{r}',t) \beta \varepsilon_{22} \tilde{V}_{22}(|\mathbf{r}-\mathbf{r}'|) \right) \\ &\quad + c_2 \big[n(\mathbf{r},t) - \alpha \big] \rho_2(\mathbf{r},t), \end{aligned} \tag{6.2.7}$$

where $\tilde{D}_1 = \frac{D_h}{D_c}$, the dimensionless growth constant for the healthy cells is

$$c_2 = \frac{R_{11}^2 \lambda_{m2} \lambda_{d1}}{D_c \lambda_{m1}} \tag{6.2.8}$$

and the dimensionless threshold nutrient concentration for healthy cells is

$$\alpha = \frac{\lambda_{d2} \lambda_{m1}}{\lambda_{d1} \lambda_{m2}}. \tag{6.2.9}$$

Now consider Eq. (6.1.6). We obtain,

$$\frac{\partial (n^*(\mathbf{r},t)\hat{n})}{\partial (t^* \hat{t})} = D_n \nabla^{*2} n^*(\mathbf{r},t)\hat{n} + S_n f(\mathbf{r}) - \lambda_{n1} \rho_1^*(\mathbf{r},t) \hat{\rho}_1 n^*(\mathbf{r},t)\hat{n} - \lambda_{n2} \rho_2^*(\mathbf{r},t) \hat{\rho}_2 n^*(\mathbf{r},t)\hat{n},$$

which can be rearanged to obtain

$$\frac{\partial n^*(\mathbf{r},t)}{\partial t^*} = \frac{D_n \hat{t}}{R_{11}^2} \nabla^{*2} n^*(\mathbf{r},t) + \frac{S_n \hat{t}}{\hat{n}} f(\mathbf{r}) - \frac{\hat{t}}{\hat{n}} \lambda_{n1} \rho_1^*(\mathbf{r},t) \hat{\rho}_1 n^*(\mathbf{r},t)\hat{n} - \frac{\hat{t}}{\hat{n}} \lambda_{n2} \rho_2^*(\mathbf{r},t) \hat{\rho}_2 n^*(\mathbf{r},t)\hat{n}.$$

From the definition of $\hat{n}, \hat{t}$, $\hat{\rho}_1$ and $\hat{\rho}_2$, we get

$$\begin{aligned}\frac{\partial n^*(\mathbf{r},t)}{\partial t^*} &= \left(\frac{D_n}{D_c}\right)\nabla^{*2}n^*(\mathbf{r},t) + \left(\frac{R_{11}^2 S_n \lambda_{m1}}{\lambda_{d1} D_c}\right) f(\mathbf{r}) - \left(\frac{\lambda_{n1}}{D_c}\right)\rho_1^*(\mathbf{r},t)n^*(\mathbf{r},t) \\ &\quad - \left(\frac{\lambda_{n2}}{D_c}\right)\rho_2^*(\mathbf{r},t)n^*(\mathbf{r},t).\end{aligned}$$

Writing

$$\tilde{D}_2 = \frac{D_n}{D_c}, \quad \tilde{S}_n = \frac{R_{11}^2 S_n \lambda_{m1}}{\lambda_{d1} D_c}, \quad \tilde{\lambda}_{n1} = \frac{\lambda_{n1}}{D_c} \;\; and \;\; \tilde{\lambda}_{n2} = \frac{\lambda_{n2}}{D_c}, \tag{6.2.10}$$

and omitting the superscript $*$, we get

$$\frac{\partial n(\mathbf{r},t)}{\partial t} = \tilde{D}_2\nabla^2 n(\mathbf{r},t) + \tilde{S}_n f(\mathbf{r}) - \tilde{\lambda}_{n1}\rho_1(\mathbf{r},t)n(\mathbf{r},t) - \tilde{\lambda}_{n2}\rho_2(\mathbf{r},t)n(\mathbf{r},t). \tag{6.2.11}$$

The above equation together with Eq.(6.2.3) and Eq.(6.2.7) constitutes the non-dimensionalised model equations that we study.

6.3 Parameter values

For both the healthy and cancer cell growth rate parameters, diffusion coefficients, etc. and the parameters related to the nutrient dynamics we use the same values as in Sec. 5.3 for the model with only one species of cells. The main change is to make the growth rate parameters for cancer cells larger than those of the healthy cells in order for them reproduce and grow faster (or die slower) than the healthy cells. The parameter values are summarised in Table 6.2 and the corresponding dimensionless parameter values are given in Table 6.3. The other main addition in the model for both healthy and cancer cells that must be considered are the parameter values for

the interaction potential between the different types of cells, given in Eq. (6.1.7). The parameter values we choose are given in Table 6.2. These values are chosen in order to (i) make the cancer cells either the same size or slightly smaller than the healthy cells [155] and also (ii) to make sure the cancer cells do not overlap with the healthy cells.

Table 6.2: Model parameters and their units (note c. = cancer and h. = healthy). Values marked with asterisk (*) are estimates from Sections 5.3 and 6.3.

Symbol	Description	typical value	Unit	Source
$\rho_1(\mathbf{r},t)$	Number density of the cancer cells	$3\times10^5*$	cm^{-2}	estimated
$\rho_2(\mathbf{r},t)$	Number density of the healthy cells	$3\times10^5*$	cm^{-2}	estimated
$n(\mathbf{r},t)$	Local concentration of nutrients	3 *	mg/L	*estimated*
$V_{11}(\lvert\mathbf{r}-\mathbf{r}'\rvert)$	Interaction potential for c. cells	ε_{11}/k_BT	dimensionless	§3.3
$V_{12}(\lvert\mathbf{r}-\mathbf{r}'\rvert)$	Interaction potential for c. and h. cells	ε_{12}/k_BT	dimensionless	§3.3
$V_{22}(\lvert\mathbf{r}-\mathbf{r}'\rvert)$	Interaction potential for h.cells.	ε_{22}/k_BT	dimensionless	§3.3
R_{11}	Radius of the cancer cells	0.001	cm	[145]
R_{22}	Radius of the healthy cells	0.0011	cm	[145]
λ_{m1}	Nutrient-dependent growth rate for c. cells	0.00015 *	min^{-1}	estimated
λ_{m2}	Nutrient-dependent growth rate for h. cells	0.000015 *	min^{-1}	estimated
λ_{d1}	Cancer cell death rate constant	0.00005 *	min^{-1}	estimated
λ_{d2}	Healthy cell death rate constant	0.00001 *	min^{-1}	estimated
λ_{n1}	Nutrient uptake rate for cancer cells	3 *	min^{-1}	estimated
λ_{n2}	Nutrient uptake rate for healthy cells	3 *	min^{-1}	estimated
D_c	Diffusion coefficient of cancer cells	1.3×10^{-9} *	cm^2 min^{-1}	estimated
D_h	Diffusion coefficient of healthy cells	1.1×10^{-9} *	cm^2 min^{-1}	estimated
D_n	Diffusion coefficient of nutrient	0.0012	cm^2min^{-1}	[24]
Γ_1	Cancer cell motility coefficient	3×10^{10}	$ming^{-1}$	§6.2
Γ_2	Healthy cell motility coefficient	2.5×10^{10}	$ming^{-1}$	§6.2
T	Temperature	310	K	[145]
k_B	Boltzmann's constant	1.38×10^{-23}	$Joule/K$	[146]
ε_{11}	Energy scale in interaction potential between c. cells	1 k_BT	$Joule$	§3.3
ε_{12}	Energy scale in interaction pot. c. and h. cells.	1.5 k_BT	$Joule$	§3.3
ε_{22}	Energy scale in interaction potential between h. cells	1 k_BT	$Joule$	§3.3
ρ_0	A constant reference density	3×10^5	cm^{-2}	§5.5.3.1
L^2	Area of the system	6×10^{-4}	cm^2	§5.5.3.1
S_n	Nutrient in take flux	433 *	$mgL^{-1}min^{-1}cm^{-2}$	estimated

Table 6.3: Dimensionless parameter values of the model.

Nondimensional parameter	Dimension form	value	Used value
ρ_1^*	$\rho_1/\hat{\rho}_1$	1	$6+\gamma(\mathbf{r})$
ρ_2^*	$\rho_2/\hat{\rho}_2$	1	$6+\gamma(\mathbf{r})$
n^*	$n/\hat{n}$	3	3
c_1	$R_{11}^2\lambda_{d1}/D_c$	0.038	0.5, 0.6
c_2	$R_{11}^2\lambda_{m2}\lambda_{d1}/D_c\lambda_{m1}$	0.0038	0.5, 0.6
α	$\lambda_{d2}\lambda_{m1}/\lambda_{d1}\lambda_{m2}$	2	2
$\tilde{D}_1$	D_h/D_c	1.1	1
$\tilde{D}_2$	D_n/D_c	10^6	1
$\tilde{S}_n$	$R_{11}^2 S_n\lambda_{m1}/\lambda_{d1}D_c$	10^6	8, 9, 60
$\tilde{\lambda}_{n1}$	λ_{n1}/D_c	10^6	1
$\tilde{\lambda}_{n2}$	λ_{n2}/D_c	10^6	1
$\varepsilon_{11}\tilde{V}_{11}(r^*)$	$V_{11}(r/R_{11})$	See Eq. (6.1.7)	ε_{11}/k_BT
$\varepsilon_{12}\tilde{V}_{12}(r^*)$	$V_{12}(r/R_{11})$	See Eq. (6.1.7)	ε_{12}/k_BT
$\varepsilon_{22}\tilde{V}_{22}(r^*)$	$V_{22}(r/R_{11})$	See Eq. (6.1.7)	ε_{22}/k_BT

6.4 Linear stability analysis for two species system

The governing equations for the time evolution of the density profile of the cancer cells, the healthy cells and the nutrient are given by Eqs. (6.2.3), (6.2.7) and (6.2.11). We note that for $\alpha \neq 1$ there is no spatially uniform positive steady-state to this system. We consider here the linear stability of uniform state $\rho_1 = \rho_1^b > 0$ and $\rho_2 = \rho_2^b > 0$ for the case $c_1, c_2 \ll \xi \ll 1$, where ξ is the amplitude of the density perturbation; the small magnitude of c_1 and c_2 in comparison to the other parameters is evident from Table 6.3. In setting $c_1 = c_2 = 0$ for the purposes of the linear stability analysis, we are assuming the growth of cells occurs on a much longer time scale than that of the cell motion. This assumption means that the nutrient equation (6.2.11) decouples from Eqs. (6.2.3) and (6.2.7), so that in what follows, the stability of uniform states is predominantly governed by cell density and the cell-cell interaction process.

We assume the cell density perturbations are of the form

$$\begin{aligned}\rho_1(\mathbf{r},t) &= \rho_1^b + \delta\rho(\mathbf{r},t) \\ &= \rho_1^b + \xi e^{i(\mathbf{k}.\mathbf{r})+\omega t},\end{aligned} \tag{6.4.1}$$

and

$$\begin{aligned}\rho_2(\mathbf{r},t) &= \rho_2^b + \chi\delta\rho(\mathbf{r},t) \\ &= \rho_2^b + \chi\xi e^{i(\mathbf{k}.\mathbf{r})+\omega t},\end{aligned} \tag{6.4.2}$$

where $0 < \xi \ll 1$, k is the wavenumber, χ is the ratio between the amplitude of the perturbation in the two components and the growth or decay rate is determined by the dispersion relation $\omega = \omega(k)$, where $k = |\mathbf{k}|$. The growth/decay rate of this model is given by the dispersion relation $\omega = \omega(k)$, where $k = |\mathbf{k}|$. If we substitute Eqs. (6.4.1) and (6.4.2) into Eq. (6.2.3), we get

$$\begin{aligned}\omega\delta\rho(\mathbf{r},t) &= -k^2\delta\rho(\mathbf{r},t) \\ &+\nabla\cdot\left[\left(\rho_1^b+\delta\rho(\mathbf{r},t)\right)\nabla\left(\int d\mathbf{r}'(\rho_1^b+\delta\rho(\mathbf{r}',t))\beta\varepsilon_{11}\tilde{V}_{11}(|\mathbf{r}-\mathbf{r}'|)\right)\right] \\ &+\nabla\cdot\left[\left(\rho_2^b+\chi\delta\rho(\mathbf{r},t)\right)\nabla\left(\int d\mathbf{r}'(\rho_2^b+\chi\delta\rho(\mathbf{r}',t))\beta\varepsilon_{12}\tilde{V}_{12}(|\mathbf{r}-\mathbf{r}'|)\right)\right].\end{aligned} \tag{6.4.3}$$

As before, when going from Eq. (5.4.4) to Eq. (5.4.8), we obtain

$$\omega\delta\rho(\mathbf{r},t) = -k^2[1+\rho_1^b\beta\varepsilon_{11}\hat{V}_{11}(k)+\rho_2^b\chi\beta\varepsilon_{12}\hat{V}_{12}(k)]\delta\rho(\mathbf{r},t)+O(\delta\rho^2), \tag{6.4.4}$$

where $\hat{V}_{ij}(k)$ is the Fourier transform of $V_{ij}(r)$, defined as in Eq. (5.4.7). Dividing

both sides by $\delta\rho(\mathbf{r},t)$ and neglecting terms $O(\delta\rho)$ and higher we get

$$\omega(k) = -k^2(1 + \rho_1^b\beta\varepsilon_{11}\hat{V}_{11}(k) + \rho_2^b\chi\beta\varepsilon_{12}\hat{V}_{12}(k)). \tag{6.4.5}$$

In the same way, if we substitute Eqs. (6.4.1) and (6.4.2) into Eq. (6.2.7), we get

$$\chi\omega(k) = -k^2(\chi + \rho_1^b\beta\varepsilon_{21}\hat{V}_{21}(k) + \rho_2^b\chi\beta\varepsilon_{22}\hat{V}_{22}(k)). \tag{6.4.6}$$

Eqs. (6.4.5) and (6.4.6) can be represented in matrix form, allowing for easier analysis,

$$\omega(k)\begin{pmatrix}1\\ \chi\end{pmatrix} = \mathbf{M}\begin{pmatrix}1\\ \chi\end{pmatrix}, \tag{6.4.7}$$

where

$$\mathbf{M} = -k^2\begin{pmatrix}1 + \rho_1^b\beta\varepsilon_{11}\hat{V}_{11}(k) & \rho_2^b\beta\varepsilon_{12}\hat{V}_{12}(k)\\ \rho_1^b\beta\varepsilon_{21}\hat{V}_{21}(k) & 1 + \rho_2^b\beta\varepsilon_{22}\hat{V}_{22}(k)\end{pmatrix}. \tag{6.4.8}$$

We can rewrite the matrix $\mathbf{M}$ as a product of two matrices $\mathbf{N}$ and $\mathbf{E}$ as follows,

$$\mathbf{M} = \mathbf{N}\cdot\mathbf{E} \tag{6.4.9}$$

where

$$\mathbf{N} = \begin{pmatrix}-\rho_1^b k^2 & 0\\ 0 & -\rho_2^b k^2\end{pmatrix}, \tag{6.4.10}$$

and

$$\mathbf{E} = \begin{pmatrix}\left[\frac{1}{\rho_1^b} + \beta\varepsilon_{11}\hat{V}_{11}(k)\right] & \beta\varepsilon_{12}\hat{V}_{12}(k)\\ \beta\varepsilon_{21}\hat{V}_{21}(k) & \left[\frac{1}{\rho_2^b} + \beta\varepsilon_{22}\hat{V}_{22}(k)\right]\end{pmatrix}. \tag{6.4.11}$$

We can now determine the dispersion relation $\omega(k)$ by calculating the eigenvalues of

$\mathbf{N}\cdot\mathbf{E}$,

$$\omega(k)=\frac{\mathrm{Tr}(\mathbf{N}\cdot\mathbf{E})}{2}\pm\sqrt{\frac{\mathrm{Tr}(\mathbf{N}\cdot\mathbf{E})^2}{4}-|\mathbf{N}\cdot\mathbf{E}|}, \tag{6.4.12}$$

where $|\mathbf{N}\cdot\mathbf{E}|$ denotes the determinant of the matrix $\mathbf{N}\cdot\mathbf{E}$ [149]. When $\omega(k)<0$ for all wave numbers k, the system is linearly stable. If, however, $\omega(k)>0$ for any wave number k, then the uniform density state is linearly unstable. Since $\mathbf{N}$ is a (negative definite) diagonal matrix its inverse $\mathbf{N}^{-1}$ exists for all nonzero densities and temperatures, enabling us to write Eq. (6.4.7) as the generalised eigenvalue problem

$$(\mathbf{E}-\mathbf{N}^{-1}\omega)\hat{\chi}=0, \tag{6.4.13}$$

where $\hat{\chi}=(1,\chi)$.

As $\mathbf{E}$ is a symmetric matrix, all eigenvalues are real. It follows that the linear stability threshold is determined by $|\mathbf{E}|=0$, i.e. by the condition [149]

$$D(k)\equiv[1+\rho_1^b\beta\varepsilon_{11}\hat{V}_{11}(k)][1+\rho_2^b\beta\varepsilon_{22}\hat{V}_{22}(k)]-\rho_1^b\rho_2^b\beta^2\varepsilon_{12}^2\hat{V}_{12}^2(k)=0. \tag{6.4.14}$$

In Fig. 6.1 we display the linear stability threshold for different values of the concentration $\phi\equiv\rho_1/\rho$, where $\rho\equiv\rho_1+\rho_2$ is the total density and ρ_1, ρ_2 are densities of cancer and healthy cells respectively. For points above the linear stability threshold line in Fig. 6.1, the system forms peaks, modelling the distribution of the cells. The instability line is obtained by tracing the locus defined by $D(k_c)=0$ and $D'(k_c)=0$, where $D(k)$ is given by Eq. (6.4.14) and $k_c\neq 0$ is the wave number at the minimum of $D(k)$ [i.e. $D(k=k_c)=0$]. Note that if R_{22}/R_{11} is further increased, then the two wavenumbers at which the system can become linearly unstable $k_{c_1}\approx 2\pi/R_{11}$ and $k_{c_2}\approx 2\pi/R_{22}$ move apart leading to the linear stability threshold to develop a

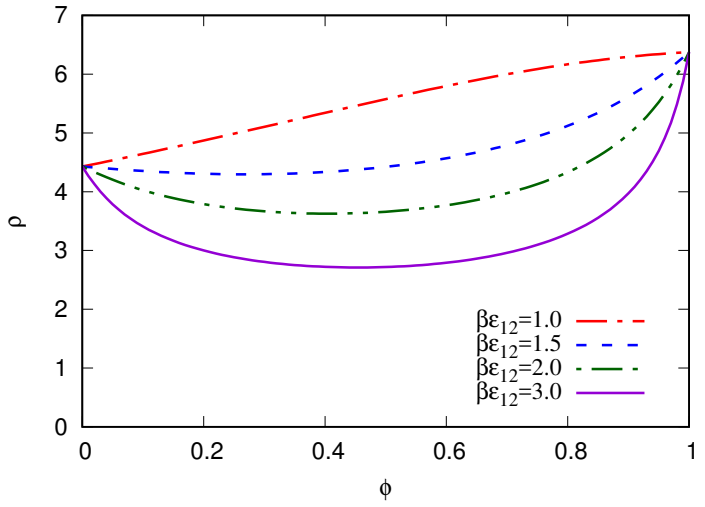

Figure 6.1: The linear stability limit for the two species cells [see Eqs. (6.2.3) and (6.2.7)] with $R_{22}/R_{11} = 1.2$, $R_{12}/R_{11} = 1.1$, $\beta\varepsilon_{11} = 1$, $\beta\varepsilon_{22} = 1$ and for varying $\beta\varepsilon_{12}$ as given in the key, plotted in the total density $\rho \equiv \rho_1 + \rho_2$ versus concentration $\phi \equiv \rho_1/\rho$ plane. The uniform density state is linearly unstable above this line.

cusp, see Fig. 6.2 for several examples. The cusp corresponds to a discontinuity of the first derivative along the linear stability threshold line. When a cusp exists, at the cusp point the system is marginally unstable at two distinct wave numbers.

The cusp appears when the two minima of $D(k)$ first appear and have $D(k_c) = 0$. Thus, the parameter values at which this occurs can be determined by simultaneously solving the system of algebraic equations

$$D(k_c) = 0, \tag{6.4.15}$$

$$\frac{d}{dk}[D(k_c)] = 0, \tag{6.4.16}$$

$$\frac{d^2}{dk^2}[D(k_c)] = 0, \tag{6.4.17}$$

$$\frac{d^3}{dk^3}[D(k_c)] = 0. \tag{6.4.18}$$

We find that the cusp appears at R_{22}/R_{11}=1.73, ρ=8.26 and ϕ=0.74, (red curve in

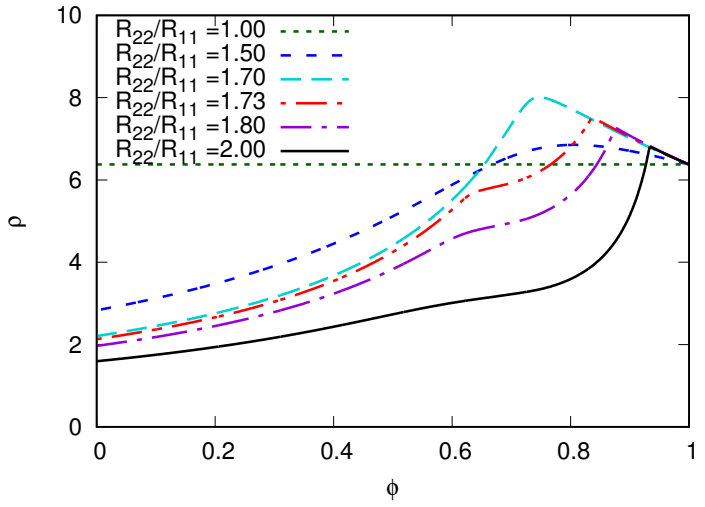

Figure 6.2: The linear stability limit for the two species cells [see Eqs. (6.2.3) and (6.2.7)] plotted in the total density $\rho \equiv \rho_1 + \rho_2$ versus concentration $\phi \equiv \rho_1/\rho$ plane. The curves are for varying $R_{22}/R_{11} = 1, 1.5, 1.7, 1.73, 1.8$ and 2. We set the cross-interaction radius $R_{12} = \frac{1}{2}(R_{11}+R_{22})$ and $\beta\varepsilon_{11}$= $\beta\varepsilon_{12}$=$\beta\varepsilon_{22}$=1. The uniform density state is linearly unstable above this line.

Fig. 6.2) and is present for $R_{22}/R_{11} > 1.73$. The onset wavenumber $k_c R_{11}$=4.31. The linear stability threshold line including this point is displayed in Fig. 6.2 along with the linear stability threshold for various other values of R_{22}.

6.5 Results for cancer invading healthy tissue

6.5.1 Results with a homogeneous nutrient source

In this section we discuss some representative results showing the competition between healthy and cancer cells, obtained by solving numerically the system of integro-partial differential Eqs. (6.2.3), (6.2.7) and (6.2.11) using the numerical methods discussed in Sec. 5.5. We investigate the evolution of the cells starting from various different initial arrangements and the effect of the cross-species interaction range R_{12}. Table 6.4 summarises all of the parameter values used in the simulations presented below. With each type of initial conditions we test three cases for the parameter R_{12} such that $R_{12} = \frac{1}{2}(R_{11} + R_{22})$ in the first case, then $R_{12} < \frac{1}{2}(R_{11} + R_{22})$ and finally $R_{12} > \frac{1}{2}(R_{11} + R_{22})$ according to the discussion in Sec. 6.1.

6.5.1.1 Half-half domain case

In this section, we assume that the population growth constant for both the cancer and the healthy cells are c_1=c_2 =0.5 and the threshold nutrient concentration for healthy cells $\alpha = 2$ [c.f. Eq. (6.2.9)]. We fix the energy scale in the interaction potential between both cancer cells and healthy cells to be $\beta\varepsilon_{11} = \beta\varepsilon_{22} = 1$, and the energy scale in the interaction potential between different species to be $\beta\varepsilon_{12} = 1.5$, so that density peaks of the two different cell types do not overlap. The nutrient uptake rate for cancer cells $\tilde{\lambda}_{n1} = 1$ and for healthy cells $\tilde{\lambda}_{n2} = 1$. We set the area of the domain in which the model is solved to be 25.6×25.6 and nutrient source to be uniform with constant $f(\mathbf{r}) = 1$ and $\tilde{S}_n = 8$. The diffusion coefficient $\tilde{D}_c = 1$ for cancer cells and the diffusion coefficient $\tilde{D}_h = 1$ for healthy cells. We use periodic boundary conditions on all sides. The initial conditions are

Table 6.4: Dimensionless parameter values of the different examples

Density of cells	R_{11}	R_{12}	R_{22}	$\beta\varepsilon_{12}$	c_1	c_2	$\tilde{D}_c$	$\tilde{D}_h$	$\tilde{S}_n$	$\tilde{\lambda}_{n1}$	$\tilde{\lambda}_{n2}$
Fig. 6.3	1	0.9	1	1.5	0.5	0.5	1	1	8	1	1
Fig. 6.4	1	1.1	1.2	1.5	0.5	0.5	1	1	8	1	1
Fig. 6.5	1	1.1	1	1.5	0.5	0.5	1	1	8	1	1
Fig. 6.6	1	0.9	1	1.5	0.5	0.5	1	1	8	1	1
Fig. 6.7	1	1.1	1.2	1.5	0.5	0.5	1	1	8	1	1
Fig. 6.8	1	1.1	1	1.5	0.5	0.5	1	1	8	1	1
Fig. 6.9	1	0.9	1	1.5	0.5	0.5	1	1	9	1	1
Fig. 6.10	1	1	1	1.5	0.5	0.5	1	1	9	1	1
Fig. 6.11	1	1.1	1	1.5	0.5	0.5	1	1	9	1	1
Fig. 6.12	1	0.9	1	1.5	0.5	0.5	1	1	9	1	1
Fig. 6.14	1	0.9	1	1.5	0.5	0.5	1	1	60	1	1
Fig. 6.15	1	0.9	1	1.5	0.5	0.5	1	1	60	1	1
Fig. 6.16	1	0.9	1	1.5	0.5	0.5	1	1	60	1	1
Fig. 6.17	1	1.1	1.2	1.5	0.5	0.5	1	1	9	1	1
Fig. 6.18	1	0.9	1	1.5	0.5	0.5	1	1	9	1	1
Fig. 6.19	1	1	1	1.5	0.5	0.5	1	1	9	1	1
Fig. 6.20	1	1.1	1	1.5	0.5	0.5	1	1	9	1	1

$$\rho_1^*(\mathbf{r},0) = \begin{cases} 6+\gamma(\mathbf{r}) & x \le 12.8 \\ 0 & x > 12.8 \end{cases} \quad \text{and} \quad \rho_2^*(\mathbf{r},0) = \begin{cases} 0 & x \le 12.8 \\ 6+\gamma(\mathbf{r}) & x > 12.8 \end{cases} \tag{6.5.1}$$

where $\gamma(\mathbf{r})$ is a random variable with $\gamma(\mathbf{r}) \sim U(0,1)$, where U is a uniform distribution. For the results displayed in Fig. 6.3, we set $R_{11} = R_{22} = 1$ and the interaction range between cancer cells and healthy cells is $R_{12}/R_{11} = 0.9$ such that $R_{12} < \frac{1}{2}(R_{11} + R_{22})$. The top four plots in Fig. 6.3, are the density profile of the cancer cells minus the density of the healthy cells, at times (t= 0.1, 1.1, 6 and 15), it is clear that the total density of cancer cells increases with time and we can see

the peaks (i.e. cells) grow, then split and then move into the area occupied by the healthy cells. As a result, the healthy cells start to subsequently die. By the time $t = 6$, the region occupied by the cancer cells has significantly increased and the area occupied by the healthy cells has shrunk. Note the hexagonal pattern due to packing, which is retained as the size of the region occupied by cancer cells grows.

In the bottom of Fig. 6.3, we see that the average density of the cancer cells increases with time while the average density of the healthy cells decreases with time. However, this decrease is not monotonic; there are oscillations with three clear maxima. These oscillations correspond to the death of the healthy cells layer by layer and short periods of recovery to occupy the newly available space whilst simultaneously being replaced by the multiplying cancer cells. Finally, after $t \approx 7$ the density of the healthy cells decreases to zero monotonically.

In a second example displayed in Fig. 6.4 we set R_{11} =1 and increase the radii of the healthy cells to R_{22}/R_{11}=1.2, and also set R_{12}/R_{11}=1.1 such that $R_{12} = \frac{1}{2}(R_{11} + R_{22})$. All the rest of the parameters remain the same as in Fig. 6.3. In this example we see different behaviour for both types of cells. The cancer cells do not grow row by row as in the previous example in Fig 6.3. We see instead the formation of individual cancer cells ahead of the main front. We also observe some formation of cancer cells with the region still occupied by healthy cells, see for example the profile for t=9 in Fig. 6.4. Beyond t=13, the number of cancer cells remains constant. At the same time the number of healthy cells generally decreases over time. However, this decrease is once again not monotonic. For example, we see an increase in the average density at $t \approx 10$. Ultimately the average density of the healthy cells decreases and tends to zero (there remaining no healthy cells at all) as

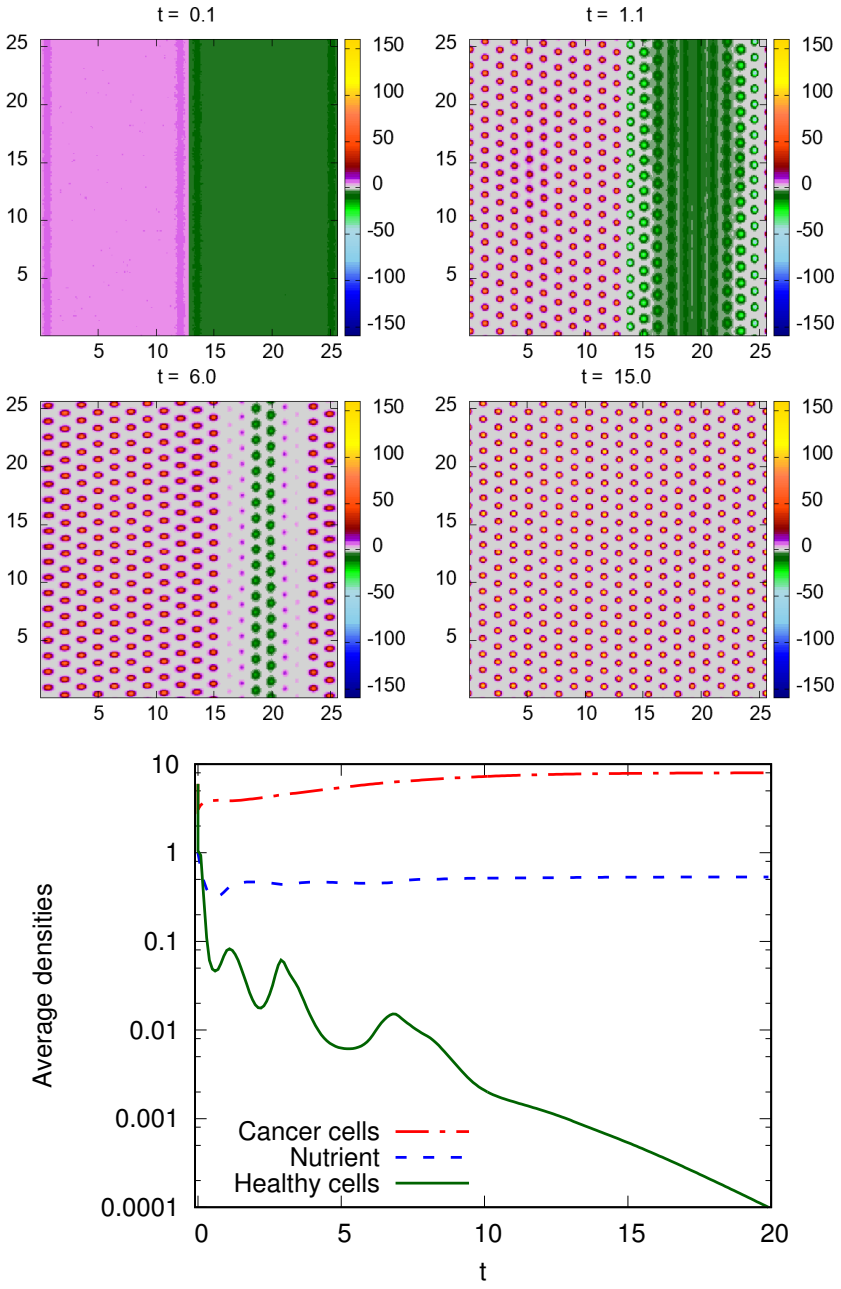

Figure 6.3: Top four panels: Plots of $\rho_1 - \rho_2$, the density profile of the cancer cells minus the density of the healthy cells, at times $t = 0.1, 1.1, 6$ and 15, when the initial conditions are defined in Eq. (6.5.1).The nutrient uptake rates $\tilde{\lambda}_{n1} = 1$ and $\tilde{\lambda}_{n2} = 1$, the population growth constants $c_1 = 0.5$ and $c_2 = 0.5$ and the threshold nutrient concentration for healthy cells $\alpha = 2$. The nutrient source is homogeneous with $f(\mathbf{r})$=1 and $\tilde{S}_n = 8$. The area of the domain is 25.6×25.6 and $\Delta x = \Delta y = 0.1$. The cell-cell pair interaction potential parameters are $\beta\varepsilon_{11} = 1$, $\beta\varepsilon_{12} = 1.5$, $\beta\varepsilon_{22} = 1$, $R_{11} = R_{22} = 1$ and $R_{21} = 0.9$. Bottom: the corresponding average cell density, [see Eq. (5.5.14)] and the average nutrient density [see Eq. (5.5.15)].

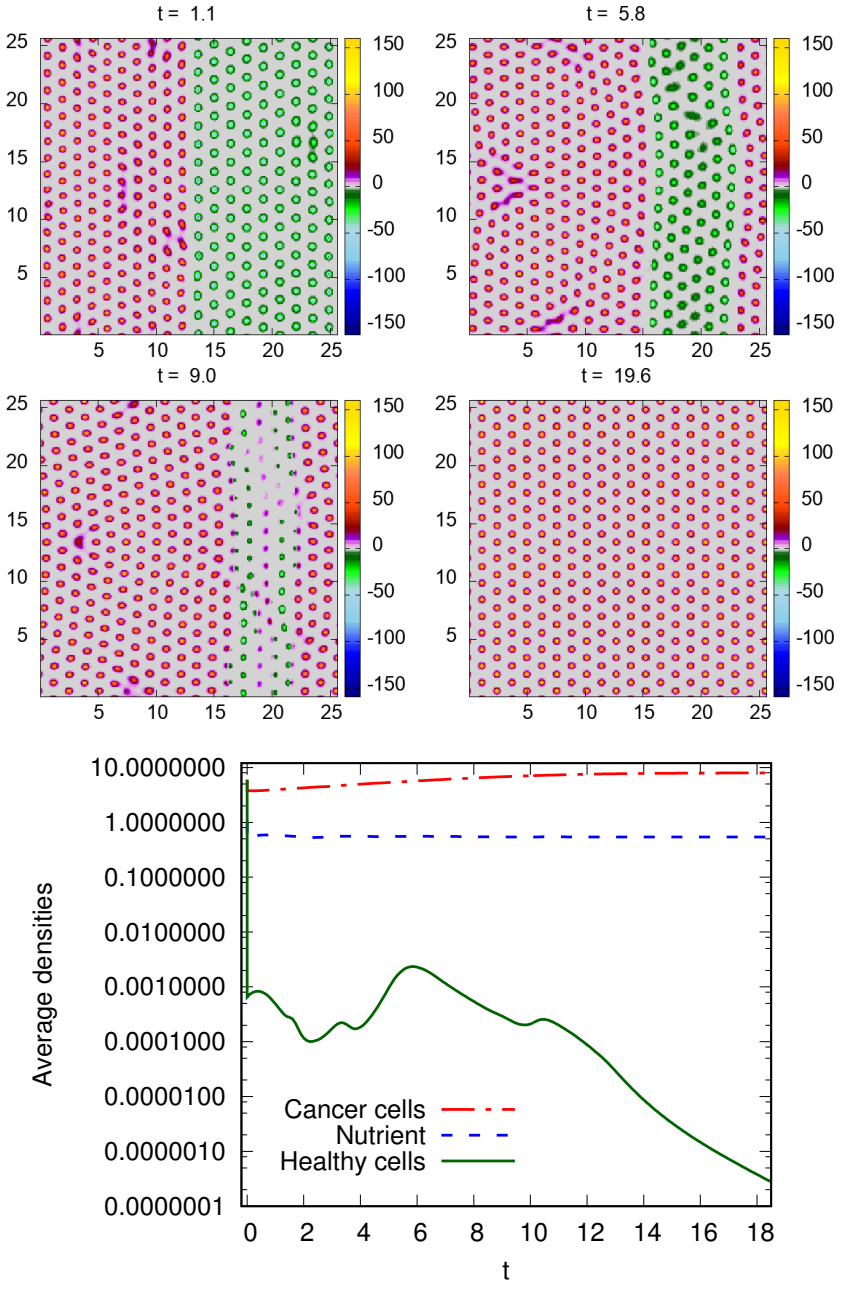

Figure 6.4: Snapshots of $(\rho_1 - \rho_2)$ at time $t = 1.1, 5.8, 9$ and 19.6. All the parameters here are the same as those in Fig. 6.3, except here the cross interaction pair potential radius is $R_{12} = 1.1$ and $R_{22} = 1.2$.

shown in the Fig. 6.4.

In a third example displayed in Fig. 6.5 we set $R_{11} = R_{22} = 1$, and also set R_{12}/R_{11}=1.1 such that $R_{12} > \frac{1}{2}(R_{11} + R_{22})$. All the rest of the parameters remain the same as in Fig. 6.3. In this example we see different a behaviour for both types of cells. The cancer cells penetrate in between the healthy cells, see for example the profile at t=5.8 in Fig. 6.5, we can see the new cancer cell layer that are being formed. This layer of cancer cell was formed in the middle of the healthy cells area, starts to form a coil-like shape as it seems that there is another melting state is taking place and at the same time the cancer cells continue to divide up and the number of healthy cells generally decrease over time. This decrease in this case is also not monotonic and the average densities for this case is similar to example 2 in Fig 6.4 more than example 1 in Fig. 6.3 because the average density of the healthy cells density has local maximum at $t \approx 4$, as shown in Fig. 6.5.

6.5.1.2 Diagonal domain case

In Fig. 6.6 we present results for the same system as in Fig. 6.3, except we change the initial conditions to

$$\rho_1^*(\mathbf{r},0) = \begin{cases} 6+\gamma(\mathbf{r}) & x \le y \\ 0 & x > y \end{cases} \quad \text{and} \quad \rho_2^*(\mathbf{r},0) = \begin{cases} 0 & x \le y \\ 6+\gamma(\mathbf{r}) & x > y \end{cases} \tag{6.5.2}$$

where $\gamma(\mathbf{r})$ is a random variable as before. This corresponds to two triangular domains, with periodic boundary conditions. Given the hexagonal crystal like ordering of the density peaks, this allows us to locate the interface between the two cell types

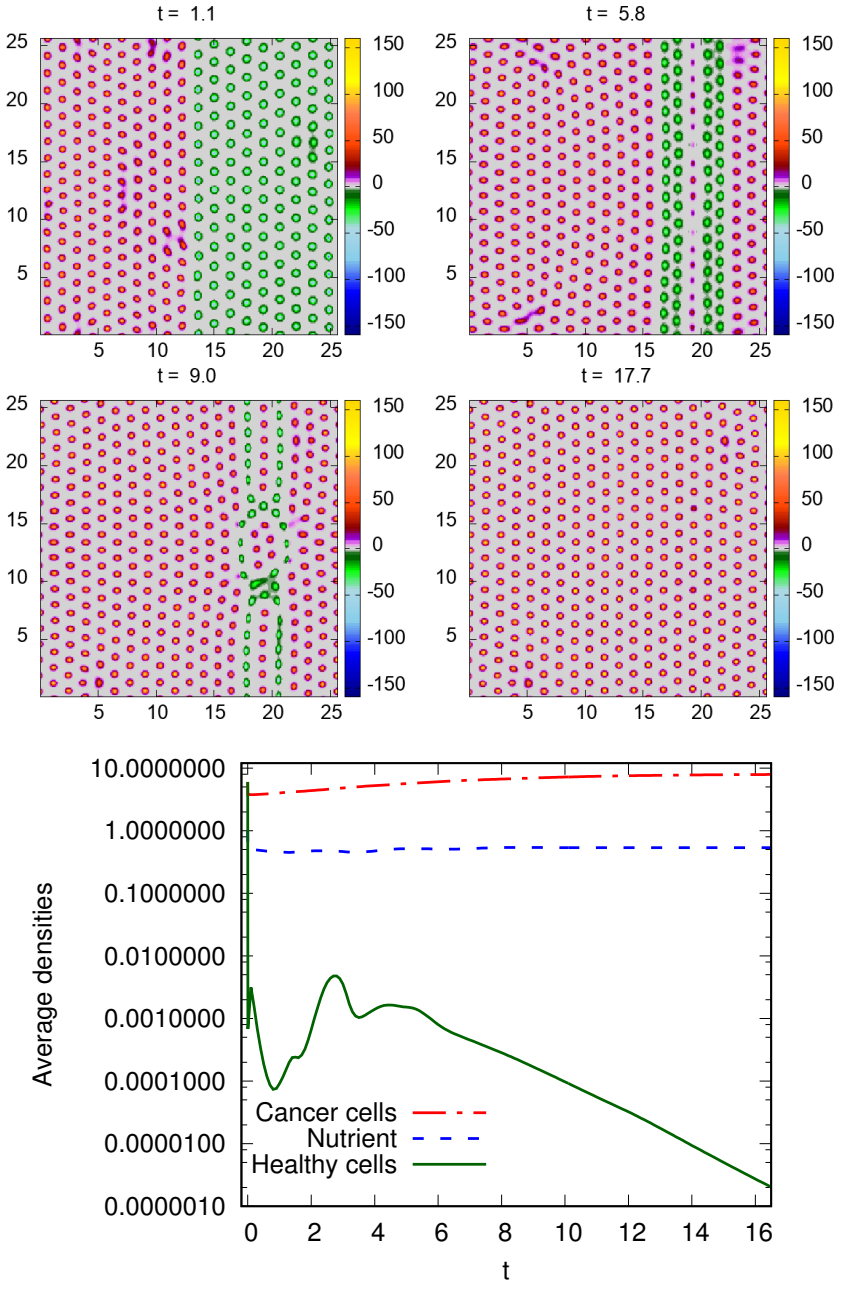

Figure 6.5: Snapshots of $(\rho_1 - \rho_2)$ at the times $t = 1.1, 5.8, 9$ and 17.7. All the parameters here are the same as those in Fig. 6.3, except here the cross interaction pair potential radius is $R_{12} = 1.1$.

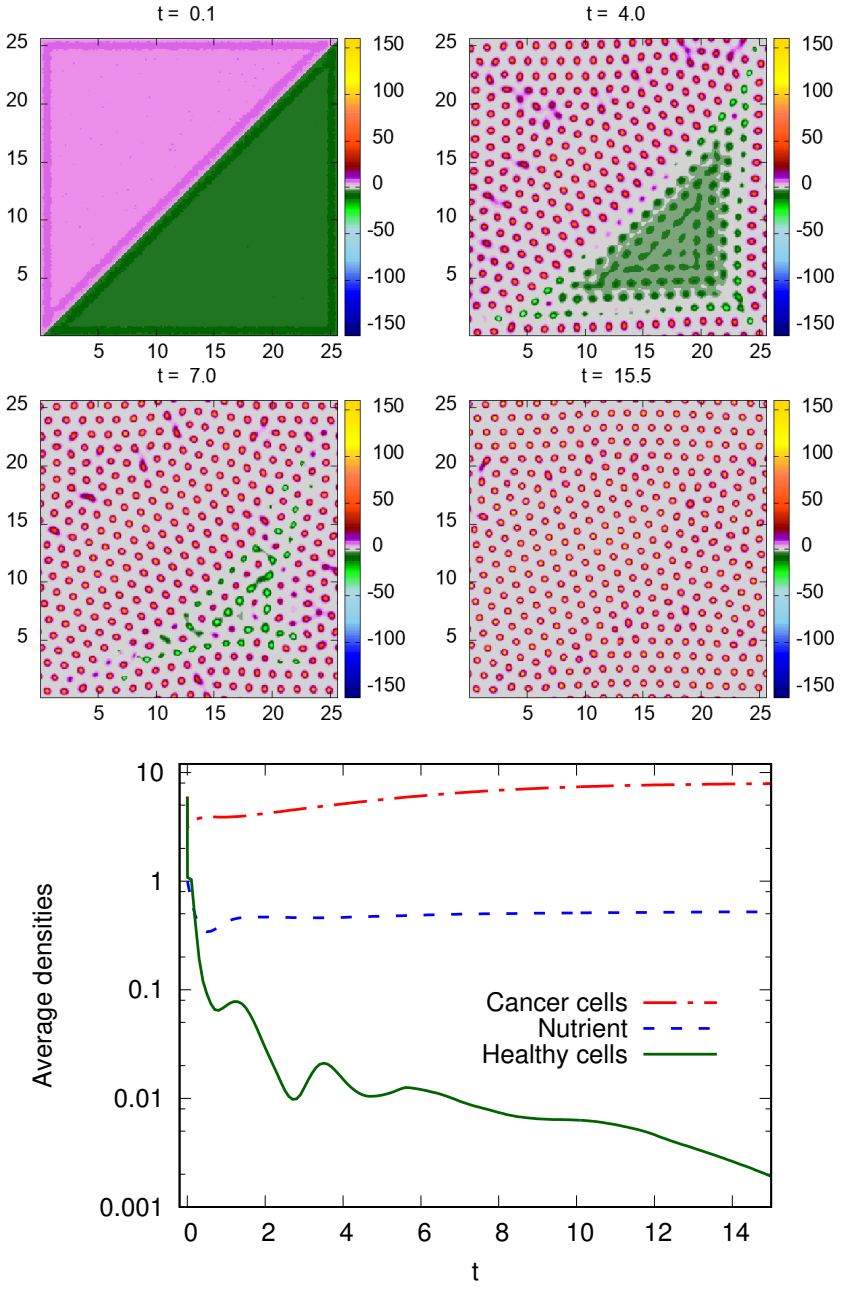

Figure 6.6: Top four panels: Plots of $\rho_1 - \rho_2$, the density profile of the cancer cells minus the density of the healthy cells, at times $t = 0.1, 4, 7$ and 15.5, All the parameters here are the same as those in Fig. 6.3, except here the initial conditions are defined in Eq. (6.5.2).

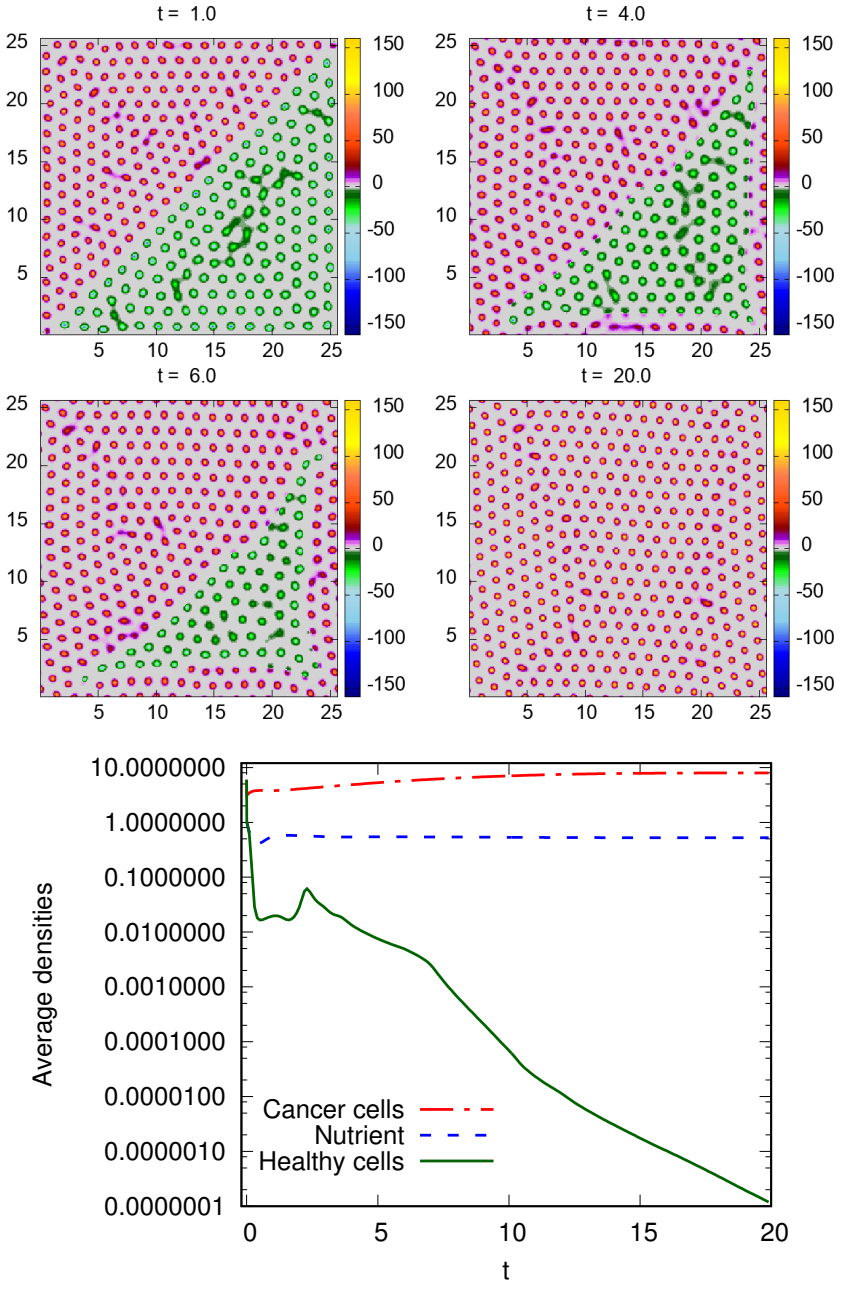

Figure 6.7: Snapshots of $(\rho_1 - \rho_2)$ at the times $t = 1, 4, 6$ and 20. All the parameters here are the same as those in Fig. 6.6, except here the cross interaction pair potential radius is $R_{12} = 1.1$ and $R_{22} = 1.2$.

at a different orientation to the lattice plane.

In Fig. 6.6, we set $R_{11} = R_{22} = 1$ and the interaction range between cancer cells and healthy cells is $R_{12}/R_{11} = 0.9$ such that $R_{12} < \frac{1}{2}(R_{11} + R_{22})$, the four plots in the top are are the density profile of the cancer cells minus the density of the healthy cells at a series of different times (t= 1, 4, 7 and 15.5). In bottom of Fig. 6.6 we display the corresponding plots of the average densities over time. Comparing with Figs. 6.3, we see that the results have some similarities, but there are also significant differences. In particular the average density of the healthy cells has less prominent oscillations. Recall that these oscillations correspond to the death of the healthy cells layer by layer.

In Fig. 6.7 we present results using the same parameters as in Fig. 6.4, except we change to the diagonal initial conditions in Eq. (6.5.2). The results in top of the Fig. 6.7 show density profiles for a series of different times t =1, 4, 6 and 20 . The corresponding average densities over time are shown in bottom of the Fig. 6.7. The total density of the cancer cells increases with the time whilst the total density of the healthy cells decreases. However, the decrease is not monotonic, as can be seen Fig. 6.7 which exhibits a single peak at $t \approx 10.7$.

In Fig. 6.8 we present results for system same as in Fig. 6.5, except we change to the diagonal initial conditions in Eq. (6.5.2). The results in the top of the Fig. 6.8 show density profiles for a series of different times t =1.1, 4.6, 6.0 and 12.8. The corresponding average densities over time are shown in bottom of the Fig. 6.8. The total density of the cancer cells increases with the time whilst the total density of the healthy cells decreases, although the decrease in Fig. 6.8 is not monotonic and similar to the example in Fig 6.6 rather than example in Fig. 6.7. The interesting aspect that we observe in Fig. 6.8 when comparing with Fig. 6.5 is the degree to

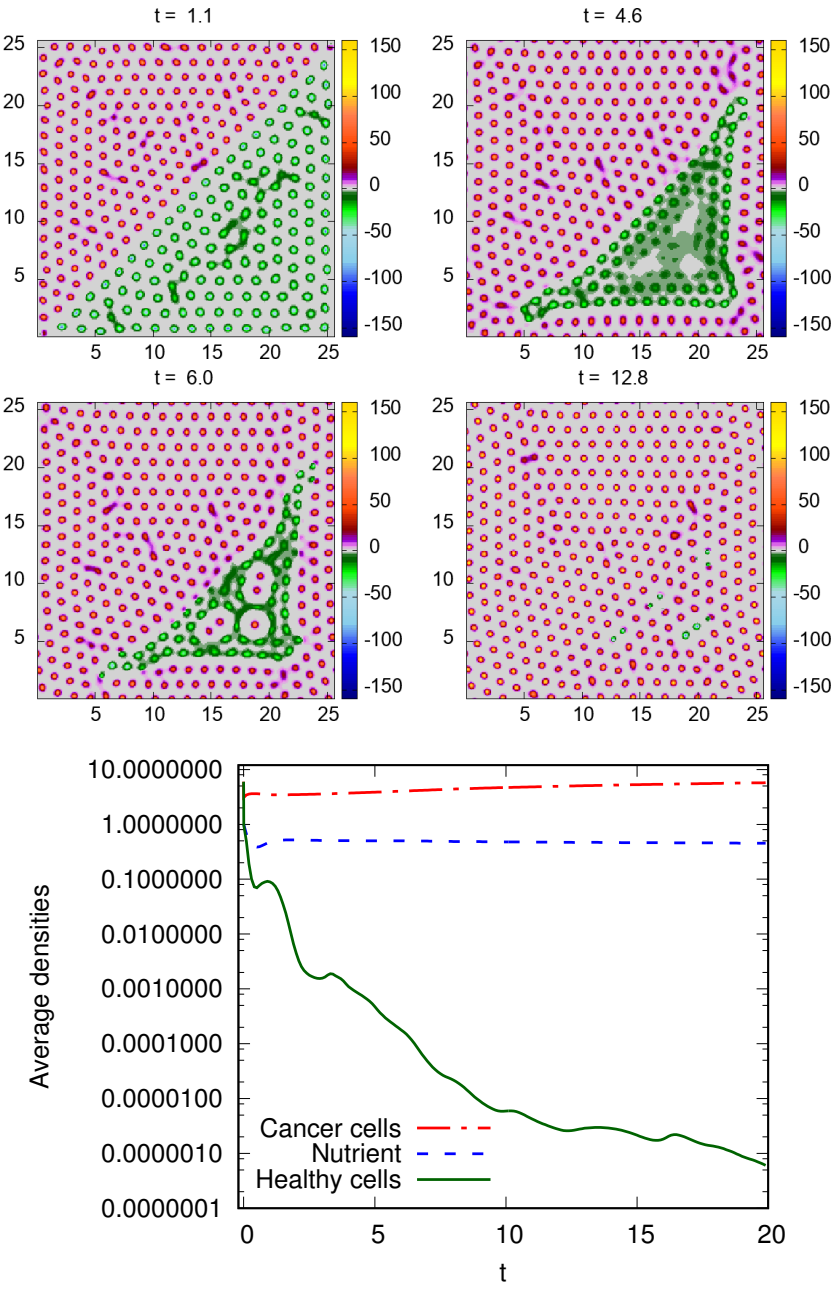

Figure 6.8: Snapshots of $(\rho_1 - \rho_2)$ at the times $t = 1.1, 4.6, 6$ and 12.8. All the parameters here are the same as those in Fig. 6.6, except here the cross interaction pair potential radius is $R_{12} = 1.1$.

which the cancer cells penetrate into the healthy tissue, forming in the midst of region of healthy cells.

6.5.1.3 Initial small circular cancer case

The figures 6.9–6.11 we display results for the evolution over time starting from the initial condition

$$\rho_1(\mathbf{r},0) = \begin{cases} 6+\gamma(\mathbf{r}) & (x-12.8)^2+(y-12.8)^2 \leq 6^2 \\ 0 & (x-12.8)^2+(y-12.8)^2 > 6^2, \end{cases} \tag{6.5.3}$$

$$\rho_2(\mathbf{r},0) = \begin{cases} 0 & (x-12.8)^2+(y-12.8)^2 \leq 6^2 \\ 6+\gamma(\mathbf{r}) & (x-12.8)^2+(y-12.8)^2 > 6^2 \end{cases} \tag{6.5.4}$$

where $\gamma(\mathbf{r})$ is a random variable drawn from a uniform distribution on the interval $(0,1)$ and $n(\mathbf{r},0) = 0.5$. This initial condition corresponds to a small circular cancer of radius 6 in the middle of healthy cells. Figs 6.9–6.11 show simulations with $R_{12} = 0.9, 1, 1.1$, respectively, with all other parameters fixed as in Fig. 6.3, noting that $R_{11} = R_{22} = 1$. In the case of R_{12} =0.9, the two cell types can tolerate being closer to each other thereby promoting mixing behaviour; this despite the repulsive strength across types, $\beta\varepsilon_{12} = 1.5$, being stronger than that between them $\beta\varepsilon_{11} = \beta\varepsilon_{22}$= 1. For R_{12}= 1.1 we expect more demixing type behaviour.

We see in Fig. 6.9 that although within the domains where the different cell species are initiated – see Eqs. (6.5.3) and (6.5.4) – the densities are uniform, i.e. liquid–like, rather than a "crystalline" state with density peaks, the peaks corresponding to the locations of the cells rapidly form and are already present by the

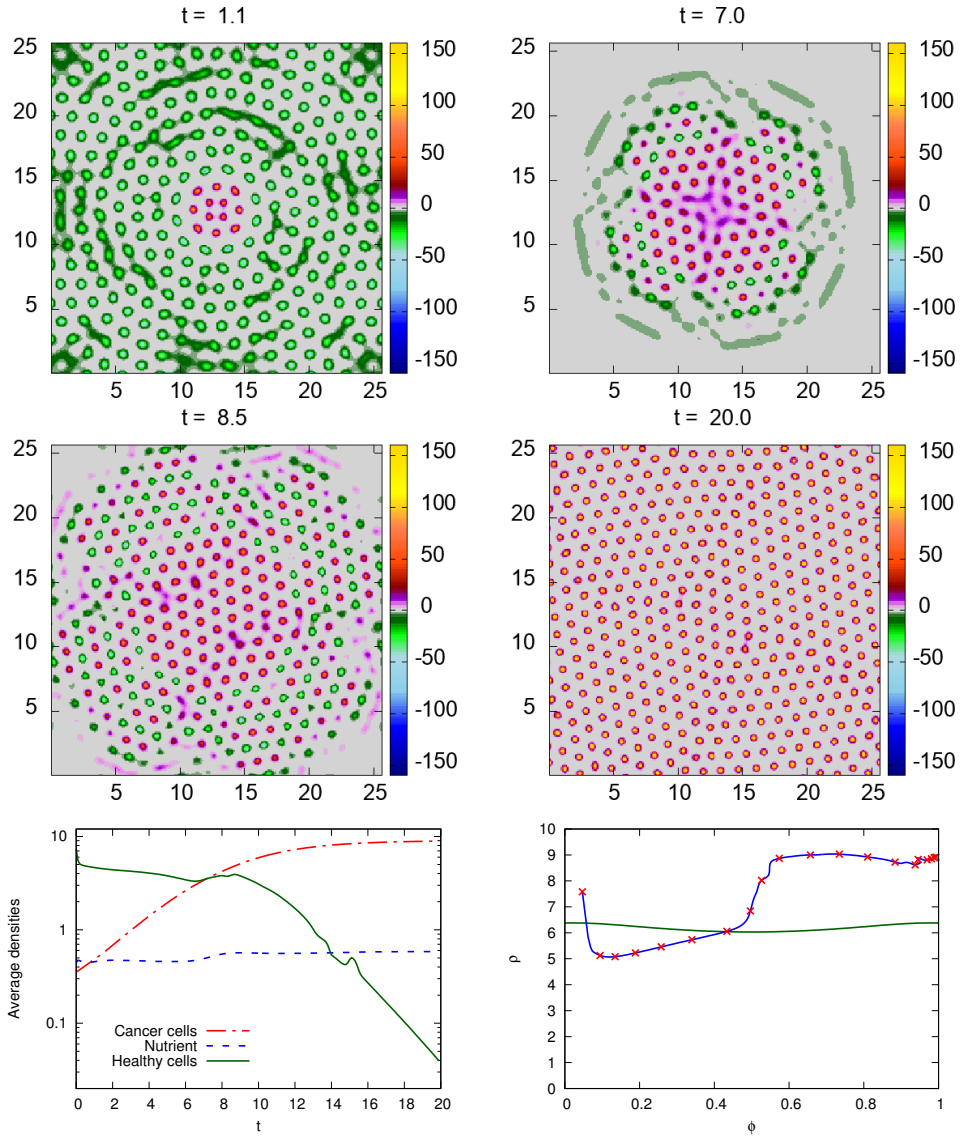

Figure 6.9: Top four panels: Snapshots of $(\rho_1 - \rho_2)$, the density profile of the cancer cells minus that of the healthy cells, at the times $t = 1.1$, 7, 8.5 and 20 evolving from the initial conditions defined in Eqs. (6.5.3) and (6.5.4). The system parameters are $\tilde{\lambda}_{n1} = \tilde{\lambda}_{n2} = 1$, $\tilde{D}_c = \tilde{D}_h = 1$, $c_1 = c_2 = 0.5$ and $\alpha = 2$. The nutrient source is homogeneous with $f(\mathbf{r}) = 1$ and $\tilde{S}_n = 9$. The area of the domain is 25.6×25.6 and $\Delta x = \Delta y = 0.1$. The parameters in the pair interaction potentials between the cells are $\beta\varepsilon_{11} = 1$, $\beta\varepsilon_{12} = 1.5$, $\beta\varepsilon_{11} = 1$, $R_{11} = R_{22} = 1$ and $R_{12} = 0.9$. In the bottom left panel are plotted the corresponding average cell densities [see Eq. (5.5.14)] and the average nutrient density [see Eq. (5.5.15)]. In the bottom right panel we plot the trajectory of the time evolution in the (ρ, ϕ) plane. Note that the red cross points from left to right on this trajectory correspond to the integer times $t = 1, 2, \ldots$. We also plot the linear stability threshold for this system. When the trajectory dips below this line, the system temporarily "melts".

time $t = 1.1$. However, this sudden initial growth leads to a drop in the nutrient level, as can be seen at $t \approx 6$ in the bottom left panel of Fig. 6.9. The drop in nutrient level then leads to a drop in the overall number of healthy cells, which leads to the "crystal" melting temporarily, which corresponds to the cells being distributed in disordered liquid-like configurations; biologically, this melting phenomena can be viewed as a temporary state of flux, whereby cells are moving around relatively rapidly and the densities shown are the average density distribution of the cell centres. The nutrient level then recovers and the system "refreezes" and over time the cancer cells penetrate the healthy tissue and eventually the healthy cells all die out. The temporary "melting" can be understood if one plots the trajectory of the system in the total density versus concentration (ρ, ϕ) plane, in addition to plotting the threshold for the system to be linearly unstable, given by Eq. (6.4.14). This is displayed in the bottom right panel of Fig. 6.9. Recall that above the stability line the system is linearly unstable and forms peaks. We see that when the trajectory dips below this line is when the system temporarily "melts".

In the Fig. 6.10 we plot results for the case when all the model parameters are the same as those in the previous case (that displayed in Fig. 6.9), except now the radius in the cross interaction pair potential $R_{12} = 1$, which is slightly larger (for the results in Fig. 6.9 we have $R_{12} = 0.9$). In Fig. 6.10 we plot $(\rho_1 - \rho_2)$ at the times t=1.1, 6.5, 8.5 and 20. As before, we see that the total density of the cancer cells increases with time and the healthy cells retreat from the centre. Finally all the healthy cells die by $t = 20$. The consequence of the increased value of R_{12} is that there is now a tendency for the cancer cells to penetrate into layers beyond the initial interfacial layer of healthy cells, and so form alternating layers of healthy and cancerous cells – see e.g. the plot for the time $t = 6.5$. The averages densities

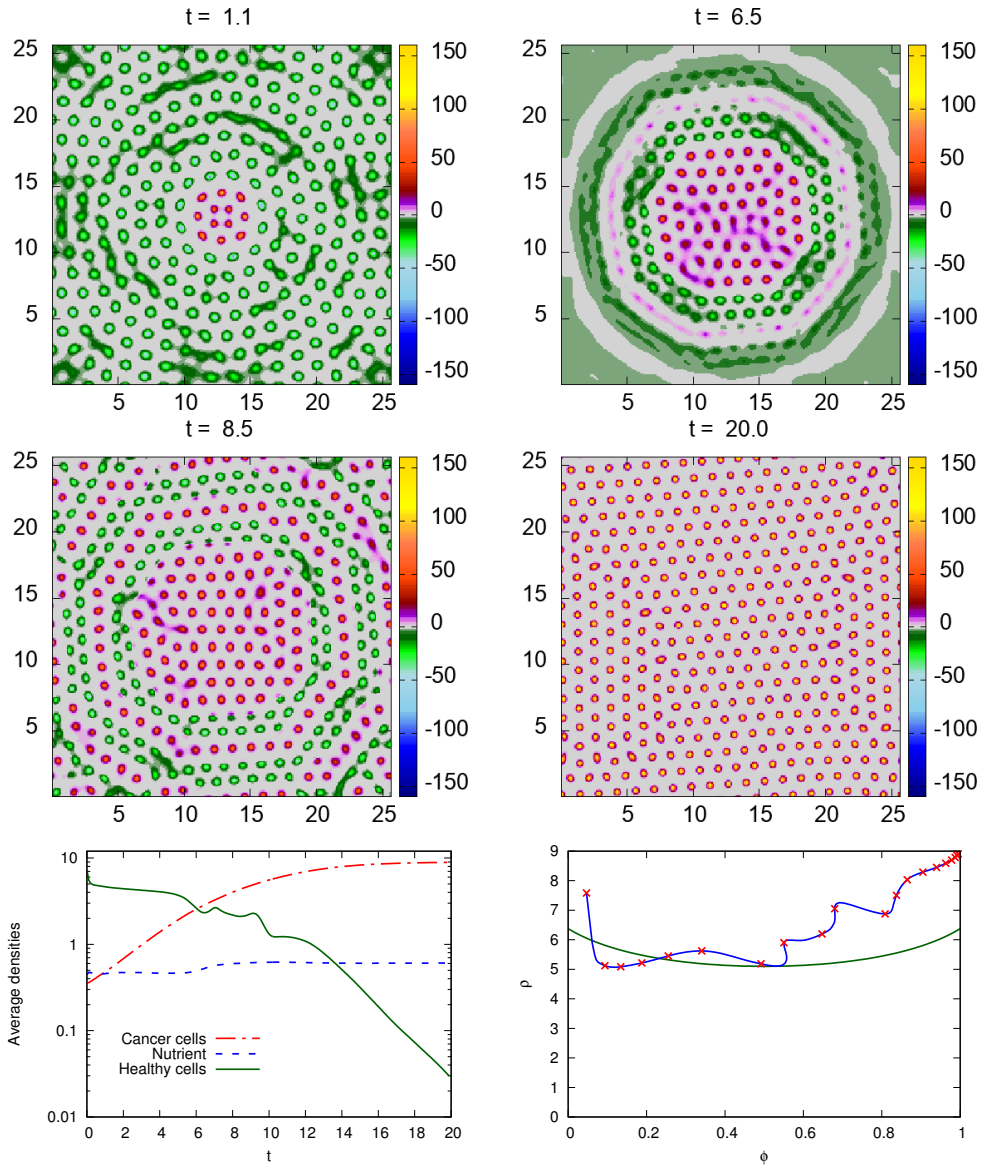

Figure 6.10: Snapshots of $(\rho_1 - \rho_2)$ at the times $t = 1.1$, 6.5, 8.5 and 20. All the parameters here are the same as those in Fig. 6.9, except here the cross interaction pair potential radius is $R_{12} = 1$, which is slightly larger.

over time are shown in the bottom left panel of Fig. 6.10 and in the bottom right end is the trajectory in the (ρ, ϕ) plane and also the corresponding linear stability threshold line.

In Fig. 6.11 we present results for an even larger value of the cross interaction radius, $R_{12} = 1.1$. Comparing with Figs. 6.9 and 6.10, we see that the effect of this increase is to further increase the tendency of the cancer cells to penetrate into the healthy tissue (metastasis) and in this case forming roughly circular clumps of cancer cells ahead of the main tumour, rather than layers.

The dynamics shown in each of Figs. 6.9 and 6.10 reflects metastasis. Smaller cross species interaction range, R_{12}, lead to a disordered infiltration of healthy tissue by individual tumour cells, which is more ordered for $R_{12} = 1$. For the larger R_{12}, tumour cells appears to infiltrate healthy tissue as small clusters. In each case, much of the initial mixing of cell types occurs during the transient melting phase, the timescale for which decreases on increasing R_{12} (as can be seen from the linear stability threshold diagrams); we note, however, the central core structure of tumour regions is maintained during the melting phase. The different manner of infiltration is an interesting consequence of the modelling assumptions, but it would be experimentally challenging to discern which of these patterns, if any, are relevant biologically.

To avoid the system exhibiting the temporary "melting" phenomenon, we increase the radius in the initial conditions (6.5.3) and (6.5.4). We adjusted the radius of the initially cancerous area such that the size of this region becomes equal to the size of the healthy area. In Fig 6.12, we plot $(\rho_1 - \rho_2)$ for three cases, the first column demonstrate the case when $R_{12} = 0.9$ $\left[R_{12} < \frac{1}{2}(R_{11} + R_{22})\right]$ at times $t = 1, 5, 8$ and 15, The second one represent the case when $R_{12} = 1$ $\left[R_{12} = \frac{1}{2}(R_{11} + R_{22})\right]$ at times

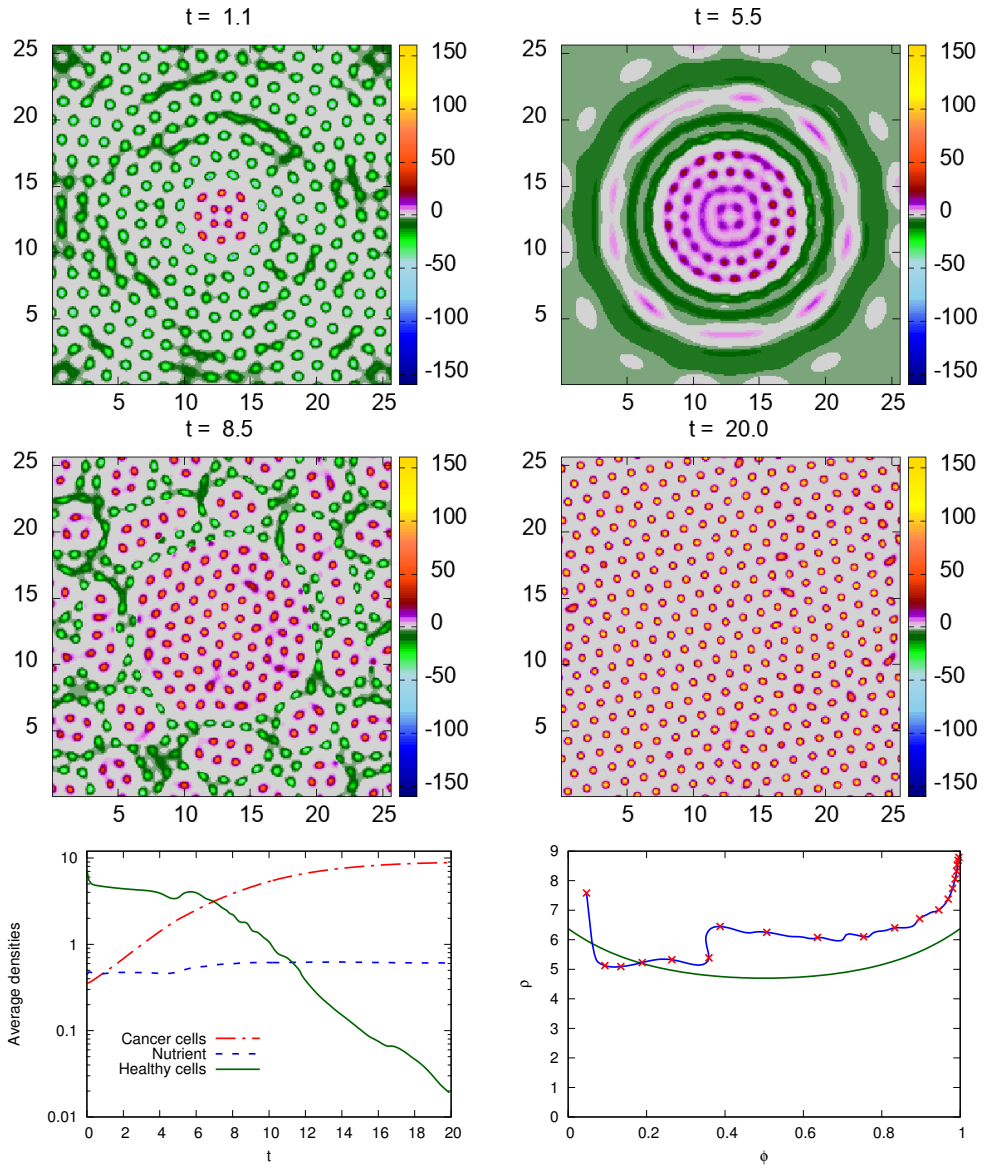

Figure 6.11: Snapshots of $(\rho_1 - \rho_2)$ at the times $t = 1.1$, 5.5, 8.5 and 20. All the parameters here are the same as those in Figs. 6.9 and 6.10, except here the cross interaction pair potential radius is even larger, $R_{12} = 1.1$.

$t = 1, 7.5, 9.5$ and 16. The last column illustrates the situation when $R_{12} = 1.1$ $\left[R_{12} > \frac{1}{2}(R_{11} + R_{22})\right]$ at times $t = 1, 5.5, 8$ and 19. From the figure, we can see the time at which a new row of cancer cells penetrates with the healthy tissue is at times t=5.0, 7.5 and 5.5, respectively. The transition stage (between penetration and the final steady state) is similar in all cases. However, for $R_{12} < \frac{1}{2}(R_{11} + R_{22})$, the healthy area is the largest compared to the other two. The time at which the system forms the final steady state for all the three cases is $t \approx 15$, 16 and 19 respectively. Although the averages densities over time of the cancer cells and nutrient are similar for all cases, the average density over time of the healthy cells is somewhat different, as shown in Fig. 6.13.

6.5.2 Results with inhomogeneous nutrient sources

In this section we discuss some results showing the competition between healthy and cancer cells, obtained by solving numerically the system Eqs. (6.2.3), (6.2.7) and (6.2.11), using a nutrient source located along the vertical mid–line of the system, see Eq. (4.4.5). These results are for the population growth constants $c_1 = c_2 = 0.5$ and the threshold nutrient concentration for healthy cells $\alpha = 2$. We fix the various cell-cell interaction parameters to be $\beta\varepsilon_{11} = \beta\varepsilon_{22} = 1$, $\beta\varepsilon_{12} = 1.5$ (so that density peaks of the two different cell types do not overlap), $R_{11} = R_{22} = 1$ and $R_{12} = 0.9$. The nutrient uptake rate for cancer cells $\tilde{\lambda}_{n1} = 1$ and for healthy cells $\tilde{\lambda}_{n2} = 1$. The area of the domain in which the model is solved is 25.6×25.6 and $\Delta x = \Delta y = 0.1$. The nutrient source is non uniform, with $f(\mathbf{r}) = e^{(-(x-L/2)^2)}$ and $\tilde{S}_n = 60$. The diffusion coefficients for both cell species are equal, $\tilde{D}_c = \tilde{D}_h = 1$.

Notice that the value of $\tilde{S}_n$ with inhomogeneous nutrient is greater than the value

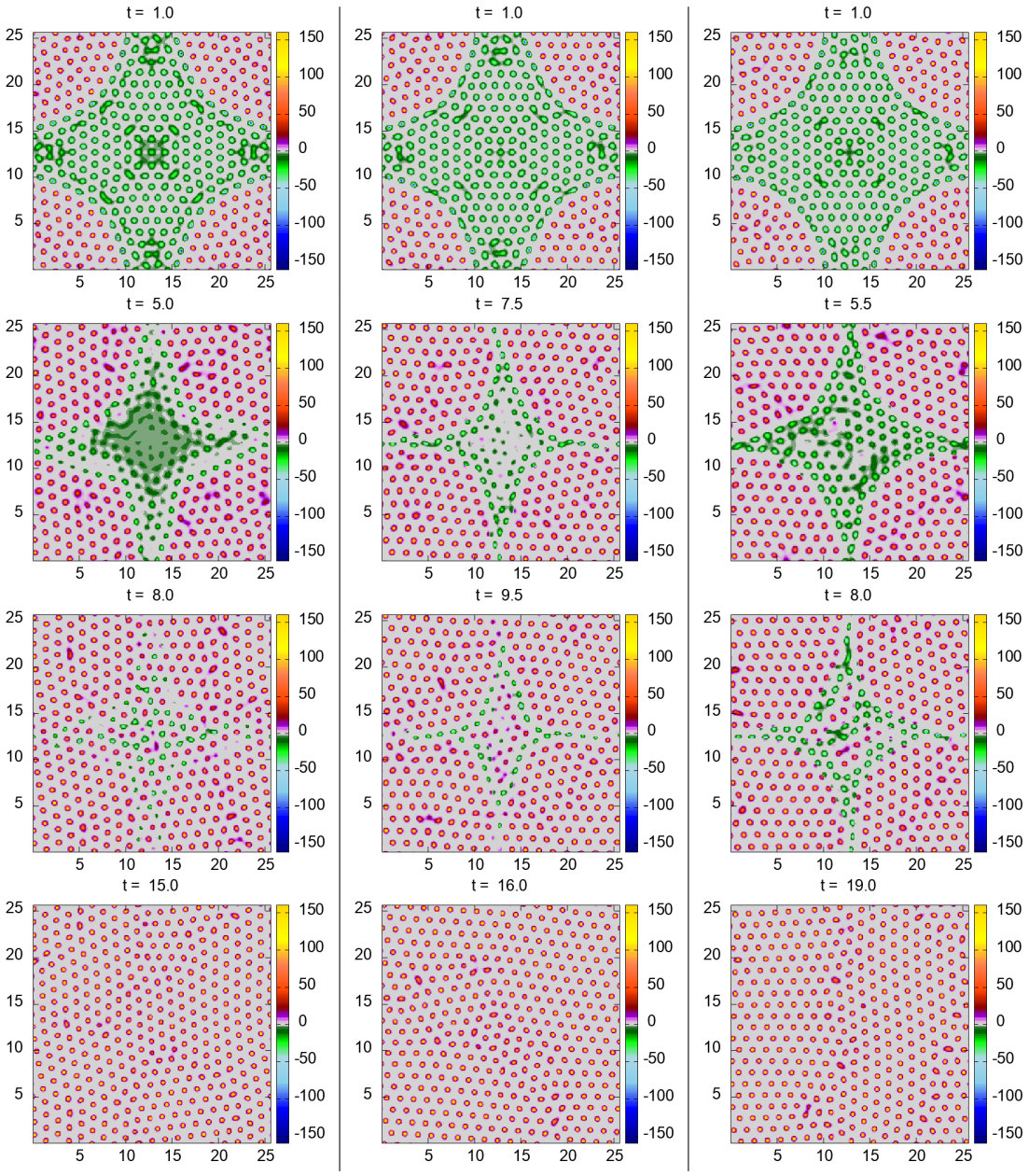

Figure 6.12: Density profile of $(\rho_1 - \rho_2)$ when $R_{12} < \frac{1}{2}(R_{11} + R_{22})$ at times $t = 1, 5, 8$ and 15 (left), $(\rho_1 - \rho_2)$ when $R_{12} = \frac{1}{2}(R_{11} + R_{22})$ at times $t = 1, 7.5, 9.5$ and 16 (middle) and $(\rho_1 - \rho_2)$ when $R_{12} > \frac{1}{2}(R_{11} + R_{22})$ at times $t = 1, 5.5, 8$ and 19 when the initial conditions are defined in Eqs. (6.5.3) and (6.5.4). The system parameters are $\tilde{\lambda}_{n1} = \tilde{\lambda}_{n2} = 1$, $\tilde{D}_c = \tilde{D}_h = 1$, $c_1 = c_2 = 0.5$ and $\alpha = 2$. The nutrient source is homogeneous with $f(\mathbf{r}) = 1$ and $\tilde{S}_n = 9$. The area of the domain is 25.6×25.6 and $\Delta x = \Delta y = 0.1$. The pair potential between cells are $\beta\varepsilon_{11} = 1$, $\beta\varepsilon_{12} = 1.5$ and $\beta\varepsilon_{11} = 1$, $R_{11} = R_{22} = 1$.

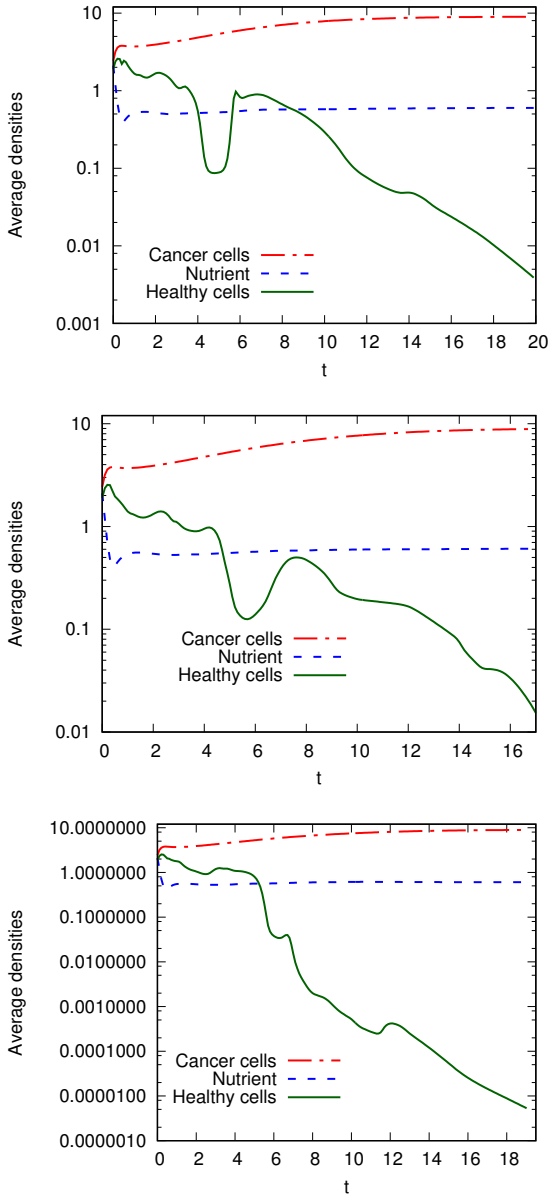

Figure 6.13: The average cell density, [see Eq.(5.5.14)] and the average nutrient density [see Eq.(5.5.15)], corresponding to the results in Fig. 6.12. When $R_{12}<\frac{1}{2}(R_{11}+R_{22})$ (above), $R_{12}=\frac{1}{2}(R_{11}+R_{22})$ (middle) and when $R_{12}>\frac{1}{2}(R_{11}+R_{22})$ (bottom).

of $\tilde{S}_n$ used with homogeneous nutrient which is described in Sec. 6.5.1 because we want the total flux of nutrient into the system to be the same in all cases i.e. we choose S_n so that the quantity $S_n \int_\Omega f(\mathbf{r})d\mathbf{r}$ is the same in all cases. Note that in particular for the two cases we consider here

$$\int_\Omega f(\mathbf{r})d\mathbf{r} = \begin{cases} L^2, & f(\mathbf{r}) = 1 \\ L^{3/2}\sqrt{\frac{\pi}{2}}, & f(\mathbf{r}) = e^{(-(x-L/2)^2)}, \end{cases} \tag{6.5.5}$$

which leads to $S_{n_2} = S_{n_1} L^{1/2}\sqrt{\frac{2}{\pi}}$ where L is the domain width.

In contrast to the results in previous sections, which gave similar behaviour when we used different initial conditions, the time evolution profile of the cells (healthy or cancer) is shown to be different depending on the initial conditions.

In our first example, we use the initial conditions given in Eqs. (6.5.3) and (6.5.4) [see Fig. 6.14]. The cancer cells are located in a circular area at the four corners of the domain (recall the system has periodic boundary conditions) and the remaining space is occupied by healthy cells. Since the nutrients are only in the mid vertical line of the area, the (mostly healthy) cells that are in the middle are provided with the nutrients needed to grow and reproduce whereas all cells on left and right edges, have no nutrients resulting in the death of these cells, over the period t = 2–3. At t=3, a few surviving cancer cells start to appear in the middle, surrounded by healthy cells. This is due to a low level of penetration of cancer cells in this region. In time, these cancer cells divide and grow, emerging at various parts along the region where there is a good source of nutrients. As both the cancer and healthy cells are splitting and increasing in number, the new cells formed push the cells around then forcing them to the side where, as a result of a lack of nutrients, they die. As time

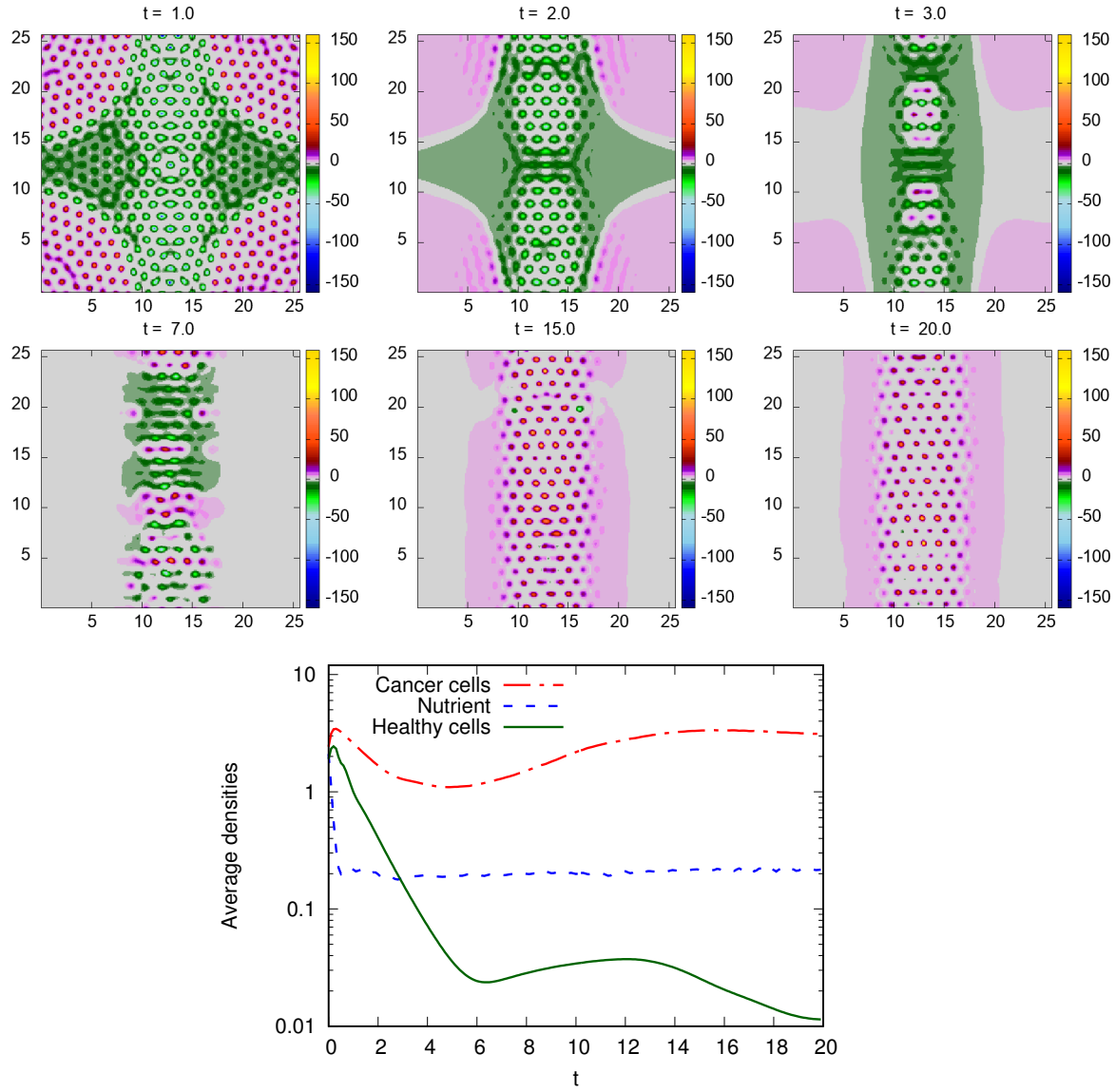

Figure 6.14: Top six panels: Plots of $\rho_1 - \rho_2$, the density profile of the cancer cells minus the density of the healthy cells, at times $t = 1, 2, 3, 7, 15$ and 20, where the initial conditions are defined in Eq. (6.5.3). The nutrient uptake rates $\tilde{\lambda}_{n1} = 1$ and $\tilde{\lambda}_{n2} = 1$, the population growth constants $c_1 = 0.5$ and $c_2 = 0.5$ and the threshold nutrient concentration for healthy cells $\alpha = 2$. The nutrient source $f(\mathbf{r})$ is centred at 12.8 as given by Eq.(4.4.5) with $\tilde{S}_n = 60$. The area of the domain is 25.6×25.6 and $\Delta x = \Delta y = 0.1$. The cell-cell pair interaction potential parameters are $\beta\varepsilon_{11} = 1$, $\beta\varepsilon_{12} = 1.5$, $\beta\varepsilon_{22} = 1$, $R_{11} = R_{22} = 1$ and $R_{21} = 0.9$. Bottom: the corresponding average cell density, [see Eq. (5.5.14)] and the average nutrient density [see Eq. (5.5.15)].

progresses, the cancer cells displace the healthy cells. This is almost completed by t = 15, and finally, at t=20 all healthy cells are dead and the area is filled with cancer cells which carry on dividing and producing new cancer cells. The averages densities of the cancer cells, the nutrient and the healthy cells is shown in the bottom of Fig. 6.14.

As a second example we use the initial conditions given in Eqs. (6.5.2) [see Fig. 6.15]. As before, cells of both types die out at the edges of the domain due to lack of nutrient. However, in this case there is already a substantial population of cancer cells on the centre line. This leads to a relatively rapid collapse of the healthy cell population as the cancer cells invade this space. Healthy cells have vanished by t=10. The averages densities for cancer cells, nutrient and healthy cells is shown in the bottom end of Fig. 6.15, showing clearly the rapid decline of healthy cells in comparison to that shown in Fig. 6.14.

In the third example we use the initial conditions given in Eqs. (6.5.1) [see Fig. 6.16]. Three important points in this model are different from the other two examples. The first point is that there is no penetration of the cancer cells into the healthy region. The second point is that the healthy cells die due to lack of nutrient rather than cancer cell invasion. The final crucial point in this example is that the system reaches the steady state very quickly compared with the other two examples, such that by t=5, all the healthy cells have died out, as seen in Fig. 6.16. The averages densities for cancer cells, nutrient and healthy cells is shown in bottom of Fig. 6.16.

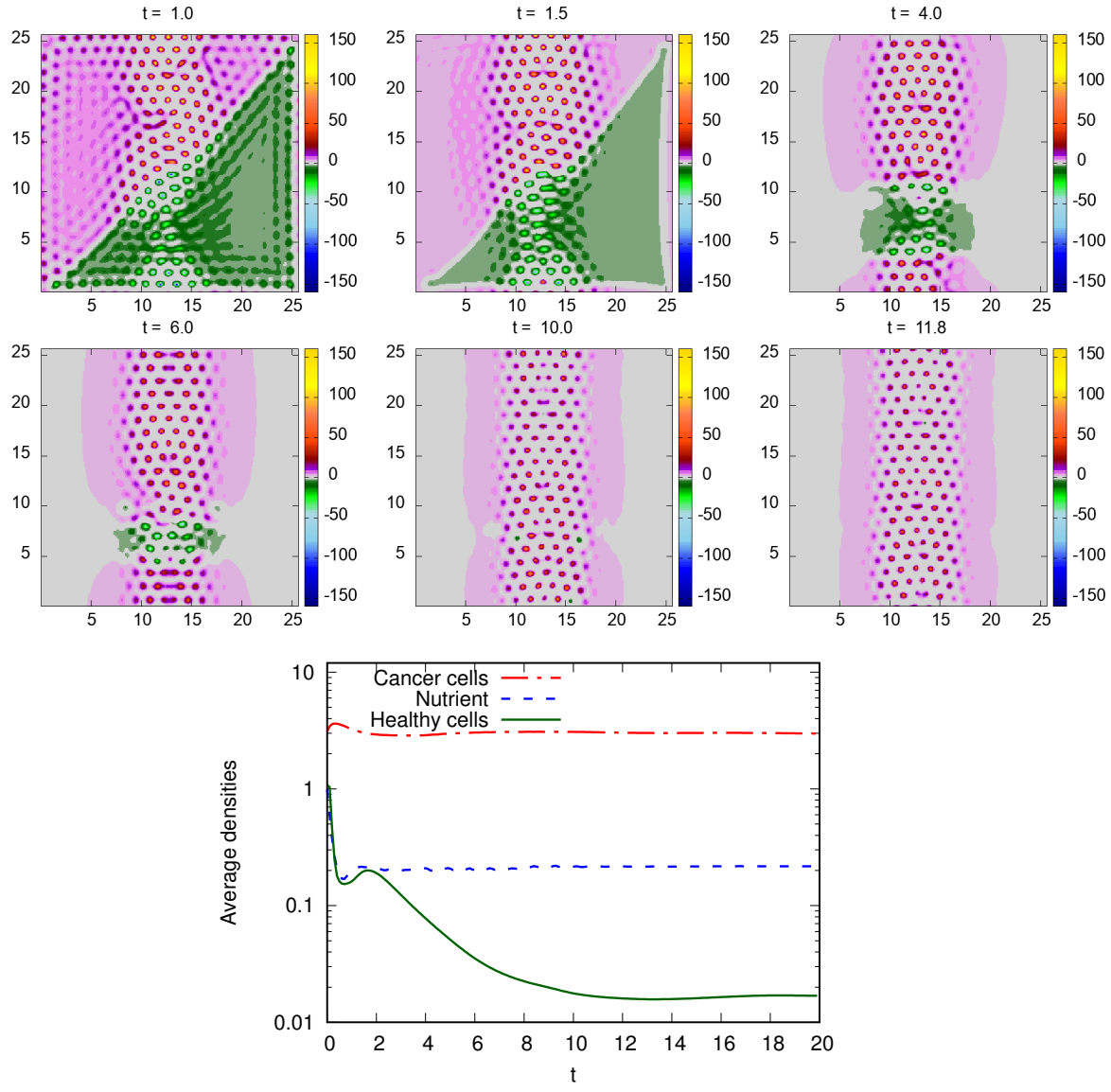

Figure 6.15: Top six panels: Plots of $\rho_1 - \rho_2$, the density profile of the cancer cells minus the density of the healthy cells, at times $t = 1, 1.5, 4, 6, 10$ and 11.8. All the parameters here are the same as those in Fig. 6.14, except here the initial conditions are defined in Eq. (6.5.2)

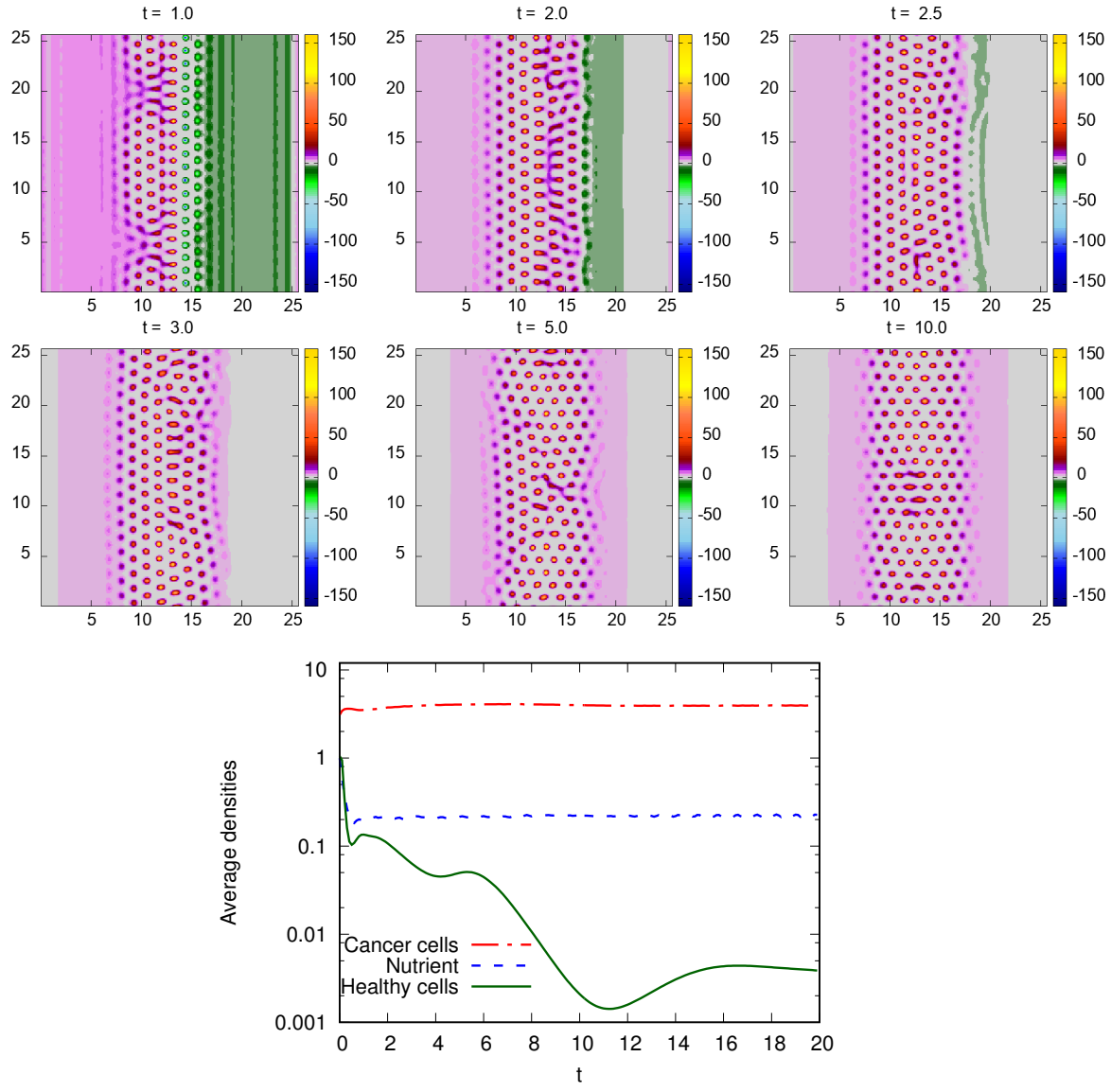

Figure 6.16: Top six panels: Plots of $\rho_1 - \rho_2$, the density profile of the cancer cells minus the density of the healthy cells, at times $t = 1, 2, 2.5, 3, 5$ and 10. All the parameters here are the same as those in Fig. 6.14, except here the initial conditions are defined in Eq. (6.5.1)

6.5.3 A few cancer cells dispersed throughout healthy tissue

In order to model the growth and spread of a tumour within healthy tissue we consider a case where we first initiate the system with one half containing predominantly healthy tissue, the other half containing cancerous tissue (with uniform densities in each half) and a uniform nutrient density. As the system evolves, peaks form in the two cell density profiles and over time the cancer cells displace the healthy cells until the total average density of healthy cells is small. We then stop the simulation and *swap* the labels on the two density profiles, so that the (more realistic) initial condition for the following simulation consists of an array of peaks (cells) in the healthy cell density profile and a low density of cancer cells; i.e. for the initial conditions we define $\rho_1(\mathbf{r}, t = 0) = \rho_2^{\ddagger}(\mathbf{r}, t = 20)$ and $\rho_2(\mathbf{r}, t = 0) = \rho_1^{\ddagger}(\mathbf{r}, t = 20)$, where $\rho_1^{\ddagger}(\mathbf{r}, t = 20)$ and $\rho_2^{\ddagger}(\mathbf{r}, t = 20)$ are the final profiles at time $t = 20$ from the preliminary simulation.

Snapshots from the subsequent evolution are displayed in Fig. 6.17. These results are for the population growth constants $c_1 = c_2 = 0.5$ and the threshold nutrient concentration for healthy cells $\alpha = 2$. We fix the various cell-cell interaction parameters to be $\beta\varepsilon_{11} = \beta\varepsilon_{22} = 1$, $\beta\varepsilon_{12} = 1.5$ (so that density peaks of the two different cell types do not overlap), $R_{11} = 1$, $R_{22} = 1.2$ and $R_{12} = 1.1$. The nutrient uptake rate for cancer cells $\tilde{\lambda}_{n1} = 1$ and for healthy cells $\tilde{\lambda}_{n2} = 1$. The area of the domain in which the model is solved is 25.6×25.6 and the nutrient source is uniform, with $f(\mathbf{r}) = 1$ and $\tilde{S}_n = 9$. The diffusion coefficients for both cell species are equal, $\tilde{D}_c = \tilde{D}_h = 1$.

In Fig. 6.17 we plot the difference between the density profiles, $(\rho_1 - \rho_2)$. Positive values in this quantity correspond to regions where the cancer cells are present (where

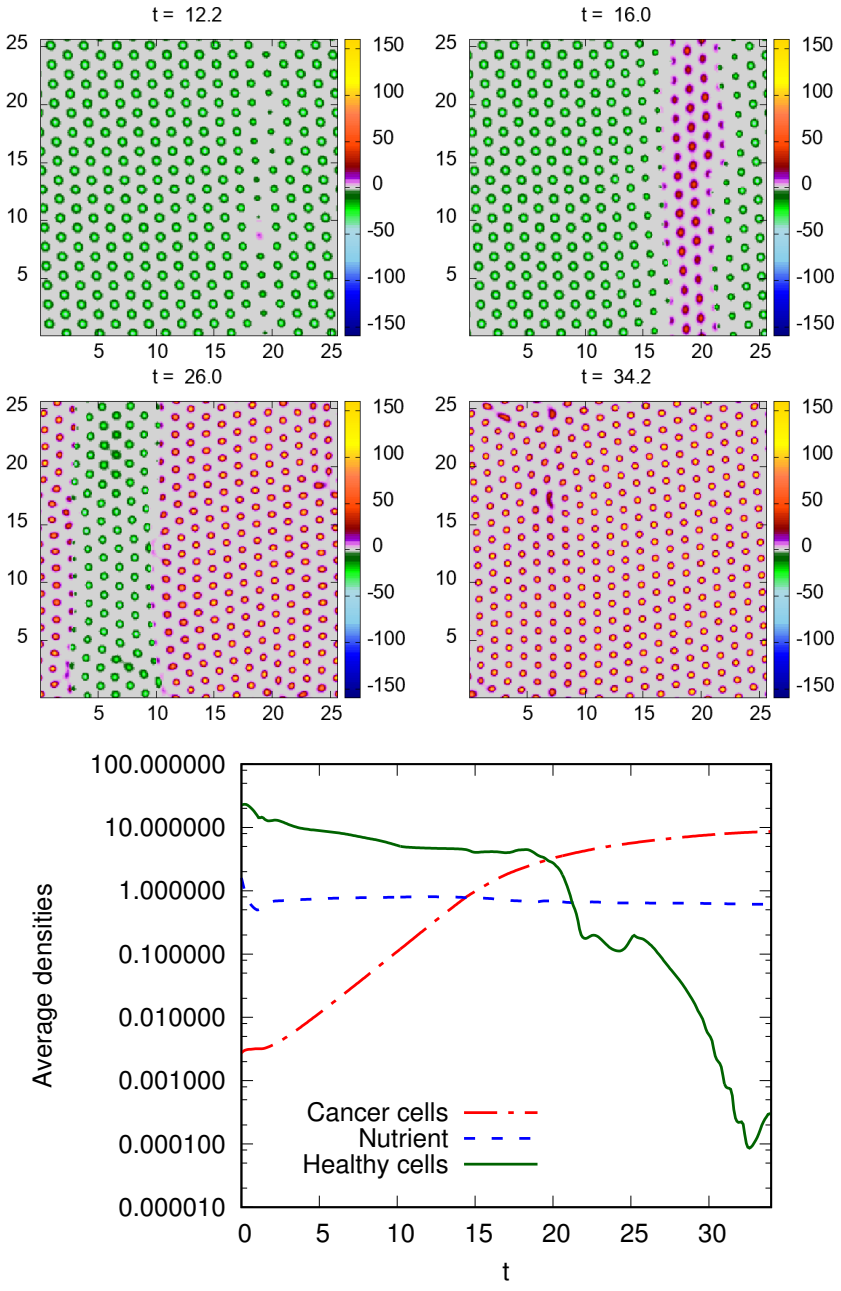

Figure 6.17: Snapshots of $(\rho_1 - \rho_2)$ at the times $t = 0.1$, 16, 26 and 34.2. The nutrient uptake rates $\tilde{\lambda}_{n1}$=1 and $\tilde{\lambda}_{n2}$=1, the population growth constants $c_1 = c_2 = 0.5$ and the threshold nutrient concentration for healthy cells $\alpha = 2$. The nutrient source is homogeneous, with $f(\mathbf{r}) = 1$ and $\tilde{S}_n = 9$. The area of the domain is 25.6×25.6 and $\Delta x = \Delta y = 0.1$. The cell-cell pair interaction potential parameters are $\beta\varepsilon_{11}$=1, $\beta\varepsilon_{12}$=1.5, $\beta\varepsilon_{11}$=1, $R_{11} = 1$, $R_{12} = 1.1$ and R_{22}=1.2. Bottom: the corresponding average cell density, [see Eq. (5.5.14)] and the average nutrient density [see Eq. (5.5.15)].

the peaks are purple-red, with yellow maxima) and negative values where the healthy cells are present (where the peaks are green). In regions that are grey, both densities are low. The Fig. 6.17 profiles are snapshots at the times t=12.2, 16, 26 and 34.2. At t=12.2 the first cancer cell becomes visible. As time increases, the cancer cells proliferate to form a vertical strip of cancerous tissue, shown in the top right panel. The fact that it is a vertical strip is due to the original initial conditions. By the time $t = 26$ the cancer cells have invaded two thirds of the healthy area and by $t = 34.2$ they cover the entire domain, having displaced all the healthy cells.

In the bottom panel of Fig. 6.17, we plot the average densities of the two species of cells and also of the nutrients, calculated using the two component generalisation of Eq. (5.5.14) and Eq. (5.5.15), respectively. We see that over time the average nutrient density is roughly constant, but the density of the healthy cells decreases over time, whilst the average density of the cancer cells increases. Interestingly, the average density of the healthy cells does not decrease monotonically; there are instances of brief increase, where healthy cells momentarily find gaps around the evolving cancer into which they try and grow. However, the overall trend is for the healthy cells to be displaced and die out.

Repeating the simulations corresponding to the results in Fig. 6.17 but using $R_{12} = 0.9$, such that $R_{12} < \frac{1}{2}(R_{11} + R_{22})$ [see Fig. 6.18], $R_{12} = 1$, such that $R_{12} = \frac{1}{2}(R_{11} + R_{22})$ [see Fig. 6.19], and also $R_{12} = 1.1$, such that $R_{12} > \frac{1}{2}(R_{11} + R_{22})$ [see Fig. 6.20]. Table 6.5 shows a summary of the information about the figures which include a few cancer cells dispersed throughout healthy tissue with different values of R_{12}.

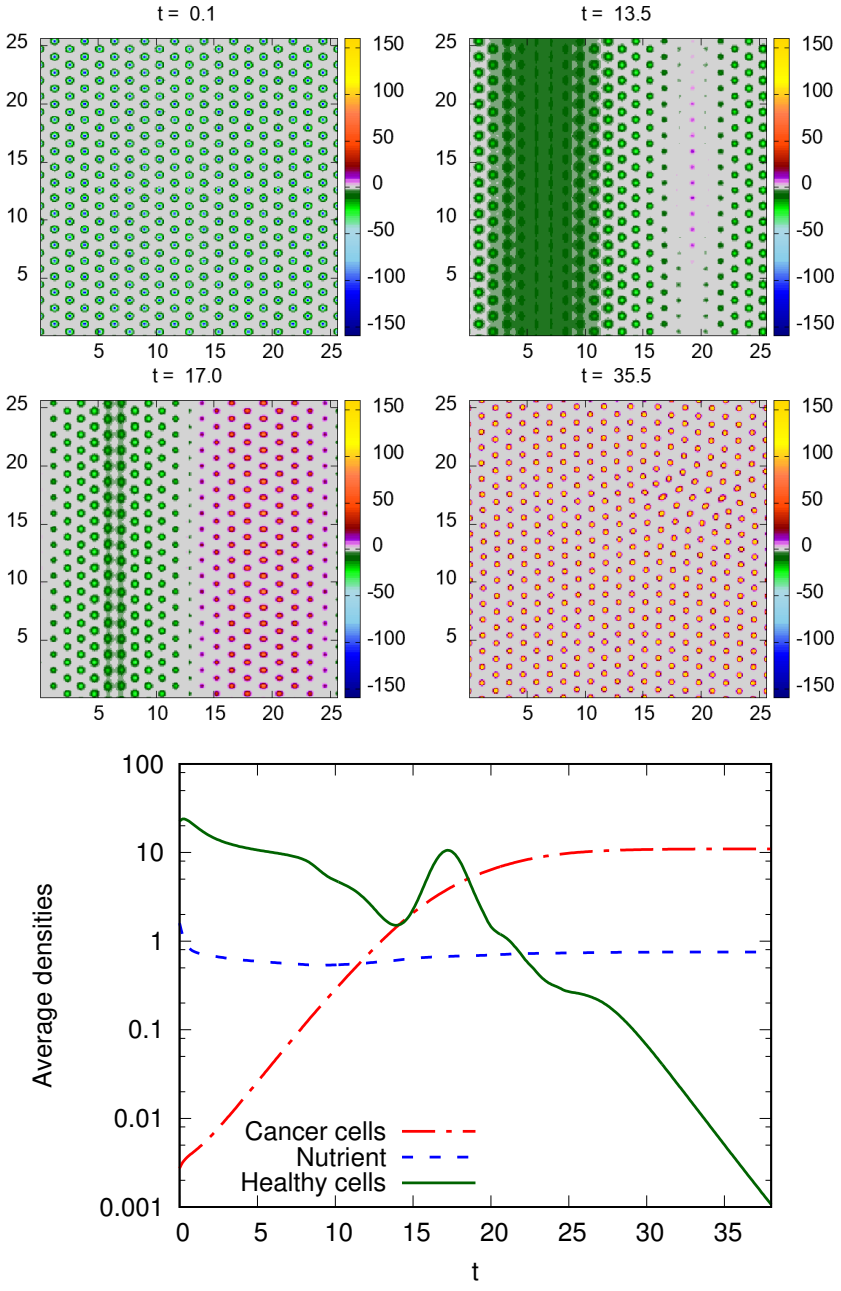

Figure 6.18: Top four panels: plots of $(\rho_1 - \rho_2)$, the density profile of the cancer cells minus the density of the healthy cells, at times $t = 0.1$, 13.5, 17 and 35.5. All the parameters here are the same as those in Fig. 6.17, except here the cross interaction pair potential radius is $R_{12} = 0.9$ and $R_{22} = 1$.

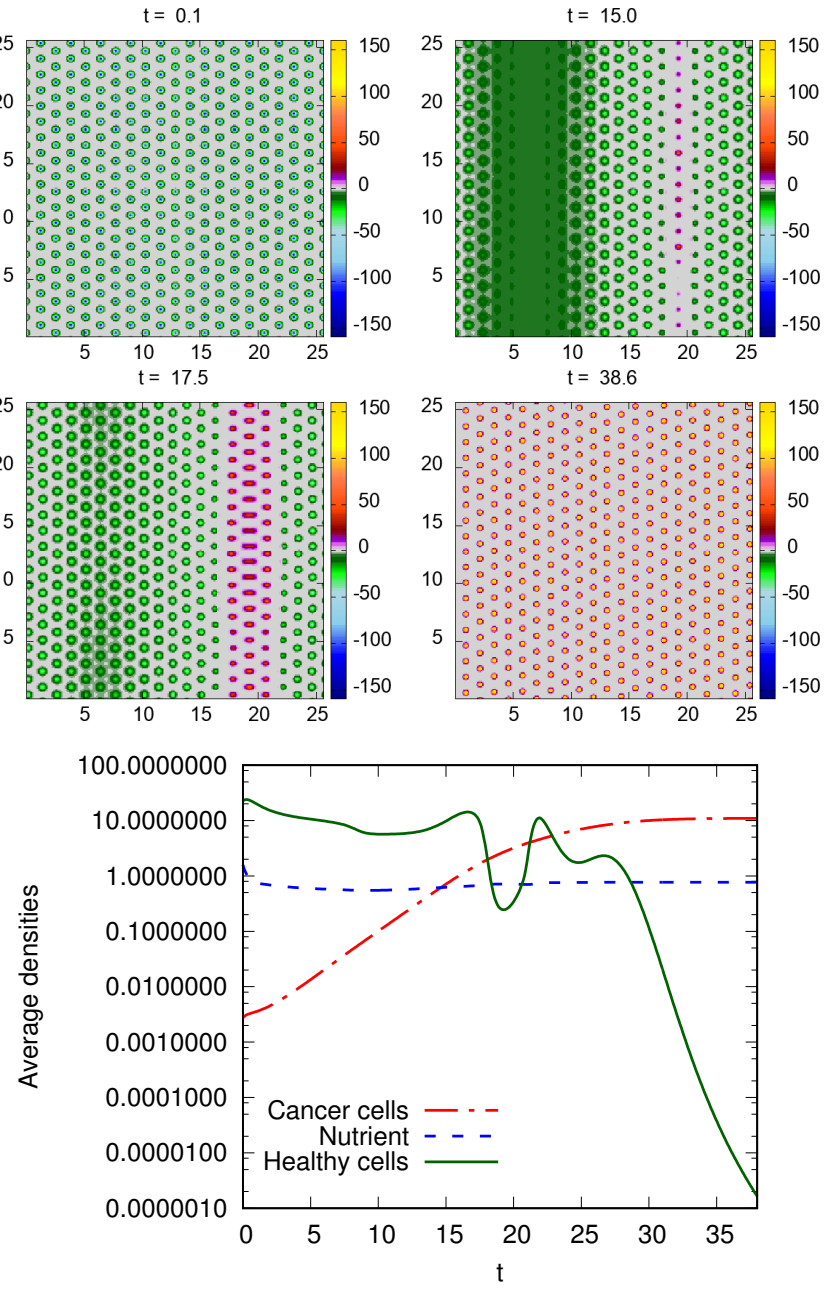

Figure 6.19: Snapshots of $(\rho_1 - \rho_2)$ at the times $t = 0.1, 15, 17.5$ and 36.6. All the parameters here are the same as those in Fig. 6.18, except here the cross interaction pair potential radius is $R_{12} = 1$, which is slightly larger.

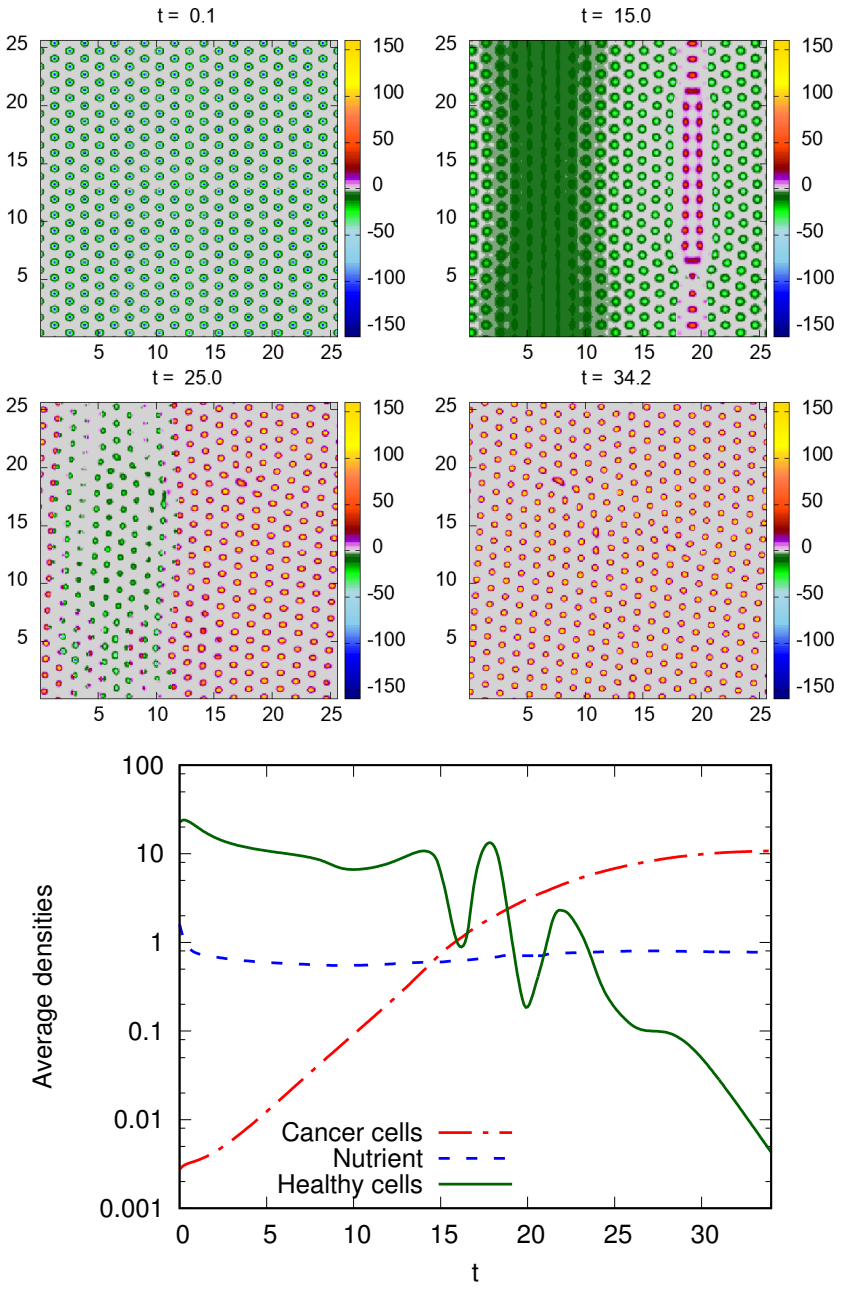

Figure 6.20: Snapshots of $(\rho_1 - \rho_2)$ at the times $t = 0.1$, 15, 25 and 34.2. All the parameters here are the same as those in Fig. 6.18, except here the cross interaction pair potential radius is $R_{12} = 1.1$.

Table 6.5: Dimensionless parameter values of the different examples

Density of cells	R_{11}	R_{12}	R_{22}	$\beta\varepsilon_{12}$	c_1	c_2	$\tilde{D}_c$	$\tilde{D}_h$	$\tilde{S}_n$	$\tilde{\lambda}_{n1}$	$\tilde{\lambda}_{n2}$
Fig. 6.17	1	1.1	1.2	1.5	0.5	0.5	1	1	9	1	1
Fig. 6.18	1	0.9	1	1.5	0.5	0.5	1	1	9	1	1
Fig. 6.19	1	1	1	1.5	0.5	0.5	1	1	9	1	1
Fig. 6.20	1	1.1	1	1.5	0.5	0.5	1	1	9	1	1

6.6 The effect of varying $\beta\varepsilon_{12}$ on the results

Guided by the results in Fig. 6.1, we now investigate the effect on the cancer development of varying the cross-species repulsion strength, $\beta\varepsilon_{12}$. In Fig. 6.21 we display results for three different values, $\beta\varepsilon_{12} = 1$, 1.75 and 2. The speed of penetration of the cancer cells into the healthy tissue increases as we increase the value $\beta\varepsilon_{12}$. For the results in the left hand column, which are for $\beta\varepsilon_{12} = 1$, there is no penetration of cancer cells into the healthy tissue. For $\beta\varepsilon_{12} = 1.75$ (middle column) the penetration starts at $t \approx 5.5$ whereas it begins at $t \approx 4.5$ for $\beta\varepsilon_{12} = 2$ (right hand column).

In Fig. 6.22 we plot the average densities of the cells and the nutrient as a function of time and also the trajectory of the system in the (ρ, ϕ) plane, corresponding to the results displayed in Fig. 6.21. This allows us to see that the increased degree of "melting" at times $t \sim \mathrm{O}(1)$ for smaller $\beta\varepsilon_{12}$ (particularly in the case with $\beta\varepsilon_{12} = 1$), is due to the fact that the linear stability threshold line is at higher total densities and is closer to the initial state. This means that the system spends a greater amount of time below the linear stability threshold line as it evolves along its trajectory in the (ρ, ϕ) plane. We also see from the plots of the average cell densities over time that the fluctuations over time in the density of the healthy cells increases with increasing $\beta\varepsilon_{12}$. In the (ρ, ϕ) plane, these fluctuations manifest as a meandering trajectory with zig-zag-like portions.

Table 6.6: The effect of varying $\beta\varepsilon_{12}$ and R_{12} on the penetration. See Figures 6.9, 6.10, 6.11, 6.21, 6.23 and 6.25 .

	$R_{12} < \frac{1}{2}(R_{11} + R_{22})$	$R_{12} = \frac{1}{2}(R_{11} + R_{22})$	$R_{12} > \frac{1}{2}(R_{11} + R_{22})$
$\beta\varepsilon_{12}$=1.00	No penetration	No penetration	No penetration
$\beta\varepsilon_{12}$=1.50	penetrate at $t \simeq 7.0$	penetrate at $t \simeq$6.5	penetrate at $t \simeq$5.5
$\beta\varepsilon_{12}$=1.75	penetrate at $t \simeq 5.5$	penetrate at $t \simeq$4.5	penetrate at $t \simeq$3.5
$\beta\varepsilon_{12}$=2.00	penetrate at $t \simeq 4.2$	penetrate at $t \simeq$3.5	penetrate at $t \simeq$3.0

Repeating the simulations corresponding to the results in Figs. 6.21 and 6.22, but using $R_{12} = 1.1$, such that $R_{12} > \frac{1}{2}(R_{11} + R_{22})$ [see Figs. 6.23 and 6.24], and also $R_{12} = 1$, such that $R_{12} = \frac{1}{2}(R_{11} + R_{22})$ [see Figs. 6.25 and 6.26], we find that the results are qualitatively similar, but the melting phenomenon for $\beta\varepsilon_{12} = 1$ is prolonged for the smaller value of R_{12} and shortened for the larger value of R_{12}. Also, the time at which the cancer cells penetrate into the healthy tissue first, is earlier for larger R_{12}.

Table 6.6 shows the relationship among the $\beta\varepsilon_{12}$, R_{12} and the penetration.

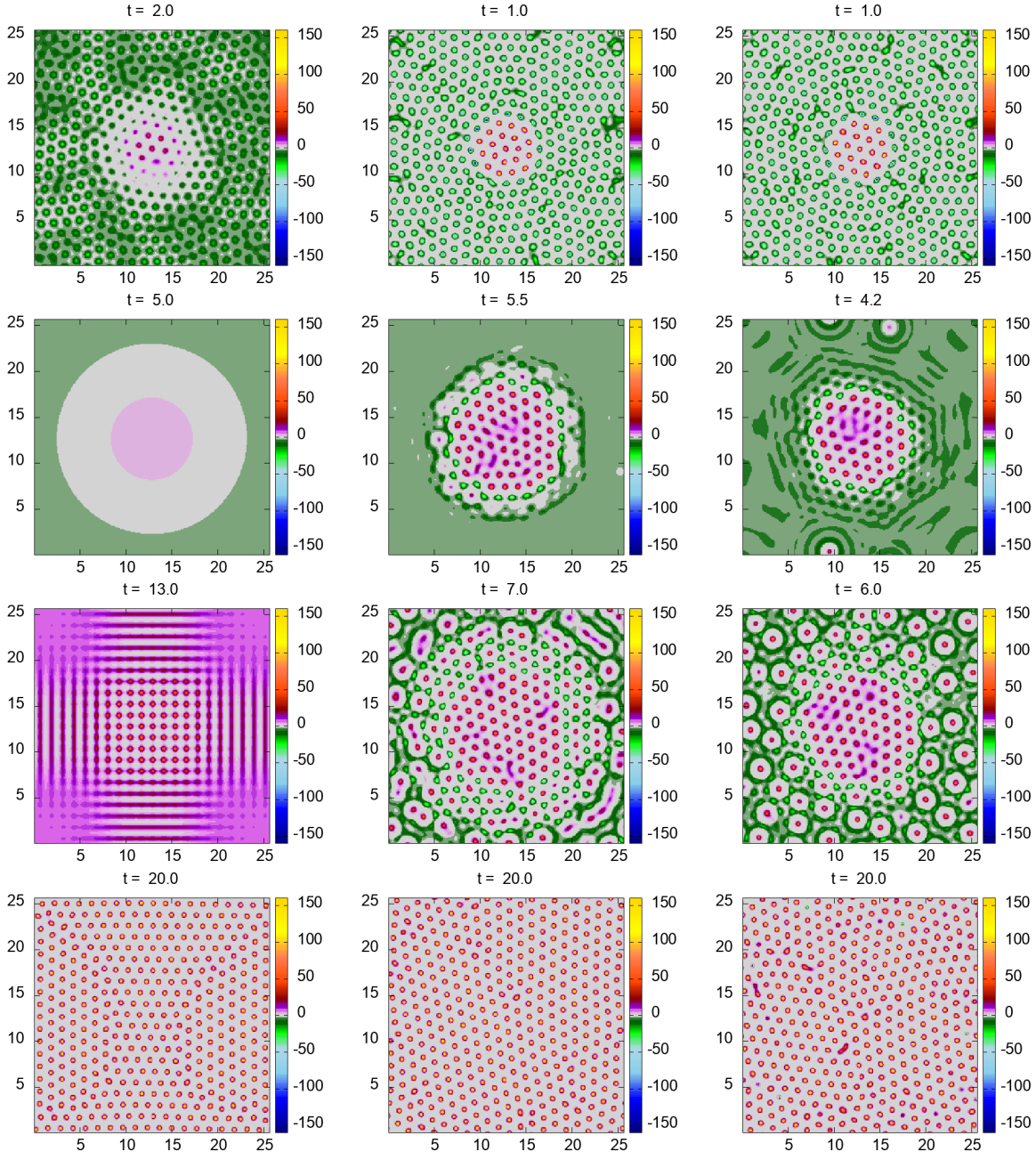

Figure 6.21: Snapshots of $(\rho_1 - \rho_2)$, for various $\beta\varepsilon_{12} = 1$ (left), $\beta\varepsilon_{12} = 1.75$ (middle) and $\beta\varepsilon_{12} = 2$ (right) and various different times, with time increasing from top to bottom, as indicated above. The other pair potential parameters are $\beta\varepsilon_{11} = \beta\varepsilon_{22} = 1$, $R_{11} = R_{22} = 1$ and $R_{12} = 0.9$. All the other model parameters are same as those in Fig. 6.17.

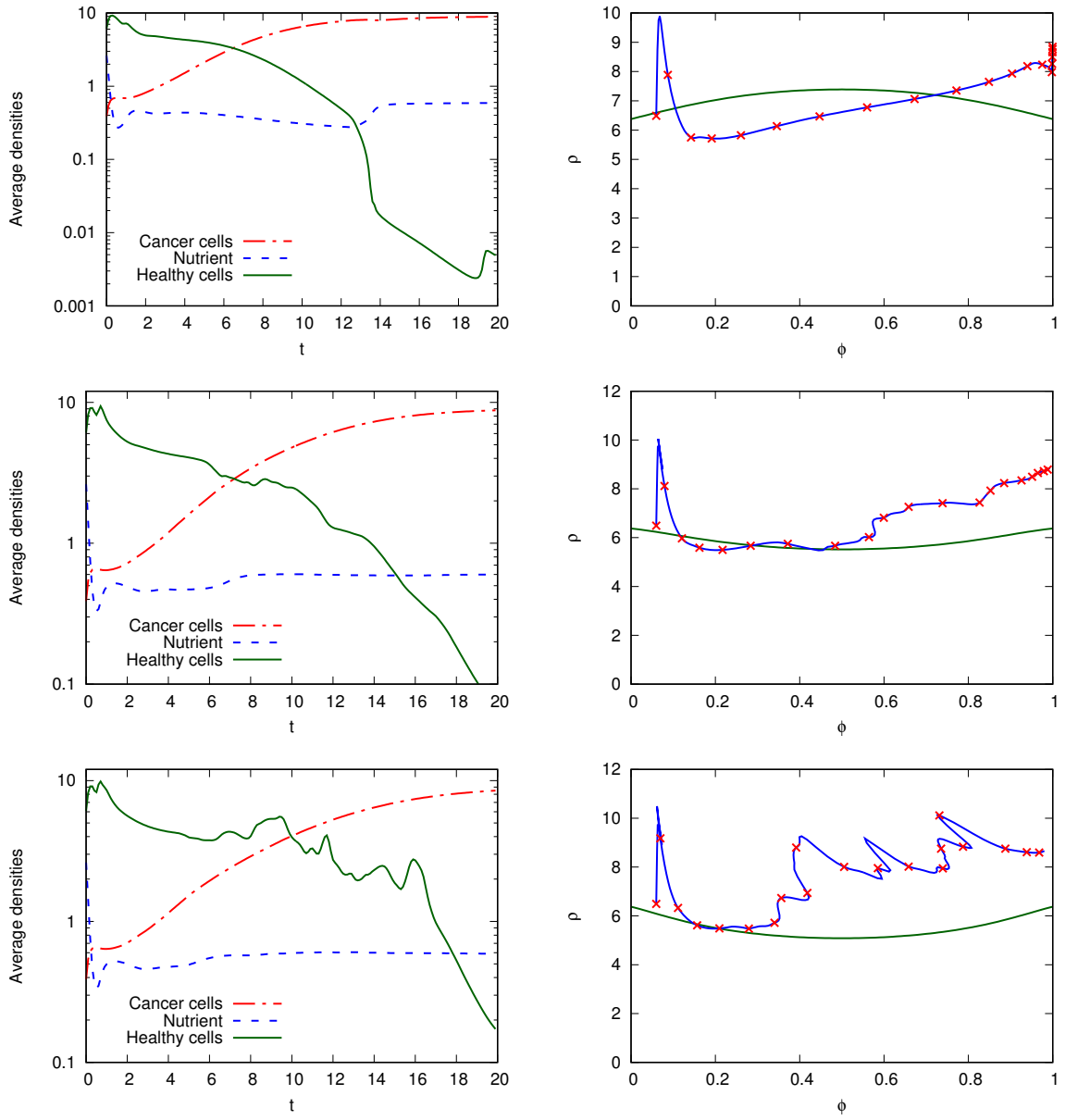

Figure 6.22: On the left are plots of the average cell densities [see Eq. (5.5.14)] and the average nutrient density [see Eq. (5.5.15)] and on the right plots of the trajectory in the (ρ, ϕ) plane with the corresponding linear stability threshold line, corresponding to the results in Fig. 6.21. These are for varying $\beta\varepsilon_{12} = 1$ (top), $\beta\varepsilon_{12} = 1.75$ (middle) and $\beta\varepsilon_{12} = 2$ (bottom).

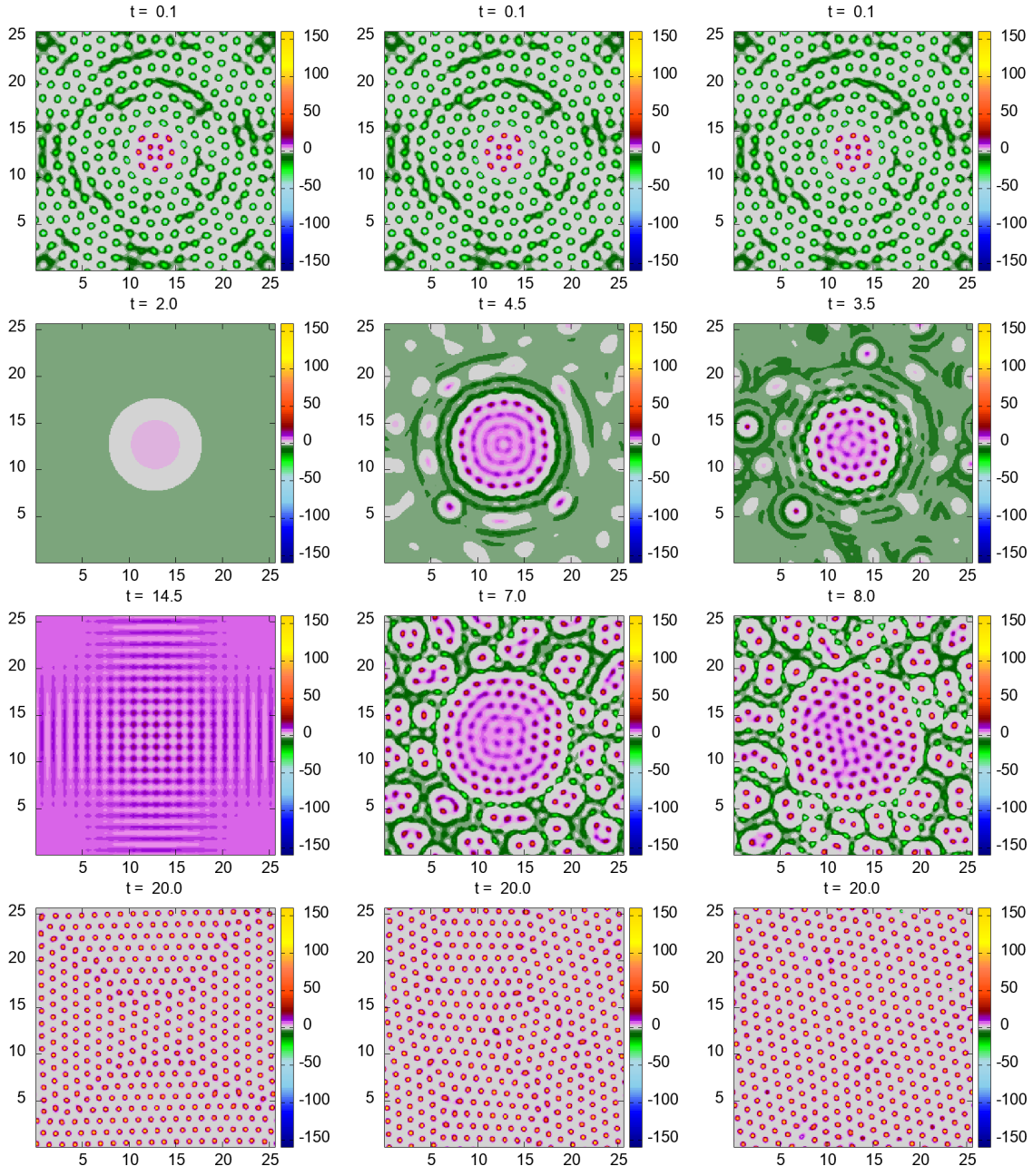

Figure 6.23: Snapshots of $(\rho_1 - \rho_2)$ at different times . All the parameters here are the same as those in Fig. 6.21, except here the cross interaction pair potential radius is $R_{12} = 1$.

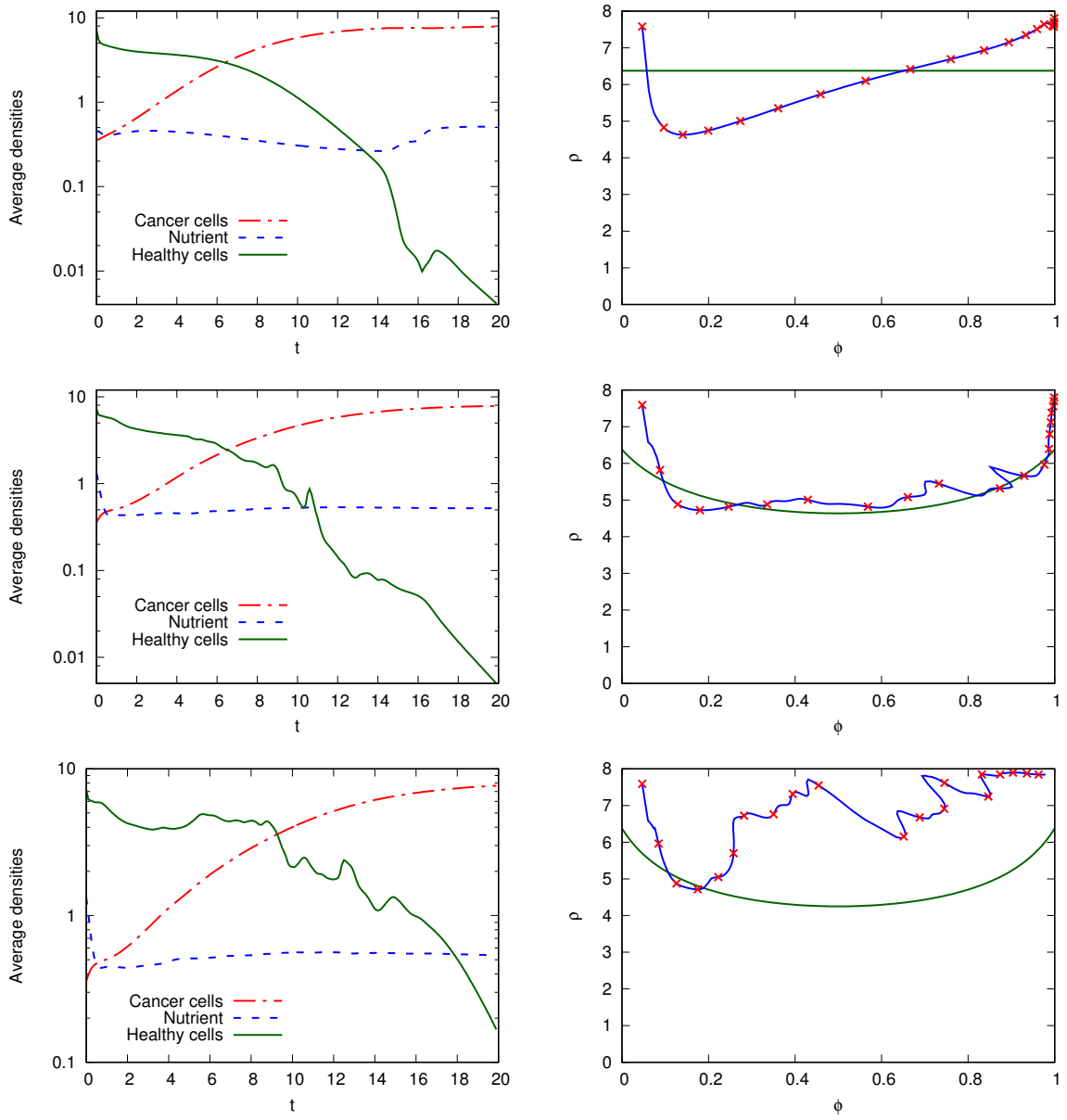

Figure 6.24: On the left are plots of the average cell densities [see Eq. (5.5.14)] and the average nutrient density [see Eq. (5.5.15)] and on the right plots of the trajectory in the (ρ, ϕ) plane with the corresponding linear stability threshold line, corresponding to the results in Fig. 6.23. These are for varying $\beta\varepsilon_{12} = 1$ (top), $\beta\varepsilon_{12} = 1.75$ (middle) and $\beta\varepsilon_{12} = 2$ (bottom).

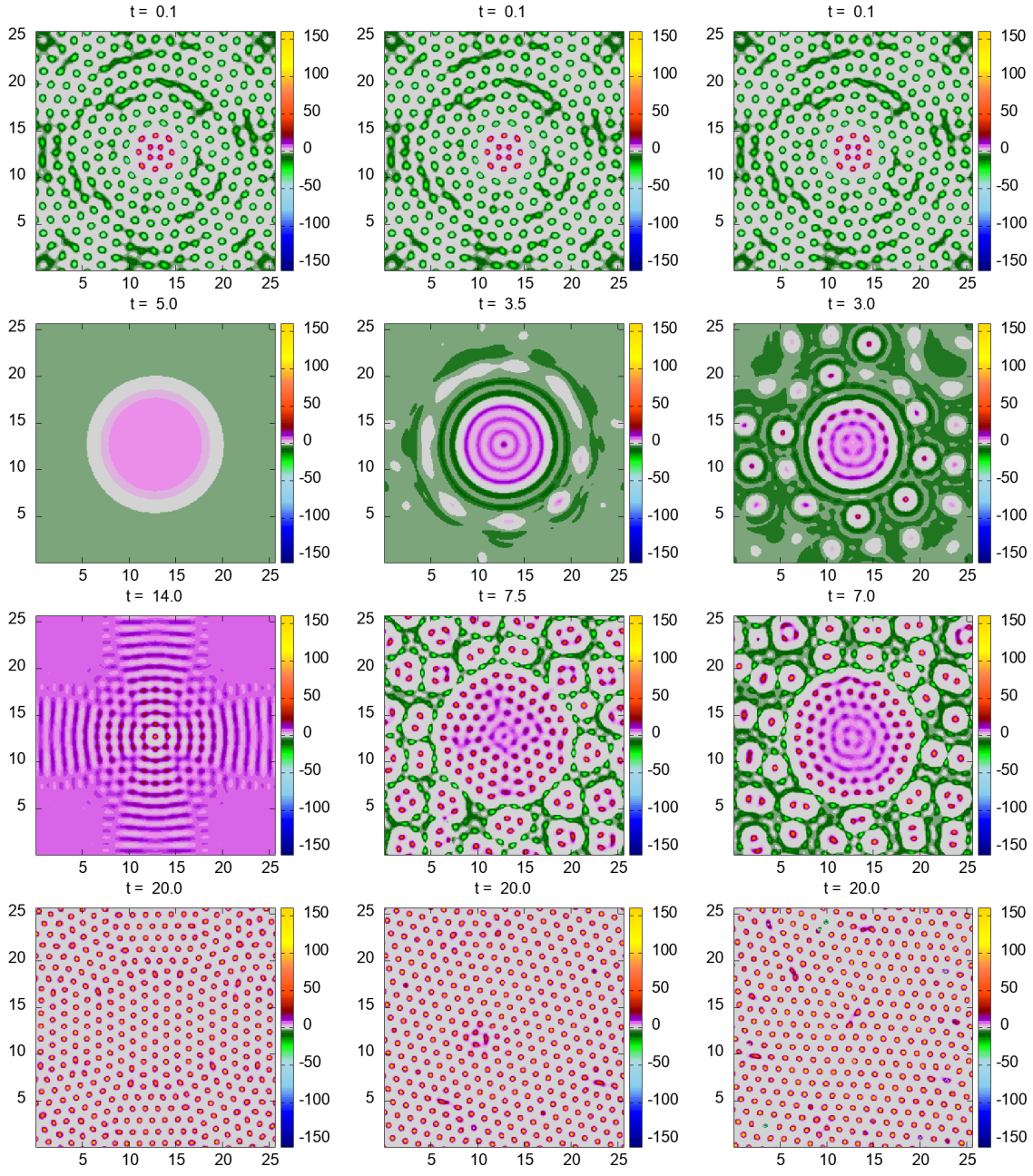

Figure 6.25: Snapshots of $(\rho_1 - \rho_2)$ at different times . All the parameters here are the same as those in Fig. 6.21, except here the cross interaction pair potential radius is R_{12}=1.1

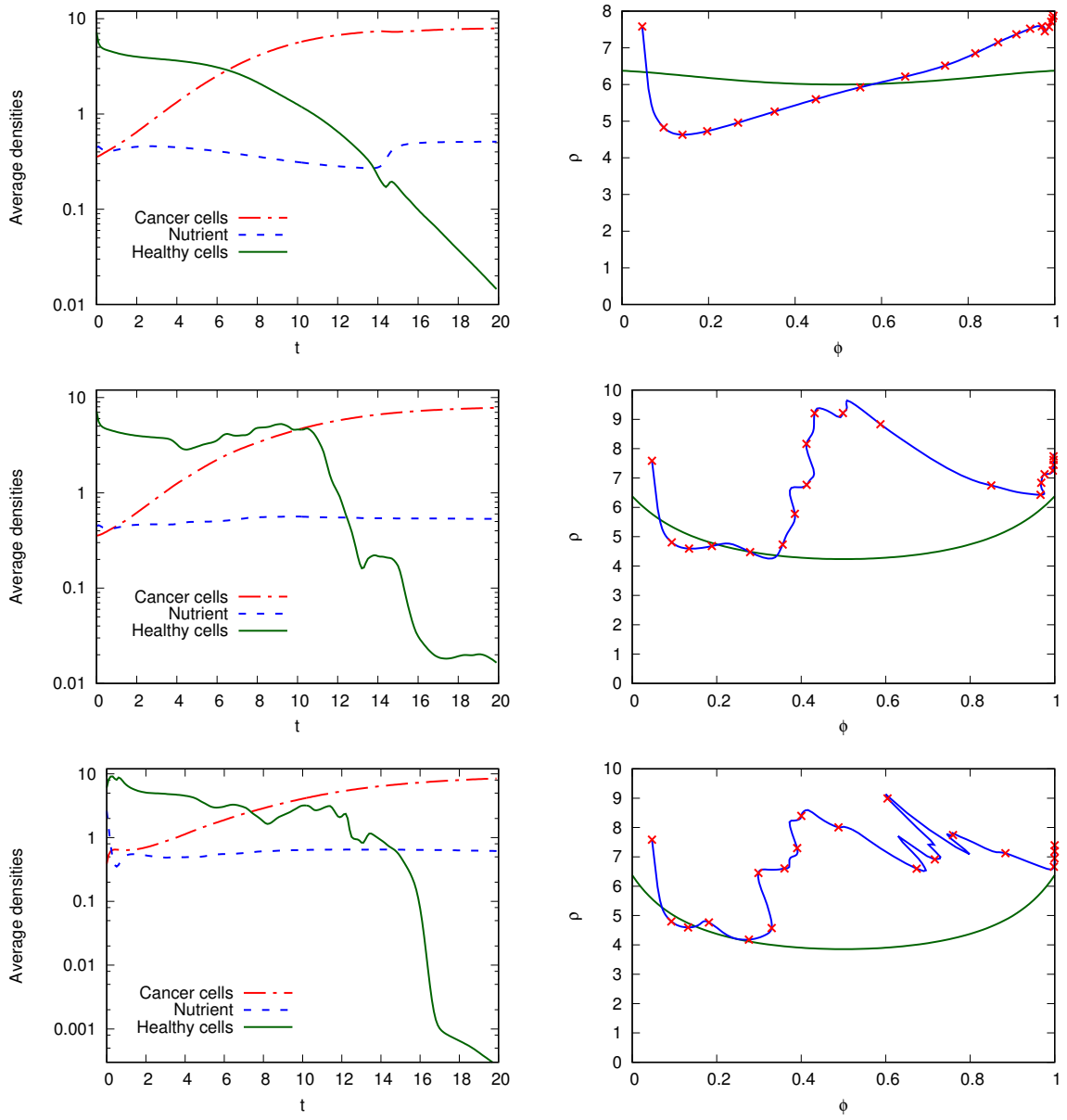

Figure 6.26: On the left are plots of the average cell densities [see Eq. (5.5.14)] and the average nutrient density [see Eq. (5.5.15)] and on the right plots of the trajectory in the (ρ, ϕ) plane with the corresponding linear stability threshold line, corresponding to the results in Fig. 6.25. These are for varying $\beta\varepsilon_{12} = 1$ (top), $\beta\varepsilon_{12} = 1.75$ (middle) and $\beta\varepsilon_{12} = 2$ (bottom).

CHAPTER 7

MODEL INCLUDING HAPTOTAXIS

7.1 Introduction

In this chapter we extend the model of the competition between cancer cells and healthy cells to include taxis which refers to several mechanisms through which cells can move in the direction corresponding to increasing or decreasing gradient of particular stimuli, such as the extracellular matrix (ECM). We present a preliminary analysis of a model to describe the haptotaxis process of cell movement in response to gradient in an extracellular matrix (ECM), based on the model proposed by Lowengrub [103]. The aim is to get an initial understanding of how other potentially destabilising processes interact with those discussed in previous chapters.

7.2 Mathematical model

The model system of integro-partial differential equations for the time evolution of the density profile of the cancer cells, the healthy cells, extracellular matrix (ECM) and nutrient is given by the following generalisation of the system of Eqs. (6.1.1)

$$\frac{\partial \rho_1(\mathbf{r},t)}{\partial t} = \Gamma_1 \nabla \cdot \left[\rho_1(\mathbf{r},t) \nabla \left(\frac{\delta \mathcal{F}[\rho_1(\mathbf{r},t), \rho_2(\mathbf{r},t)]}{\delta \rho_1(\mathbf{r},t)} \right) \right] + [\lambda_{m1} n(\mathbf{r},t) - \lambda_{d1}] \rho_1(\mathbf{r},t),$$

$$\frac{\partial \rho_2(\mathbf{r},t)}{\partial t} = \Gamma_2 \nabla \cdot \left[\rho_2(\mathbf{r},t) \nabla \left(\frac{\delta \mathcal{F}[\rho_1(\mathbf{r},t), \rho_2(\mathbf{r},t)]}{\delta \rho_2(\mathbf{r},t)} \right) \right] + [\lambda_{m2} n(\mathbf{r},t) - \lambda_{d2}] \rho_2(\mathbf{r},t),$$

$$\frac{\partial E(\mathbf{r},t)}{\partial t} = -\lambda_{E_1}(E(\mathbf{r},t) - E_1)\rho_1(\mathbf{r},t) - \lambda_{E_2}(E(\mathbf{r},t) - E_2)\rho_2(\mathbf{r},t),$$

$$\frac{\partial n(\mathbf{r},t)}{\partial t} = D_n \nabla^2 n(\mathbf{r},t) + S_n f(\mathbf{r}) - \lambda_{n1}\rho_1(\mathbf{r},t) n(\mathbf{r},t)) - \lambda_{n2}\rho_2(\mathbf{r},t) n(\mathbf{r},t). \quad (7.2.1)$$

The variables and parameters in the above system and their descriptions are summarised in Table 7.1. For such a system we may approximate the intrinsic Helmholtz free energy of the system as [134, 153],

$$\begin{aligned} \mathcal{F}[\{\rho_i(\mathbf{r},t)\}] &= k_B T \sum_{i=1}^{2} \int d\mathbf{r} \rho_i(\mathbf{r},t) \Big(\ln\left(\Lambda_i^2 \rho_i(\mathbf{r},t)\right) - 1 \Big) \\ &\quad + \frac{1}{2} \sum_{i,j=1}^{2} \int d\mathbf{r} \int d\mathbf{r}' \rho_i(\mathbf{r},t) V_{ij}(|\mathbf{r}-\mathbf{r}'|) \rho_j(\mathbf{r}',t) \\ &\quad - \chi_c \int d\mathbf{r} \rho_1(\mathbf{r},t) E(\mathbf{r},t) - \chi_h \int d\mathbf{r} \rho_2(\mathbf{r},t) E(\mathbf{r},t). \quad (7.2.2) \end{aligned}$$

The last two terms are key for modelling the haptotaxis; these incorporate the effect of the cells moving in the direction of gradients in $E(\mathbf{r},t)$. For this preliminary work,

we simplify the interaction potential by approximating as follows

$$V_{ij}(|\mathbf{r}-\mathbf{r}'|) = \delta(\mathbf{r}-\mathbf{r}')(\alpha_{ij} - \gamma_{ij}\nabla^2). \tag{7.2.3}$$

This results in the system being a PDE model, noting that

$$\int d\mathbf{r}'\delta(\mathbf{r}-\mathbf{r}') = 1. \tag{7.2.4}$$

The first variation of the free energy is

$$\frac{\delta\mathcal{F}}{\delta\rho_i(\mathbf{r},t)} = k_B T \ln(\Lambda_i^2\rho_i(\mathbf{r},t)) + \sum_{j=1}^{2}(\alpha_{ij} - \gamma_{ij}\nabla^2)\rho_j(\mathbf{r},t) - \chi_i E(\mathbf{r},t), \tag{7.2.5}$$

where χ_i represent the chemotaxis coefficients relevant to cancer and healthy cells respectively. Taking the gradient of Eq.(7.2.5) and substituting the result into Eq.(7.2.1), we obtain

$$\begin{aligned}\frac{\partial\rho_1(\mathbf{r},t)}{\partial t} &= \nabla\cdot\Bigg[\Gamma_1\rho_1(\mathbf{r},t)\nabla\Bigg(k_B T\ln(\Lambda_1^2\rho_1(\mathbf{r},t)) + \alpha_{11}\rho_1(\mathbf{r},t) + \alpha_{12}\rho_2(\mathbf{r},t)\\ &\quad -\gamma_{11}\nabla^2\rho_1(\mathbf{r},t) - \gamma_{12}\nabla^2\rho_2(\mathbf{r},t)\Bigg)\Bigg] - \chi_c\nabla\cdot\Big[\rho_1(\mathbf{r},t)\nabla E(\mathbf{r},t))\Big]\\ &\quad +\big[\lambda_{m1}n(\mathbf{r},t) - \lambda_{d1}\big]\rho_1(\mathbf{r},t),\end{aligned} \tag{7.2.6}$$

$$\begin{aligned}\frac{\partial\rho_2(\mathbf{r},t)}{\partial t} &= \nabla\cdot\Bigg[\Gamma_2\rho_2(\mathbf{r},t)\nabla\Bigg(k_B T\ln(\Lambda_2^2\rho_2(\mathbf{r},t)) + \alpha_{21}\rho_1(\mathbf{r},t) + \alpha_{22}\rho_2(\mathbf{r},t)\\ &\quad -\gamma_{21}\nabla^2\rho_1(\mathbf{r},t) - \gamma_{22}\nabla^2\rho_2(\mathbf{r},t)\Bigg)\Bigg] - \chi_h\nabla\cdot\Big[\rho_2(\mathbf{r},t)\nabla E(\mathbf{r},t))\Big]\\ &\quad +\big[\lambda_{m2}n(\mathbf{r},t) - \lambda_{d2}\big]\rho_2(\mathbf{r},t),\end{aligned} \tag{7.2.7}$$

$$\frac{\partial E(\mathbf{r},t)}{\partial t} = -\lambda_{E_1}(E(\mathbf{r},t)-E_1)\rho_1(\mathbf{r},t) - \lambda_{E_2}(E(\mathbf{r},t)-E_2)\rho_2(\mathbf{r},t). \tag{7.2.8}$$

$$\frac{\partial n(\mathbf{r},t)}{\partial t} = D_n\nabla^2 n(\mathbf{r},t)+S_n f(\mathbf{r})-\lambda_{n1}\rho_1(\mathbf{r},t)n(\mathbf{r},t))-\lambda_{n2}\rho_2(\mathbf{r},t)n(\mathbf{r},t). \quad (7.2.9)$$

The above PDE model is a simplified further generalisation of the model from the previous chapters to include the coupling to the local concentration of ECM. The variables and parameters in the above system and their descriptions are summarised in Table 7.1.

7.3 Linear stability analysis for the system

The governing equations for the time evolution of the density profile of cancer cells, healthy cells and the ECM are given by Eqs. (7.2.6), (7.2.7) and (7.2.8). We first consider the stability properties of a uniform state with densities ρ_1^o, ρ_2^o and E_o (defined later) and we consider small density fluctuations about the bulk values, of the form

$$\begin{aligned}\rho_1(\mathbf{r},t) &= \rho_1^o + \delta\rho(\mathbf{r},t)\\ &= \rho_1^o + \xi e^{i(\mathbf{k}.\mathbf{r})+\omega t},\end{aligned} \quad (7.3.1)$$

$$\begin{aligned}\rho_2(\mathbf{r},t) &= \rho_2^o + \zeta_1\delta\rho(\mathbf{r},t)\\ &= \rho_2^o + \zeta_1\xi e^{i(\mathbf{k}.\mathbf{r})+\omega t},\end{aligned} \quad (7.3.2)$$

and

$$\begin{aligned}E(\mathbf{r},t) &= E_o + \zeta_2\delta\rho(\mathbf{r},t)\\ &= E_o + \zeta_2\xi e^{i(\mathbf{k}.\mathbf{r})+\omega t},\end{aligned} \quad (7.3.3)$$

Table 7.1: Summary of the variables and parameters in the model given in Eqs. (7.2.6), (7.2.7) and (7.2.8).

State variables	Description
$\rho_1(\mathbf{r},t)$	Density of the cancer cells
$\rho_2(\mathbf{r},t)$	Density of the healthy cells
$E(\mathbf{r},t)$	Local concentration of ECM
$n(\mathbf{r},t)$	Local concentration of nutrients
$N_1(t)$	Total number of cancer cells in the system
$N_2(t)$	Total number of healthy cells in the system
$\bar{\rho}_1(t)$	Average cancer cell density
$\bar{\rho}_2(t)$	Average healthy cell density
$\bar{n}(t)$	Average nutrient density
$f(\mathbf{r})$	Function that defines where in space the nutrient source is located
α_{ij},γ_{ij}	Coefficients of interaction potential
λ_{d1}	Cancer cell death rate constant
λ_{d2}	Healthy cell death rate constant
λ_{n1}	Nutrient uptake rate constant for cancer cells
λ_{n2}	Nutrient uptake rate constant for healthy cells
λ_{m1}	Nutrient-dependent growth rate constant for cancer cells
λ_{m2}	Nutrient-dependent growth rate constantfor healthy cells
χ_c	Chemotaxis coefficient relevant to cancer cells
χ_h	Chemotaxis coefficient relevant to healthy cells
λ_{E_1}	Net rate of ECM production of cancer cells
λ_{E_2}	Net rate of ECM production of healthy cells
E_1	Saturated ECM value for cancer cells
E_2	Saturated ECM value for healthy cells
D_c	Cancer cell diffusion coefficient
D_h	Healthy cell diffusion coefficient
Γ_1	Cancer cell motility coefficient
Γ_2	Healthy cell motility coefficient
T	Temperature
k_B	Boltzmann's constant
ρ_0	constant reference density
D_n	Nutrient diffusion coefficient
S_n	The nutrient source
Λ_1,Λ_2	Thermal de Broglie wavelengths

where ξ is the initial amplitude of the sinusoidal perturbation that has wavenumber k, ζ_1 is the ratio between the amplitude of the modulation in the cancer and healthy components and ζ_2 is the ratio between the amplitude of the modulation in the cancer and ECM components. The growth/decay rate of this model is given by the dispersion relation $\omega = \omega(k)$, where $k = |\mathbf{k}|$. If we substitute Eqs. (7.3.1), (7.3.2) and (7.3.3) into Eq. (7.2.6), we get

$$\begin{aligned}\omega\delta\rho(\mathbf{r},t) &= -k^2\delta\rho(\mathbf{r},t) \\ &\quad +\nabla\cdot\left[(\rho_1^o+\delta\rho(\mathbf{r},t))\,\nabla\left(\alpha_{11}(\rho_1^o+\delta\rho(\mathbf{r},t))+\alpha_{12}(\rho_2^o+\zeta_1\delta\rho(\mathbf{r},t))\right)\right] \\ &\quad -\nabla\cdot\left[(\rho_1^o+\delta\rho(\mathbf{r},t))\,\nabla\left(\gamma_{11}\nabla^2(\rho_1^o+\delta\rho(\mathbf{r},t))+\gamma_{12}\nabla^2(\rho_2^o+\zeta_1\delta\rho(\mathbf{r},t))\right)\right] \\ &\quad -\chi_c\nabla\cdot\left[(\rho_1^o+\delta\rho(\mathbf{r},t))\,\nabla(E_o+\zeta_2\delta\rho(\mathbf{r},t))\right].\end{aligned} \tag{7.3.4}$$

As before, when going from Eq. (5.4.4) to Eq. (5.4.8), we obtain

$$\begin{aligned}\omega\delta\rho(\mathbf{r},t) &= -[k^2(D_1+\rho_1^o(\alpha_{11}+\alpha_{12}\zeta_1-\chi_c\zeta_2))+k^4(\rho_1^o(\gamma_{11}+\gamma_{12}\zeta_1))]\delta\rho(\mathbf{r},t) \\ &\quad +O(\delta\rho^2),\end{aligned} \tag{7.3.5}$$

Dividing both sides by $\delta\rho(\mathbf{r},t)$ and neglecting terms $O(\delta\rho)$ and higher we get

$$\omega(k) = -[k^2(D_1+\rho_1^o(\alpha_{11}+\alpha_{12}\zeta_1-\chi_c\zeta_2))+k^4(\rho_1^o(\gamma_{11}+\gamma_{12}\zeta_1))]. \tag{7.3.6}$$

In the same way, if we substitute Eqs. (7.3.1), (7.3.2) and (7.3.3) into Eqs. (7.2.7) and (7.2.8), we get

$$\zeta_1\omega(k) = -[k^2((D_2+\alpha_{22}\rho_2^o)\zeta_1+(\alpha_{12}-\chi_h\zeta_2)\rho_2^o)+k^4(\rho_2^o(\gamma_{12}+\gamma_{22}\zeta_1))] \tag{7.3.7}$$

and

$$\zeta_2\omega(k) = -\lambda_{E1}(E_o - E_1) - \lambda_{E2}(E_o - E_2)\zeta_1 - (\lambda_{E1}\rho_1^o + \lambda_{E2}\rho_2^o)\zeta_2. \tag{7.3.8}$$

From the steady state of Eq. (7.2.8), we get

$$E = E_o = \frac{\lambda_{E_1}\rho_1^o E_1 + \lambda_{E_2}\rho_2^o E_2}{\lambda_{E_1}\rho_1^o + \lambda_{E_2}\rho_2^o}. \tag{7.3.9}$$

Substituting Eq. (7.3.9) into Eq. (7.3.8), we obtain

$$\begin{aligned}\zeta_2\omega(k) &= -\lambda_{E1}\lambda_{E_2}\rho_2^o\left(\frac{E_2 - E_1}{\lambda_{E_1}\rho_1^o + \lambda_{E_2}\rho_2^o}\right) - \lambda_{E_1}\lambda_{E_2}\rho_1^o\left(\frac{E_1 - E_2}{\lambda_{E_1}\rho_1^o + \lambda_{E_2}\rho_2^o}\right)\zeta_1 \\ &\quad -(\lambda_{E1}\rho_1^o + \lambda_{E2}\rho_2^o)\zeta_2. \end{aligned} \tag{7.3.10}$$

Eqs. (7.3.6), (7.3.7) and (7.3.10) can be represented in matrix form, allowing for easier analysis,

$$\omega(k)\begin{pmatrix}1\\ \zeta_1\\ \zeta_2\end{pmatrix} = \mathbf{M}\begin{pmatrix}1\\ \zeta_1\\ \zeta_2\end{pmatrix}, \tag{7.3.11}$$

where

$$\mathbf{M} = \begin{pmatrix} -k^2(D_1 + \rho_1^o\alpha_{11}) - k^4\rho_1^o\gamma_{11} & -k^2\rho_1^o\alpha_{12} - k^4\rho_1^o\gamma_{12} & k^2\rho_1^o\chi_c \\ -k^2\rho_2^o\alpha_{12} - k^4\rho_2^o\gamma_{12} & -k^2(D_2 + \rho_2^o\alpha_{22}) - k^4\rho_2^o\gamma_{22} & k^2\rho_2^o\chi_h \\ -\lambda_{E1}\lambda_{E_2}\rho_2^o\left(\frac{E_2 - E_1}{\lambda_{E_1}\rho_1^o + \lambda_{E_2}\rho_2^o}\right) & -\lambda_{E_1}\lambda_{E_2}\rho_1^o\left(\frac{E_1 - E_2}{\lambda_{E_1}\rho_1^o + \lambda_{E_2}\rho_2^o}\right) & -(\lambda_{E_1}\rho_1^o + \lambda_{E_2}\rho_2^o) \end{pmatrix}. \tag{7.3.12}$$

We can now determine the dispersion relation $\omega(k)$ by calculating the eigenvalues of $\mathbf{M}$. When $\mathrm{Re}\{\omega(k)\} < 0$ for all wave numbers k, the system is linearly stable. If, however, $\mathrm{Re}\{\omega(k)\} > 0$ for any wave number k, then the uniform density state is

linearly unstable. The linear stability threshold is therefore associated with $|\mathbf{M}| = 0$ [149, 156].

7.3.1 No cell-cell interactions

In case of no cell-cell interactions, the coefficients of interaction potentials

$$\alpha_{ij} = \gamma_{ij} = 0 \qquad i, j = 1, 2. \tag{7.3.13}$$

Substituting (7.3.13) into (6.4.8), we get

$$\mathbf{M_0} = \begin{pmatrix} -k^2 D_1 & 0 & k^2 \rho_1^o \chi_c \\ 0 & -k^2 D_2 & k^2 \rho_2^o \chi_h \\ -\lambda_{E1}\lambda_{E_2}\rho_2^o \left(\frac{E_2 - E_1}{\lambda_{E_1}\rho_1^o + \lambda_{E_2}\rho_2^o}\right) & -\lambda_{E_1}\lambda_{E_2}\rho_1^o \left(\frac{E_1 - E_2}{\lambda_{E_1}\rho_1^o + \lambda_{E_2}\rho_2^o}\right) & -(\lambda_{E_1}\rho_1^o + \lambda_{E_2}\rho_2^o) \end{pmatrix}. \tag{7.3.14}$$

We can now determine the dispersion relation $\omega(k)$ by calculating the eigenvalues of $\mathbf{M_0}$. The eigenvalues are the roots of the characteristic polynomial

$$|\mathbf{M_0} - \lambda \mathbf{I}| = 0, \tag{7.3.15}$$

where $\mathbf{I}$ is the identity matrix. The characteristic polynomial in this case take the form

$$P(\lambda) = \lambda^3 + a_1\lambda^2 + a_2\lambda + a_3 = 0, \tag{7.3.16}$$

where the coefficients $a_i, i = 1, \cdots, 3$ are given by

$$a_1 = (D_1 + D_2), k^2 + \lambda_{E1}\, \rho_1^o + \lambda_{E2}\, \rho_2^o \tag{7.3.17}$$

$$
\begin{aligned}
a_2 \;=\; & \left(\frac{k^2}{\lambda_{E_1}\rho_1^o + \lambda_{E_2}\rho_2^o}\right)\Big[D_1D_2k^2\lambda_{E_1}\rho_1^o + D_1D_2k^2\lambda_{E_2}\rho_2^o - E_1\chi_c\lambda_{E_1}\lambda_{E_2}\rho_1^o\rho_2^o \\
& + E_1\chi_h\lambda_{E_1}\lambda_{E_2}\rho_1^o\rho_2^o + E_2\chi_c\lambda_{E_1}\lambda_{E_2}\rho_1^o\rho_2^o - E_2\chi_h\lambda_{E_1}\lambda_{E_2}\rho_1^o\rho_2^o + D_1{\lambda_{E_1}}^2\rho_1^{o2} \\
& + 2D_1\lambda_{E_1}\lambda_{E_2}\rho_1^o\rho_2^o + D_1{\lambda_{E_2}}^2\rho_2^{o2} + D_2{\lambda_{E_1}}^2\rho_1^{o2} + 2D_2\lambda_{E_1}\lambda_{E_2}\rho_1^o\rho_2^o \\
& + D_2{\lambda_{E_2}}^2\rho_2^{o2}\Big] \qquad (7.3.18)
\end{aligned}
$$

$$
\begin{aligned}
a_3 \;=\; & \left(\frac{k^4}{\lambda_{E_1}\rho_1^o + \lambda_{E_2}\rho_2^o}\right)\Big[D_1E_1\chi_h\lambda_{E_1}\lambda_{E_2}\rho_1^o\rho_2^o - D_1E_2\chi_h\lambda_{E_1}\lambda_{E_2}\rho_1^o\rho_2^o \\
& - D_2E_1\chi_c\lambda_{E_1}\lambda_{E_2}\rho_1^o\rho_2^o + D_2E_2\chi_c\lambda_{E_1}\lambda_{E_2}\rho_1^o\rho_2^o \\
& + D_1D_2{\lambda_{E_1}}^2\rho_1^{o2} + 2D_1D_2\lambda_{E_1}\lambda_{E_2}\rho_1^o\rho_2^o + D_1D_2{\lambda_{E_2}}^2\rho_2^{o2}\Big] \qquad (7.3.19)
\end{aligned}
$$

We require conditions on the $a_i, i = 1, \cdots, 3$ such that the zeros of $P(\lambda)$ have $\mathrm{Re}\{\lambda\} < 0$. The necessary and sufficient conditions for this to hold are the Routh–Hurwitz conditions. The form of these conditions for the cubic equation are [157]

$$
a_1 > 0, \qquad a_3 > 0; \qquad a_1a_2 - a_3 > 0. \qquad (7.3.20)
$$

According to the Routh–Hurwitz conditions (7.3.20) of stability, a sufficient conditions for instability induced by haptotaxis alone are $\mathrm{E}_1 \neq E_2$ and $D_1\chi_c \neq D_2\chi_h$.

7.3.2 Full model

The linear stability threshold is determined by $|\mathbf{M}| = 0$, i.e. by the condition [149, 156]

$$
D(k) \equiv C_1k^8 + C_2k^6 + C_3k^4 = 0, \qquad (7.3.21)
$$

where

$$C_1 = -(\lambda_{E_1}\rho_1^o + \lambda_{E_2}\rho_2^o)(\gamma_{11}\gamma_{22} - \gamma_{12}^2)\rho_1^o\rho_2^o \tag{7.3.22}$$

$$\begin{aligned}
C_2 \;=\; & -\left(\frac{1}{\lambda_{E_1}\rho_1^o + \lambda_{E_2}\rho_2^o}\right)\Big[- E_1\chi_c\gamma_{12}\lambda_{E_1}\lambda_{E_2}\rho_1^{o2}\rho_2^o - E_1\chi_c\gamma_{22}\lambda_{E_1}\lambda_{E_2}\rho_1^o\rho_2^{o2} \\
& + E_1\chi_h\gamma_{11}\lambda_{E_1}\lambda_{E_2}\rho_1^{o2}\rho_2^o + E_1\chi_h\gamma_{12}\lambda_{E_1}\lambda_{E_2}\rho_1^o\rho_2^{o2} + E_2\chi_c\gamma_{12}\lambda_{E_1}\lambda_{E_2}\rho_1^{o2}\rho_2^o \\
& + E_2\chi_c\gamma_{22}\lambda_{E_1}\lambda_{E_2}\rho_1^o\rho_2^{o2} - E_2\chi_h\gamma_{11}\lambda_{E_1}\lambda_{E_2}\rho_1^{o2}\rho_2^o - E_2\chi_h\gamma_{12}\lambda_{E_1}\lambda_{E_2}\rho_1^o\rho_2^{o2} \\
& + \alpha_{11}\gamma_{22}\lambda_{E_1}^2\rho_1^{o3}\rho_2^o + 2\alpha_{11}\gamma_{22}\lambda_{E_1}\lambda_{E_2}\rho_1^{o2}\rho_2^{o2} + \alpha_{11}\gamma_{22}\lambda_{E_2}^2\rho_1^o\rho_2^{o3} \\
& - 2\alpha_{12}\gamma_{12}{\lambda_{E_1}}^2\rho_1^{o3}\rho_2^o - 4\alpha_{12}\gamma_{12}\lambda_{E_1}\lambda_{E_2}\rho_1^{o2}\rho_2^{o2} - 2\alpha_{12}\gamma 12{\lambda_{E_2}}^2\rho_1^o\rho_2^{o3} \\
& + \alpha_{22}\gamma_{11}\lambda_{E_1}^2\rho_1^{o3}\rho_2^o + 2\alpha_{22}\gamma 11\lambda_{E_1}\lambda_{E_2}\rho_1^{o2}\rho_2^{o2} + \alpha_{22}\gamma 11{\lambda_{E_2}}^2\rho_1^o\rho_2^{o3} \\
& + D_1\gamma_{22}{\lambda_{E_1}}^2\rho_1^{o2}\rho_2^o + 2D_1\gamma_{22}\lambda_{E_1}\lambda_{E_1}\rho_1^o\rho_2^{o2} + D_1\gamma_{22}{\lambda_{E_2}}^2\rho_2^{o3} \\
& + D_2\gamma_{11}{\lambda_{E_1}}^2\rho_1^{o3} + 2D_2\gamma_{11}\lambda_{E_1}\lambda_{E_2}\rho_1^{o2}\rho_2^o + D_2\gamma_{11}{\lambda_{E_2}}^2\rho_1^o\rho_1^{o2}\Big]
\end{aligned} \tag{7.3.23}$$

$$\begin{aligned}
C_3 \;=\; & -\left(\frac{1}{\lambda_{E_1}\rho_1^o + \lambda_{E_2}\rho_2^o}\right)\Big[- E_1\chi_c\alpha_{12}\lambda_{E_1}\lambda_{E_2}\rho_1^{o2}\rho_2^o - E_1\chi_c\alpha_{22}\lambda_{E_1}\lambda_{E_2}\rho_1^o\rho_2^{o2} \\
& + E_1\chi_h\alpha_{11}\lambda_{E_1}\lambda_{E_2}\rho_1^{o2}\rho_2^o + E_1\chi_h\alpha_{12}\lambda_{E_1}\lambda_{E_2}\rho_1^o\rho_2^{o2} + E_2\chi_c\alpha_{12}\lambda_{E_1}\lambda_{E_2}\rho_1^{o2}\rho_2^o \\
& + E_2\chi_c\alpha_{22}\lambda_{E_1}\lambda_{E_2}\rho_1^o\rho_2^{o2} - E_2\chi_h\alpha_{11}\lambda_{E_1}\lambda_{E_2}\rho_1^{o2}\rho_2^o - E_2\chi_h\alpha_{12}\lambda_{E_1}\lambda_{E_2}\rho_1^o\rho_2^{o2} \\
& + \alpha_{11}\alpha_{22}\lambda_{E_1}^2\rho_1^{o3}\rho_2^o + 2\alpha_{11}\alpha_{22}\lambda_{E_1}\lambda_{E_2}\rho_1^{o2}\rho_2^{o2} + \alpha_{11}\alpha_{22}\lambda_{E_2}^2\rho_1^o\rho_2^{o3} \\
& - \alpha_{12}^2\lambda_{E_1}^2\rho_1^{o3}\rho_2^o - 2{\alpha_{12}}^2\lambda_{E_1}\lambda_{E_2}\rho_1^{o2}\rho_2^{o2} - {\alpha_{12}}^2{\lambda_{E_2}}^2\rho_1^o\rho_2^{o3} \\
& + D_1E_1\chi_h\lambda_{E_1}\lambda_{E_2}\rho_1^o\rho_2^o - D_1E_2\chi_h\lambda_{E_1}\lambda_{E_2}\rho_1^o\rho_2^o + D_1\alpha_{22}{\lambda_{E_1}}^2\rho_1^{o2}\rho_2^o \\
& + 2D_1\alpha_{22}\lambda_{E_1}\lambda_{E_2}\rho_1^o\rho_2^{o2} + D_1\alpha_{22}{\lambda_{E_2}}^2\rho_2^{o3} \\
& - D_2E_1\chi_c\lambda_{E_1}\lambda_{E_2}\rho_1^o\rho_2^o + D_2E_2\chi_c\lambda_{E_1}\lambda_{E_2}\rho_1^o\rho_2^o + D_2\alpha_{11}{\lambda_{E_1}}^2\rho_1^{o3} \\
& + 2D_2\alpha_{11}\lambda_{E_1}\lambda_{E_2}\rho_1^{o2}\rho_2^o + D_2\alpha_{11}{\lambda_{E_2}}^2\rho_1^o\rho_2^{o2} \\
& + D_1D_2{\lambda_{E_1}}^2\rho_1^{o2} + 2D_1D_2\lambda_{E_1}\lambda_{E_2}\rho_1^o\rho_2^o + D_1D_2{\lambda_{E_2}}^2\rho_2^{o2}\Big]
\end{aligned} \tag{7.3.24}$$

From the coefficients of dispersion relation we conclude that the additional sufficient condition for instability for the full system is $\alpha_{11}\alpha_{22} - \alpha_{12}^2 \neq 0$.

In Fig. 7.1 we display the linear stability threshold for different values of the concentration $\phi \equiv \rho_1/\rho$, where $\rho \equiv \rho_1 + \rho_2$ is the total density and ρ_1, ρ_2 are densities of cancer and healthy cells respectively for varying χ_c. For state points above the linear stability threshold line in Fig. 7.1, the system exhibits a separation of the cells. The instability line is obtained by tracing the locus defined by $D(k_c) = 0$ and $D'(k_c) = 0$, where $D(k)$ is given by Eq. (6.4.14) and $k_c \neq 0$ is the wave number at the minimum of $D(k)$ [i.e. $D(k = k_c) = 0$] [154]. We see that increasing χ_c makes the system work against demixing by being stable over a larger region. However, we see the opposite effect in Fig. 7.2, where we see that increasing χ_h increases the unstable area.

In Figs. 7.3–7.4 we display the linear stability threshold for varying λ_{E_1} and λ_{E_2} respectively. The graphs show that unstable area decreases when we increase the values of λ_{E_i} for small values, λ_{E_i}=0.1 and 1.0. however, this area increases again for large values, for example when λ_{E_i}=10, and becomes close to the original area (i.e. the case when λ_{E_i}=0). This is to be expected as the stabilising $\lambda_{E_1}(E(\mathbf{r}, t) - E_1)$ term is more dominant in Eq. (7.2.7).

7.4 Conclusion

Haptotaxis (and by mathematical equivalence chemotaxis) can change the stability properties of the system and can induce instabilities when the cell-cell interaction

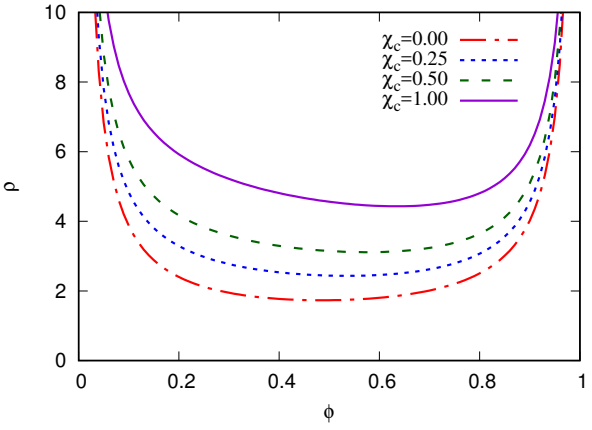

Figure 7.1: The linear stability limit for the two species cells [see Eqs. (7.2.6), (7.2.7) and (7.2.8)] with E_1=3, E_2=10, $\alpha_{11} = \alpha_{22} = 1$, α_{12}=2.1, $\gamma_{11} = \gamma_{22} = 1$, γ_{12}=0.5, λ_{E_1}=0.5, λ_{E_2}=0.25, χ_h=0.03, $D_c = D_h = 1$ and for varying χ_c as given in the key, plotted in the total density $\rho \equiv \rho_1 + \rho_2$ versus concentration $\phi \equiv \rho_1/\rho$ plane. The uniform density state is linearly unstable above this line.

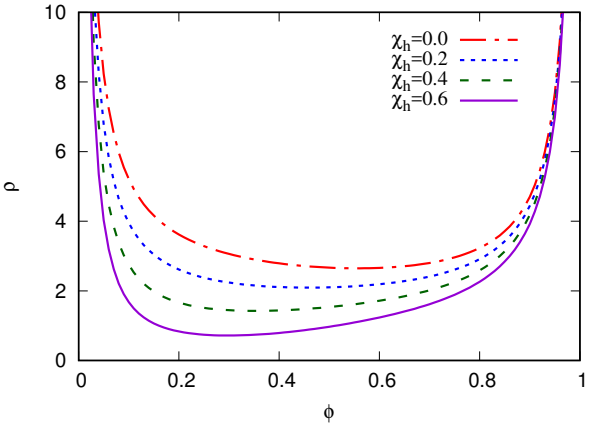

Figure 7.2: The linear stability limit for the two species cells [see Eqs. (7.2.6), (7.2.7) and (7.2.8)] with E_1=3, E_2=10, $\alpha_{11} = \alpha_{22} = 1$, α_{12}=2.1, $\gamma_{11} = \gamma_{22} = 1$, γ_{12}=0.5, λ_{E_1}=0.5, λ_{E_2}=0.25, χ_c=0.3, $D_c = D_h = 1$ and for varying χ_h as given in the key, plotted in the total density $\rho \equiv \rho_1 + \rho_2$ versus concentration $\phi \equiv \rho_1/\rho$ plane. The uniform density state is linearly unstable above this line.

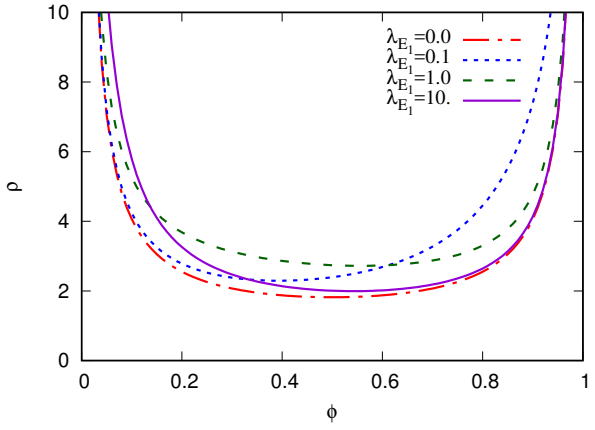

Figure 7.3: The linear stability limit for the two species cells [see Eqs. (7.2.6), (7.2.7) and (7.2.8)] with E_1=3, E_2=10, $\alpha_{11} = \alpha_{22} = 1$, α_{12}=2.1, $\gamma_{11} = \gamma_{22} = 1$, γ_{12}=0.5, λ_{E_2}=0.5, χ_c=0.6, χ_h=0.03, $D_c = D_h = 1$ and for varying λ_{E_1} as given in the key, plotted in the total density $\rho \equiv \rho_1 + \rho_2$ versus concentration $\phi \equiv \rho_1/\rho$ plane. The uniform density state is linearly unstable above this line.

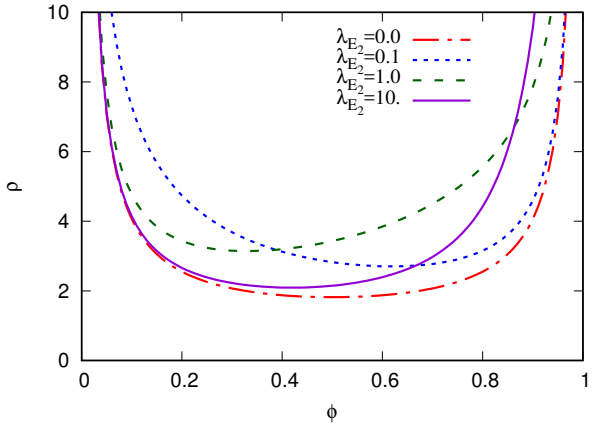

Figure 7.4: The linear stability limit for the two species cells [see Eqs. (7.2.6), (7.2.7) and (7.2.8)] with E_1=3, E_2=10, $\alpha_{11} = \alpha_{22} = 1$, α_{12}=2.1, $\gamma_{11} = \gamma_{22} = 1$, γ_{12}=0.5, λ_{E_1}=0.5, χ_c=0.6, χ_h=0.03, $D_c = D_h = 1$ and for varying λ_{E_2} as given in the key, plotted in the total density $\rho \equiv \rho_1 + \rho_2$ versus concentration $\phi \equiv \rho_1/\rho$ plane. The uniform density state is linearly unstable above this line.

parameters lead to stability in the taxis-free case.

This is a preliminary analysis and work to be done includes simulating the full PDE system and exploring further the parameters space.

CHAPTER 8

CONCLUSIONS AND FUTURE WORKS

8.1 Conclusions

In this study, we have used DDFT to describe microscopic cell-cell interactions within a simple model of nutrient driven tissue growth. The theory was applied for a single cell type (chapter 5) and for two cell types (chapter 6), the latter representing, for example, the interaction between healthy and tumour cells; this approach can easily be generalised to describe more cells for example, and also one can extend the model of the competition between cancer cells and healthy cells to include haptotaxis (chapter 7). The resulting models consist of coupled integro-partial differential equations with nonlinear source terms describing nutrient driven growth. This level of description is common in discrete models, but their analysis is limited mainly to numerical simulation; one of the main advantages of the DDFT approach is that the model is amenable to mathematical analysis, providing greater insights into the na-

ture of the numerical results. For instance, the linear stability analysis of Secs. 5.4, 6.4 and 7.3 identified parameter regimes for which stable peaks arise, representing the locations of cell centres, as demonstrated in the simulations in Secs. 5.5 and 6.5. Whilst some parameters can be estimated readily from the experimental literature, this analysis also goes some way to estimate the associated parameters in the model that are difficult to determine from direct measurements (e.g. the effective cell-cell cross interaction radius R_{12}). A further outcome of our linear stability analysis in the competition case, is the observation that as the cell radii ratio R_{22}/R_{11} is increased, the two wavenumbers at which the system can become linearly unstable move apart leading to the linear stability threshold to develop a cusp. If the radii ratio is sufficiently large then the system can be linearly unstable at two quite different wavenumbers and the interaction between these can produce a wide range of different structures [149, 156, 158] which are interesting from the pattern-formation perspective, and may also have some biological relevance.

There is still much required in the development of the basic theory before it can be applied directly to experimental results. However, numerical results reflect qualitatively the expected results based on observation, despite the use of simple growth kinetics and interaction potentials. For example, the mean densities (a proxy for total number of cells) in Figs. 5.8 and 5.11 qualitatively resemble Gompertzian or logistic type growth curves often reported in tumour growth models [159]. A further noteworthy aspect of the model is the splitting events shown in Fig. 5.3, reflecting mitosis. We note also that for a uniform nutrient distribution, such events are not observed at very large times as the arrangement of the cells settles to fixed configuration; such results are reflective of the cellular rest states observed in mature liver and muscle tissues.

In the simulations of Chapter 6, the parameter values for the kinetics guarantee that the tumour cells will overrun the healthy cells. However, it is interesting that the manner by which this is done depends on the value of the interaction parameters R_{ij} and ε_{ij} and in particular the cross-interaction radius R_{12} and energy ε_{12}. Although the critical values for R_{12} suggested here are not strictly defined, it was found that (i) if $R_{12} < \frac{1}{2}(R_{11} + R_{22})$, i.e. the cross-species interaction range is less then mean of the two same-species interaction ranges, then tumour cells tended to penetrate the healthy regions, whilst (ii) if $R_{12} > \frac{1}{2}(R_{11} + R_{22})$ the tumour cells tend to displace the the healthy cells at the tumour edge, in accordance with the insight gained from studies of mixtures of soft particles [154, 160–163]. Situation (i) is reminiscent of metastasis, whilst (ii) reflects a benign tumour state. Of course, some caution should be applied to such interpretations on the basis of the current analysis, but it is noteworthy that the DDFT approach does identify a potential behavioural property of the cells that can govern benign and virulent tumours. The present work also shows that the overall collective behaviour is sensitive to the details of the pair interactions between cells.

The complex dynamics that the system can exhibit is rather striking. For instance, the drop in the nutrient level observed e.g. in Figs. 6.9–6.11 that then leads to a drop in the overall number of healthy cells, which results in the "crystal" melting temporarily corresponds to the cells being distributed in disordered liquid-like configurations. The nutrient level then recovers and the system "refreezes" and subsequently over time the cancer cells penetrate the healthy tissue and eventually the healthy cells all die out.

Despite the current model being very simplistic in comparison to many models of tumour growth, these initial results demonstrate that DDFT has considerable po-

tential as an effective modelling approach to describe microscale cell-cell interactions that can provide new insights into the dynamics of tissue and tumour growth.

8.2 Future works

The current work is the first to analyse a model using DDFT to describe the growth of tissues and tumours. There is considerable scope to extend the model in order to create a more realistic description of tissue growth. The following areas are included for consideration.

- Instead of considering the pair potential $V_{int}(|\mathbf{r}|) = \varepsilon exp[-(r/R)^4]$ which is used in Sec.4.4, we can use another alternative pair potential models such as that proposed in Ref. [164]. It would be interesting to compare results with those from alternative soft potential models such as that proposed in Ref. [164]. However, in reality there is also attraction (adhesion) between cells, which points to the possibility of the analogue of the gas-liquid or gas-solid phase transitions in collections of cells. Incorporation of both attraction and repulsion between particles in a DFT is straightforward [121–123], but the theory becomes much more elaborate, which is why we avoided such theories for this initial study.

- We can use more sophisticated approximations for the free energy functionals, such as a weighted density functional [123].

- We can use more accurate methods for the time stepping, to solve the system of ODEs (5.5.7) and (5.5.8), such as a Runge–Kutta methods [152].

- Instead of combining birth-death and cell-movement processes, we can use

logistic growth instead of linear birth death term for single species model Eqs. (5.1.1) and (5.1.2). In the case of competition between cancer and healthy cells system of equations (6.1.1), we can use a predator-prey type model for the interacting populations instead of a simple competition interaction. This would be particularly appropriate for describing the interaction between immune cells and cancer cells.

- Instead of considering the pair potential $V_{ij}(|\mathbf{r}-\mathbf{r'}|) = \delta(\mathbf{r}-\mathbf{r'})(\alpha_{ij} - \gamma_{ij}\nabla^2)$ which is used in Sec.7.2, we can use $V_{ij}(r) = \varepsilon_{ij}e^{[-(r/R_{ij})^4]}$, or other pair potential models, to add more biologically realistic description.

- We can extend the preliminary results of chapter 7 to undertake numerical simulations and a parameter survey akin to those discussed in chapter 5 and chapter 6.

- Instead of manually determining the time of cancer penetration in the healthy tissue used in Sec. 6.6, we could develop an algorithm to analyse the cell structure and detect such processes.

APPENDIX A

THE ITO CALCULUS

In order to render this thesis self-contained, we rederive briefly the Ito stochastic differential equations and the Ito formula. A more detailed account can be found in [129]. This allows us to obtain the time evolution equation for the probability distribution function for a "particle" with position x having a fluctuating (i.e. Langevin) equation of motion.

A.1 The Ito stochastic differential equations

A general Langevin equation can be written in the form

$$\frac{dx}{dt} = a(x,t) + b(x,t)\eta(t), \tag{A.1.1}$$

where x is the variable of interest, $a(x,t)$ and $b(x,t)$ are certain known functions and $\eta(t)$ is the rapidly fluctuating random term satisfying $\langle \eta(t) \rangle = 0$ and $\langle \eta(t)\eta(t') \rangle =$

$\delta(t-t^{'})$, where $\langle\cdot\rangle$ denotes a statistical average. The second of these means there is no correlation in the values of $\eta(t)$ at different times. Eq. (A.1.1) must be integrable and hence we have

$$W(t) = \int_0^t dt'\eta(t') \tag{A.1.2}$$

exists. Suppose that $W(t)$ is a continuous function of t, this implies that $W(t)$ is a Markov process. Also, since $W(t)$ is continuous, we must be able to describe $W(t)$ by Wiener process. From Eq. (A.1.2), we obtain

$$dW(t) = W(t+dt) - W(t) = \eta(t)dt, \tag{A.1.3}$$

Now, returning to Eq. (A.1.1), we are in a position to be able to integrate over time, in the manner similar to in Eq. (A.1.3). Doing this we obtain the Ito stochastic differential equation (SDE).

$$dx(t) = a\big[x(t),t\big]dt + b\big[x(t),t\big]dW(t). \tag{A.1.4}$$

A.2 The Ito formula

Consider an arbitrary function of $x(t)$, $f[x(t)]$ and expand $df[x(t)]$ to second order in $dW(t)$:

$$\begin{aligned} df\big[x(t)\big] &= f\big[x(t)+dx(t)\big] - f\big[x(t)\big] \\ &= f'\big[x(t)\big]dx(t) + \frac{1}{2}f''\big[x(t)\big]dx(t)^2 + \cdots \\ &= f'\big[x(t)\big]\Big(a\big[x(t),t\big]dt + b\big[x(t),t\big]dW(t)\Big) \\ &+\frac{1}{2}f''\big[x(t)\big]b\big[x(t),t\big]^2\big[dW(t)\big]^2 + \cdots \end{aligned}$$

where all other terms have been discarded since they are of higher order. by using $\big[dW(t)\big]^2 = dt$ (see the proof in [129]), we obtain

$$\begin{aligned} df\big[x(t)\big] &= \Big\{a\big[x(t),t\big]f'\big[x(t)\big] + \frac{1}{2}b\big[x(t),t\big]^2 f''\big[x(t)\big]\Big\}dt \\ &\quad + b\big[x(t),t\big]f'\big[x(t)\big]dW(t). \end{aligned} \tag{A.2.1}$$

This formula is known as Ito's formula.

To develop Ito's formula for functions of an n dimensional vector $\mathbf{x}(t)$ satisfying SDE

$$d\mathbf{x}(t) = \mathbf{A}(\mathbf{x},t)dt + \mathbf{B}(\mathbf{x},t)d\mathbf{W}(t), \tag{A.2.2}$$

we simply follow the previous procedure. The result is

$$\begin{aligned} df(\mathbf{x}) &= \Big\{\sum_i \mathbf{A}_i(\mathbf{x},t)\frac{\partial f(\mathbf{x})}{\partial x_i} + \frac{1}{2}\sum_{i,j}\big[\mathbf{B}(\mathbf{x},t)\mathbf{B}^T(\mathbf{x},t)\big]_{ij}\frac{\partial^2 f(\mathbf{x})}{\partial x_i \partial x_j}\Big\}dt \\ &\quad + \sum_{i,j}\mathbf{B}_{ij}(\mathbf{x},t)\frac{\partial f(\mathbf{x})}{x_i}dW_j(t). \end{aligned} \tag{A.2.3}$$

A.3 The Fokker–Plank Equation

Consider the time development of an arbitrary $f(x(t))$. Using Ito's formula Eq. (A.2.1)

$$\begin{aligned} \frac{\langle df\big[x(t)\big]\rangle}{dt} &= \left\langle \frac{df\big[x(t)\big]}{dt}\right\rangle = \frac{d}{dt}\langle f\big[x(t)\big]\rangle \\ &= \left\langle \{a\big[x(t),t\big]\frac{\partial f}{\partial x} + \frac{1}{2}b\big[x(t),t\big]^2\frac{\partial^2 f}{\partial x^2}\right\rangle. \end{aligned} \tag{A.3.1}$$

Since $x(t)$ has conditional probability density $P(x,t)$ and

$$\begin{aligned}\frac{d}{dt}\langle f\big[x(t)\big]\rangle &= \int dx f(x)\frac{\partial P}{\partial t} \\ &= \int dx\big[\{a\big[x(t),t\big]\frac{\partial f}{\partial x}+\frac{1}{2}b\big[x(t),t\big]^2\frac{\partial^2 f}{\partial x^2}\big]P(x,t). \quad \text{(A.3.2)}\end{aligned}$$

We integrate by parts (the complete proof in [165]), to obtain

$$\int dx f(x)\frac{\partial P}{\partial t}=\int dx f(x)\Big\{\frac{-\partial[a(x,t)P]}{\partial x}+\frac{1}{2}\frac{\partial^2[b(x,t)^2P]}{\partial x^2}\Big\}. \quad \text{(A.3.3)}$$

and hence, since $f(x)$ is arbitrary,

$$\frac{\partial P(x,t)}{\partial t}=-\frac{\partial[a(x,t)P(x,t)]}{\partial x}+\frac{1}{2}\frac{\partial^2[b(x,t)^2P(x,t)]}{\partial x^2}, \quad \text{(A.3.4)}$$

In general, the Fokker–Planck equation for many variable system of SDE is [129]

$$\frac{\partial P(x,t)}{\partial t}=-\sum_i\frac{\partial\big[\mathbf{A}_i(\mathbf{x},t)P\big]}{\partial x_i}+\frac{1}{2}\sum_{i,j}\frac{\partial^2\big\{\big[\mathbf{B}(\mathbf{x},t)\mathbf{B}^T(\mathbf{x},t)\big]_{ij}P\big\}}{\partial x_i\partial x_j}. \quad \text{(A.3.5)}$$

APPENDIX B

THE SMOLUCHOWSKI EQUATION

In statistical physics, the Fokker–Planck equation is a partial differential equation that describes the time evolution of the probability density function of the positions and velocities of a system particles. The Smoluchowski equation is the Fokker–Planck equation for the probability density function of a system of over-damped Brownian particles [13, 120].

A physically intuitive way of arriving at this equation proceeds as follows [13,120]: For a fluid of N Brownian particles, one imagines applying a force on the particles, where the force on the j^{th} particle is $\mathbf{F}_j = -\nabla_j V(\mathbf{r}^N, t)$, where $\mathbf{r}^N = \{\mathbf{r}_i\}_{i=1,\cdots,N}$ is the set of position coordinates for N particles, so that the system is prevented from relaxing to its equilibrium distribution. The non-equilibrium probability density function in this situation will be:

$$P(\mathbf{r}^N, t) = \frac{1}{Z} \exp[-\beta V(\mathbf{r}^N, t) - \beta U(\mathbf{r}^N, t)], \tag{B.0.1}$$

where Z is a normalisation factor and $U(\mathbf{r}^N, t)$ is the potential energy due to the interparticle interactions and any external potentials influencing the particles are include in U. Taking the gradient of Eq. (B.0.1) we obtain:

$$\mathbf{F}_j = \nabla_j U(\mathbf{r}^N, t) + k_B T \frac{\nabla_j P(\mathbf{r}^N, t)}{P(\mathbf{r}^N, t)}. \tag{B.0.2}$$

for overdamped particles, the velocity of the i^{th} particle is

$$\mathbf{v}_i = -\sum_{j=1}^{N} \Gamma_{ij} \mathbf{F}_j, \tag{B.0.3}$$

where $\Gamma_{ij} = \beta D$ is the mobility coefficient. Since the particle number is conserved, we can expect the fluid to obey the continuity equation:

$$\frac{\partial P(\mathbf{r}^N, t)}{\partial t} = -\sum_{i=1}^{N} \nabla_i \cdot [\mathbf{v}_i P(\mathbf{r}^N, t)]. \tag{B.0.4}$$

Substituting Eqs. (B.0.2) and (B.0.3) into Eq. (B.0.4), we find

$$\frac{\partial P(\mathbf{r}^N, t)}{\partial t} = \sum_{i=1}^{N} \sum_{j=1}^{N} \nabla_i \cdot \Gamma_{ij} [k_B T \ \nabla_j + \nabla_j U(\mathbf{r}^N, t)] P(\mathbf{r}^N, t). \tag{B.0.5}$$

We can replace Γ_{ij} by its "mean-field" value, $\Gamma \delta_{ij}$ and Eq. (B.0.5) reduces to a generalised diffusion equation, termed the Smoluchowski equation:

$$\frac{\partial P(\mathbf{r}^N, t)}{\partial t} = \Gamma \sum_{i=1}^{N} \nabla_i \cdot [k_B T \ \nabla_i + \nabla_i U(\mathbf{r}^N, t)] P(\mathbf{r}^N, t). \tag{B.0.6}$$

BIBLIOGRAPHY

[1] H. Byrne, "Using mathematics to study solid tumour growth," in *Proceedings of the 9th General Meetings of European Women in Mathematics*, pp. 81–107, 2000.

[2] R. Siegel, C. DeSantis, K. Virgo, K. Stein, A. Mariotto, T. Smith, D. Cooper, T. Gansler, C. Lerro, S. Fedewa, *et al.*, "Cancer treatment and survivorship statistics, 2012," *CA: A Cancer Journal for Clinicians*, vol. 62, no. 4, pp. 220–241, 2012.

[3] P. Pisani, F. Bray, and D. M. Parkin, "Estimates of the world-wide prevalence of cancer for 25 sites in the adult population," *International journal of cancer*, vol. 97, no. 1, pp. 72–81, 2002.

[4] R. Araujo and D. McElwain, "A history of the study of solid tumour growth: the contribution of mathematical modelling," *Bulletin of mathematical biology*, vol. 66, no. 5, pp. 1039–1091, 2004.

[5] H. M. Byrned, "Biological lnferences from a mathematical model for malignant invasion," *Invasion Metastasis*, vol. 16, pp. 209–22l, 1996.

[6] R. Sender, S. Fuchs, and R. Milo, "Revised estimates for the number of human and bacteria cells in the body," *PLoS biology*, vol. 14, no. 8, p. e1002533, 2016.

[7] M. A. Chaplain and B. Sleeman, "A mathematical model for the growth and classification of a solid tumor: a new approach via nonlinear elasticity theory using strain-energy functions," *Mathematical biosciences*, vol. 111, no. 2, pp. 169–215, 1992.

[8] R. Weinberg, *The biology of cancer*. Garland science, 2013.

[9] N. Bellomo and P. Maini, "Preface?challenging mathematical problems in cancer modelling," *Mathematical Models and Methods in Applied Sciences*, vol. 17, no. supp01, pp. 1641–1645, 2007.

[10] M. A. Chaplain and G. Lolas, "Mathematical modelling of cancer cell invasion of tissue: The role of the urokinase plasminogen activation system," *Mathematical Models and Methods in Applied Sciences*, vol. 15, no. 11, pp. 1685–1734, 2005.

[11] D. McElwain, R. Callcott, and L. Morris, "A model of vascular compression in solid tumours," *Journal of theoretical biology*, vol. 78, no. 3, pp. 405–415, 1979.

[12] U. M. B. Marconi and P. Tarazona, "Dynamic density functional theory of fluids," *The Journal of chemical physics*, vol. 110, no. 16, pp. 8032–8044, 1999.

[13] A. J. Archer and M. Rauscher, "Dynamical density functional theory for interacting brownian particles: stochastic or deterministic?," *Journal of Physics A: Mathematical and General*, vol. 37, no. 40, p. 9325, 2004.

[14] M. Orme and M. Chaplain, "A mathematical model of vascular tumour growth and invasion," *Mathematical and Computer Modelling*, vol. 23, no. 10, pp. 43–60, 1996.

[15] M. Bálek, V. Bednár, T. Bíly, and M. Karasek, "Microscopic tumor growth module for contracancrum project," in *World Congress on Medical Physics and Biomedical Engineering, September 7-12, 2009, Munich, Germany*, pp. 1957–1960, Springer, 2009.

[16] C. Viallard and B. Larrivée, "Tumor angiogenesis and vascular normalization: alternative therapeutic targets," *Angiogenesis*, pp. 1–18, 2017.

[17] M. A. Chaplain, S. R. McDougall, and A. Anderson, "Mathematical modeling of tumor-induced angiogenesis," *Annu. Rev. Biomed. Eng.*, vol. 8, pp. 233–257, 2006.

[18] H. Byrne and M. A. J. Chaplain, "Growth of nonnecrotic tumors in the presence and absence of inhibitors," *Mathematical biosciences*, vol. 130, no. 2, pp. 151–181, 1995.

[19] R. S. Kerbel, "Tumor angiogenesis: past, present and the near future," *Carcinogenesis*, vol. 21, no. 3, pp. 505–515, 2000.

[20] J. A. Adam, "A simplified mathematical model of tumor growth," *Mathematical biosciences*, vol. 81, no. 2, pp. 229–244, 1986.

[21] A. C. Burton, "Rate of growth of solid tumours as a problem of diffusion.," *Growth*, vol. 30, no. 2, pp. 157–176, 1966.

[22] R. Wasserman, R. Acharya, C. Sibata, and K. Shin, "A patient-specific in vivo tumor model," *Mathematical biosciences*, vol. 136, no. 2, pp. 111–140, 1996.

[23] H. F. Lodish, A. Berk, S. L. Zipursky, P. Matsudaira, D. Baltimore, J. Darnell, *et al.*, *Molecular cell biology*, vol. 4. Citeseer, 2000.

[24] J. P. Ward and J. King, "Mathematical modelling of avascular-tumour growth," *Mathematical Medicine and Biology*, vol. 14, no. 1, pp. 39–69, 1997.

[25] L. A. Kunz-Schughart, M. Kreutz, and R. Knuechel, "Multicellular spheroids: a three-dimensional in vitro culture system to study tumour biology," *International journal of experimental pathology*, vol. 79, no. 1, pp. 1–23, 1998.

[26] W. Mayneord, "On a law of growth of jensen's rat sarcoma," *The American Journal of Cancer*, vol. 16, no. 4, pp. 841–846, 1932.

[27] A. Haddow, "The biological characters of spontaneous tumours of the mouse, with special reference to rate of growth," *The Journal of Pathology and Bacteriology*, vol. 47, no. 3, pp. 553–565, 1938.

[28] A. Hill, "The diffusion of oxygen and lactic acid through tissues," *Proceedings of the Royal Society of London. Series B, Containing Papers of a Biological Character*, pp. 39–96, 1928.

[29] W. Cramer, "The prevention of cancer," *The Lancet*, vol. 223, no. 5758, pp. 1–5, 1934.

[30] L. H. Gray, A. Conger, M. Ebert, S. Hornsey, and O. Scott, "The concentration of oxygen dissolved in tissues at the time of irradiation as a factor in radiotherapy," *The British journal of radiology*, vol. 26, no. 312, pp. 638–648, 1953.

[31] A. K. Laird, "Dynamics of tumour growth," *British journal of cancer*, vol. 18, no. 3, p. 490, 1964.

[32] T. Roose, S. J. Chapman, and P. K. Maini, "Mathematical models of avascular tumor growth," *SIAM review*, vol. 49, no. 2, pp. 179–208, 2007.

[33] J. Ward and J. King, "Mathematical modelling of avascular-tumour growth ii: modelling growth saturation," *Mathematical Medicine and Biology*, vol. 16, no. 2, pp. 171–211, 1999.

[34] J. Ward and J. King, "Mathematical modelling of the effects of mitotic inhibitors on avascular tumour growth," *Computational and Mathematical Methods in Medicine*, vol. 1, no. 4, pp. 287–311, 1999.

[35] J. Ward and J. King, "Modelling the effect of cell shedding on avascular tumour growth," *Computational and Mathematical Methods in Medicine*, vol. 2, no. 3, pp. 155–174, 2000.

[36] H. Greenspan, "Models for the growth of a solid tumor by diffusion," *Stud. Appl. Math*, vol. 51, no. 4, pp. 317–340, 1972.

[37] J. A. Adam, "A mathematical model of tumor growth. ii. effects of geometry and spatial nonuniformity on stability," *Mathematical Biosciences*, vol. 86, no. 2, pp. 183–211, 1987.

[38] J. A. Adam, "A mathematical model of tumor growth by diffusion," *Mathematical and Computer Modelling*, vol. 11, pp. 455–456, 1988.

[39] J. Adam and S. Maggelakis, "Mathematical models of tumor growth. iv. effects of a necrotic core," *Mathematical biosciences*, vol. 97, no. 1, pp. 121–136, 1989.

[40] J. Casciari, S. Sotirchos, and R. Sutherland, "Mathematical modelling of microenvironment and growth in emt6/ro multicellular tumour spheroids," *Cell proliferation*, vol. 25, no. 1, pp. 1–22, 1992.

[41] A. Deakin, "Model for the growth of a solid in vitro tumor.," *Growth*, vol. 39, no. 1, pp. 159–165, 1975.

[42] D. McElwain and P. Ponzo, "A model for the growth of a solid tumor with non-uniform oxygen consumption," *Mathematical Biosciences*, vol. 35, no. 3-4, pp. 267–279, 1977.

[43] R. Shymko and L. Glass, "Cellular and geometric control of tissue growth and mitotic instability," *Journal of Theoretical biology*, vol. 63, no. 2, pp. 355–374, 1976.

[44] H. Byrne and M. A. Chaplain, "Free boundary value problems associated with the growth and development of multicellular spheroids," *European Journal of Applied Mathematics*, vol. 8, no. 6, pp. 639–658, 1997.

[45] S. Cui and A. Friedman, "A free boundary problem for a singular system of differential equations: an application to a model of tumor growth," *Transactions of the American Mathematical Society*, vol. 355, no. 9, pp. 3537–3590, 2003.

[46] G. Pettet, C. Please, M. Tindall, and D. McElwain, "The migration of cells in multicell tumor spheroids," *Bulletin of Mathematical Biology*, vol. 63, no. 2, pp. 231–257, 2001.

[47] J. A. Sherratt, "Traveling wave solutions of a mathematical model for tumor encapsulation," *SIAM Journal on Applied Mathematics*, vol. 60, no. 2, pp. 392–407, 2000.

[48] J. A. Sherratt, "Cellular growth control and travelling waves of cancer," *SIAM Journal on Applied Mathematics*, vol. 53, no. 6, pp. 1713–1730, 1993.

[49] J. A. Sherratt and M. A. Chaplain, "A new mathematical model for avascular tumour growth," *Journal of mathematical biology*, vol. 43, no. 4, pp. 291–312, 2001.

[50] S. Tohya, A. Mochizuki, S. Imayama, and Y. Iwasa, "On rugged shape of skin tumor (basal cell carcinoma)," *Journal of theoretical biology*, vol. 194, no. 1, pp. 65–78, 1998.

[51] M. A. Chaplain, M. Ganesh, and I. G. Graham, "Spatio-temporal pattern formation on spherical surfaces: numerical simulation and application to solid tumour growth," *Journal of mathematical biology*, vol. 42, no. 5, pp. 387–423, 2001.

[52] B. Marchant, J. Norbury, and J. Sherratt, "Travelling wave solutions to a haptotaxis-dominated model of malignant invasion," *Nonlinearity*, vol. 14, no. 6, p. 1653, 2001.

[53] A. Anderson, M. Chaplain, E. Newman, R. Steele, and A. Thompson, "Mathematical modelling of tumour invasion and metastasis," *Computational and mathematical methods in medicine*, vol. 2, no. 2, pp. 129–154, 2000.

[54] W. Düchting and T. Vogelsaenger, "Recent progress in modelling and simulation of three-dimensional tumor growth and treatment," *Biosystems*, vol. 18, no. 1, pp. 79–91, 1985.

[55] A.-S. Qi, X. Zheng, C.-Y. Du, and B.-S. An, "A cellular automaton model of cancerous growth," *Journal of theoretical biology*, vol. 161, no. 1, pp. 1–12, 1993.

[56] A. R. Kansal, S. Torquato, G. Harsh Iv, E. Chiocca, and T. Deisboeck, "Simulated brain tumor growth dynamics using a three-dimensional cellular automaton," *Journal of theoretical biology*, vol. 203, no. 4, pp. 367–382, 2000.

[57] A. Kansal, S. Torquato, E. Chiocca, and T. Deisboeck, "Emergence of a subpopulation in a computational model of tumor growth," *Journal of Theoretical Biology*, vol. 207, no. 3, pp. 431–441, 2000.

[58] E. L. Stott, N. F. Britton, J. A. Glazier, and M. Zajac, "Stochastic simulation of benign avascular tumour growth using the potts model," *Mathematical and Computer Modelling*, vol. 30, no. 5-6, pp. 183–198, 1999.

[59] J. Smolle and H. Stettner, "Computer simulation of tumour cell invasion by a stochastic growth model," *Journal of Theoretical Biology*, vol. 160, no. 1, pp. 63–72, 1993.

[60] D. Drasdo, S. Dormann, S. Hoehme, and A. Deutsch, "Cell-based models of avascular tumor growth," in *Function and Regulation of Cellular Systems*, pp. 367–378, Springer, 2004.

[61] N. Bellomo and L. Preziosi, "Modelling and mathematical problems related to tumor evolution and its interaction with the immune system," *Mathematical and Computer Modelling*, vol. 32, no. 3-4, pp. 413–452, 2000.

[62] N. Bellomo, A. Bellouquid, and E. De Angelis, "The modelling of the immune competition by generalized kinetic (boltzmann) models: Review and research perspectives," *Mathematical and Computer Modelling*, vol. 37, no. 1-2, pp. 65–86, 2003.

[63] D. Drasdo and S. Höhme, "Individual-based approaches to birth and death in avascu1ar tumors," *Mathematical and Computer Modelling*, vol. 37, no. 11, pp. 1163–1175, 2003.

[64] Y. Mansury, M. Kimura, J. Lobo, and T. S. Deisboeck, "Emerging patterns in tumor systems: simulating the dynamics of multicellular clusters with an agent-based spatial agglomeration model," *Journal of Theoretical Biology*, vol. 219, no. 3, pp. 343–370, 2002.

[65] S. Turner and J. A. Sherratt, "Intercellular adhesion and cancer invasion: a discrete simulation using the extended potts model," *Journal of theoretical biology*, vol. 216, no. 1, pp. 85–100, 2002.

[66] C. Chen, H. Byrne, and J. King, "The influence of growth-induced stress from the surrounding medium on the development of multicell spheroids," *Journal of mathematical biology*, vol. 43, no. 3, pp. 191–220, 2001.

[67] W.-Y. Chen, P. R. Annamreddy, and L. Fan, "Modeling growth of a heterogeneous tumor," *Journal of theoretical biology*, vol. 221, no. 2, pp. 205–227, 2003.

[68] R. Wette, I. Katz, and E. Rodin, "Stochastic processes for solid tumor kinetics i. surface-regulated growth," *Mathematical Biosciences*, vol. 19, no. 3-4, pp. 231–255, 1974.

[69] N. V. Mantzaris, S. Webb, and H. G. Othmer, "Mathematical modeling of tumor-induced angiogenesis," *Journal of mathematical biology*, vol. 49, no. 2, pp. 111–187, 2004.

[70] H. A. Levine, B. D. Sleeman, and M. Nilsen-Hamilton, "Mathematical modeling of the onset of capillary formation initiating angiogenesis," *Journal of Mathematical Biology*, vol. 42, no. 3, pp. 195–238, 2001.

[71] H. A. Levine, B. D. Sleeman, and M. Nilsen-Hamilton, "A mathematical model for the roles of pericytes and macrophages in the initiation of angiogenesis. i. the role of protease inhibitors in preventing angiogenesis," *Mathematical biosciences*, vol. 168, no. 1, pp. 77–115, 2000.

[72] A. Anderson and M. A. Chaplain, "A mathematical model for capillary network formation in the absence of endothelial cell proliferation," *Applied mathematics letters*, vol. 11, no. 3, pp. 109–114, 1998.

[73] A. R. Anderson and M. Chaplain, "Continuous and discrete mathematical models of tumor-induced angiogenesis," *Bulletin of mathematical biology*, vol. 60, no. 5, pp. 857–899, 1998.

[74] M. A. Chaplain, "Mathematical modelling of angiogenesis," *Journal of neuro-oncology*, vol. 50, no. 1-2, pp. 37–51, 2000.

[75] M. Holmes and B. Sleeman, "A mathematical model of tumour angiogenesis incorporating cellular traction and viscoelastic effects," *Journal of theoretical biology*, vol. 202, no. 2, pp. 95–112, 2000.

[76] C. L. Stokes and D. A. Lauffenburger, "Analysis of the roles of microvessel endothelial cell random motility and chemotaxis in angiogenesis," *Journal of theoretical biology*, vol. 152, no. 3, pp. 377–403, 1991.

[77] P. Hahnfeldt, D. Panigrahy, J. Folkman, and L. Hlatky, "Tumor development under angiogenic signaling: a dynamical theory of tumor growth, treatment response, and postvascular dormancy," *Cancer research*, vol. 59, no. 19, pp. 4770–4775, 1999.

[78] C. J. Breward, H. M. Byrne, and C. E. Lewis, "A multiphase model describing vascular tumour growth," *Bulletin of mathematical biology*, vol. 65, no. 4, pp. 609–640, 2003.

[79] C. Lewis, "A multiphase model describing vascular tumour growth," 2003.

[80] P. A. Netti, L. T. Baxter, Y. Boucher, R. Skalak, and R. K. Jain, "Macro- and microscopic fluid transport in living tissues: Application to solid tumors," *AIChE journal*, vol. 43, no. 3, pp. 818–834, 1997.

[81] E. Ruoslahti, "How cancer spreads," *Scientific American*, vol. 275, no. 3, pp. 72–78, 1996.

[82] L. A. Liotta, J. Kleinerman, and G. M. Saidel, "Quantitative relationships of intravascular tumor cells, tumor vessels, and pulmonary metastases following tumor implantation," *Cancer research*, vol. 34, no. 5, pp. 997–1004, 1974.

[83] L. A. Liotta, J. Kleinerman, and G. M. Saldel, "The significance of hematogenous tumor cell clumps in the metastatic process," *Cancer research*, vol. 36, no. 3, pp. 889–894, 1976.

[84] L. A. Liotta, G. M. Saidel, and J. Kleinerman, "Diffusion model of tumor vascularization and growth," *Bulletin of mathematical biology*, vol. 39, no. 1, pp. 117–128, 1977.

[85] A. Perumpanani and H. Byrne, "Extracellular matrix concentration exerts selection pressure on invasive cells," *European Journal of Cancer*, vol. 35, no. 8, pp. 1274–1280, 1999.

[86] A. Perumpanani and J. Norbury, "Numerical interactions of random and directed motility during cancer invasion," *Mathematical and computer modelling*, vol. 30, no. 7-8, pp. 123–133, 1999.

[87] R. A. Gatenby, "Models of tumor-host interaction as competing populations: implications for tumor biology and treatment," *Journal of theoretical biology*, vol. 176, no. 4, pp. 447–455, 1995.

[88] R. A. Gatenby, "The potential role of transformation-induced metabolic changes in tumor-host interaction," *Cancer research*, vol. 55, no. 18, pp. 4151–4156, 1995.

[89] R. A. Gatenby and E. Gawlinski, "Mathematical models of tumour invasion mediated by transformation-induced alteration of microenvironmental ph," in

Novartis Foundation Symposium, pp. 85–95, Chichester; New York; John Wiley; 1999, 2001.

[90] S. D. Webb, J. A. Sherratt, and R. G. Fish, "Alterations in proteolytic activity at low ph and its association with invasion: a theoretical model," *Clinical & experimental metastasis*, vol. 17, no. 5, pp. 397–407, 1999.

[91] T. Alarcon, H. Byrne, and P. Maini, "Towards whole-organ modelling of tumour growth," *Progress in biophysics and molecular biology*, vol. 85, no. 2-3, pp. 451–472, 2004.

[92] T. Alarcón, H. M. Byrne, and P. K. Maini, "A multiple scale model for tumor growth," *Multiscale Modeling & Simulation*, vol. 3, no. 2, pp. 440–475, 2005.

[93] R. Betteridge, M. R. Owen, H. M. Byrne, T. Alarcón, and P. K. Maini, "The impact of cell crowding and active cell movement on vascular tumour growth," *Networks and heterogeneous media*, vol. 1, no. 4, pp. 515–535, 2006.

[94] H. M. Byrne, M. R. Owen, T. Alarcon, and P. K. Maini, "Cancer disease: integrative modelling approaches," in *Biomedical Imaging: Nano to Macro, 2006. 3rd IEEE International Symposium on*, pp. 806–809, IEEE, 2006.

[95] H. M. Byrne, M. R. Owen, T. Alarcon, J. Murphy, and P. K. Maini, "Modelling the response of vascular tumours to chemotherapy: a multiscale approach," *Mathematical Models and Methods in Applied Sciences*, vol. 16, no. supp01, pp. 1219–1241, 2006.

[96] C. Deroulers, M. Aubert, M. Badoual, and B. Grammaticos, "Modeling tumor cell migration: from microscopic to macroscopic models," *Physical Review E*, vol. 79, no. 3, p. 031917, 2009.

[97] L. Zhang, C. A. Athale, and T. S. Deisboeck, "Development of a three-dimensional multiscale agent-based tumor model: simulating gene-protein interaction profiles, cell phenotypes and multicellular patterns in brain cancer," *Journal of theoretical biology*, vol. 244, no. 1, pp. 96–107, 2007.

[98] C. Athale, Y. Mansury, and T. S. Deisboeck, "Simulating the impact of a molecular ?decision-process? on cellular phenotype and multicellular patterns in brain tumors," *Journal of theoretical biology*, vol. 233, no. 4, pp. 469–481, 2005.

[99] B. M. Rubenstein and L. J. Kaufman, "The role of extracellular matrix in glioma invasion: a cellular potts model approach," *Biophysical journal*, vol. 95, no. 12, pp. 5661–5680, 2008.

[100] R. M. Sutherland, J. A. McCredie, and W. R. Inch, "Growth of multicell spheroids in tissue culture as a model of nodular carcinomas," *Journal of the National Cancer Institute*, vol. 46, no. 1, pp. 113–120, 1971.

[101] L. Glass, "Instability and mitotic patterns in tissue growth," *Journal of Dynamic Systems, Measurement, and Control*, vol. 95, no. 3, pp. 324–327, 1973.

[102] W. Bullough, "Mitotic and functional homeostasis: a speculative review," *Cancer Research*, vol. 25, no. 10, pp. 1683–1727, 1965.

[103] J. S. Lowengrub, H. B. Frieboes, F. Jin, Y. Chuang, X. Li, P. Macklin, S. Wise, and V. Cristini, "Nonlinear modelling of cancer: bridging the gap between cells and tumours," *Nonlinearity*, vol. 23, no. 1, p. R1, 2009.

[104] P. S. Kim, P. P. Lee, and D. Levy, "A pde model for imatinib-treated chronic myelogenous leukemia," *Bulletin of mathematical biology*, vol. 70, no. 7, p. 1994, 2008.

[105] K. D. Miller, R. L. Siegel, C. C. Lin, A. B. Mariotto, J. L. Kramer, J. H. Rowland, K. D. Stein, R. Alteri, and A. Jemal, "Cancer treatment and survivorship statistics, 2016," *CA: a cancer journal for clinicians*, vol. 66, no. 4, pp. 271–289, 2016.

[106] J. P. Ward and J. R. King, "Mathematical modelling of drug transport in tumour multicell spheroids and monolayer cultures," *Mathematical biosciences*, vol. 181, no. 2, pp. 177–207, 2003.

[107] C. Chen and J. P. Ward, "A mathematical model of the growth of uterine myomas," *Bulletin of mathematical biology*, vol. 76, no. 12, pp. 3088–3121, 2014.

[108] A. Pierres, A. Benoliel, and P. Bongrand, "Cell-cell interactions," *Physical chemistry of biological interfaces*, pp. 459–522, 2000.

[109] M. J. Piotrowska and S. D. Angus, "A quantitative cellular automaton model of in vitro multicellular spheroid tumour growth," *Journal of theoretical biology*, vol. 258, no. 2, pp. 165–178, 2009.

[110] A. R. Anderson, "A hybrid mathematical model of solid tumour invasion: the importance of cell adhesion," *Mathematical medicine and biology: a journal of the IMA*, vol. 22, no. 2, pp. 163–186, 2005.

[111] J. A. Engelberg, G. E. Ropella, and C. A. Hunt, "Essential operating principles for tumor spheroid growth," *BMC systems biology*, vol. 2, no. 1, p. 110, 2008.

[112] X. Gao, J. T. McDonald, L. Hlatky, and H. Enderling, "Cell-cell interactions in solid tumors?the role of cancer stem cells," in *New Challenges for Cancer Systems Biomedicine*, pp. 191–204, Springer, 2012.

[113] D. Drasdo and S. Höhme, "A single-cell-based model of tumor growth in vitro: monolayers and spheroids," *Physical biology*, vol. 2, no. 3, p. 133, 2005.

[114] J. Galle, M. Hoffmann, and G. Aust, "From single cells to tissue architecture?a bottom-up approach to modelling the spatio-temporal organisation of complex multi-cellular systems," *Journal of mathematical biology*, vol. 58, no. 1-2, p. 261, 2009.

[115] J. Jeon, V. Quaranta, and P. T. Cummings, "An off-lattice hybrid discrete-continuum model of tumor growth and invasion," *Biophysical journal*, vol. 98, no. 1, pp. 37–47, 2010.

[116] S. Turner, J. A. Sherratt, and D. Cameron, "Tamoxifen treatment failure in cancer and the nonlinear dynamics of tgfβ," *Journal of theoretical biology*, vol. 229, no. 1, pp. 101–111, 2004.

[117] A. F. Marée, V. A. Grieneisen, and P. Hogeweg, "The cellular potts model and biophysical properties of cells, tissues and morphogenesis," *Single-cell-based models in biology and medicine*, pp. 107–136, 2007.

[118] A. Shirinifard, J. S. Gens, B. L. Zaitlen, N. J. Popławski, M. Swat, and J. A. Glazier, "3d multi-cell simulation of tumor growth and angiogenesis," *PloS one*, vol. 4, no. 10, p. e7190, 2009.

[119] A. Chauviere, H. Hatzikirou, I. G. Kevrekidis, J. S. Lowengrub, and V. Cristini, "Dynamic density functional theory of solid tumor growth: preliminary models," *AIP advances*, vol. 2, no. 1, p. 011210, 2012.

[120] A. J. Archer and R. Evans, "Dynamical density functional theory and its application to spinodal decomposition," *The Journal of chemical physics*, vol. 121, no. 9, pp. 4246–4254, 2004.

[121] R. Evans, "The nature of the liquid-vapour interface and other topics in the statistical mechanics of non-uniform, classical fluids," *Advances in Physics*, vol. 28, no. 2, pp. 143–200, 1979.

[122] R. Evans, "Density functionals in the theory of nonuniform fluids," *Fundamentals of inhomogeneous fluids*, vol. 1, pp. 85–176, 1992.

[123] J.-P. Hansen and I. R. McDonald, *Theory of Simple Liquids: With Applications to Soft Matter*. Academic Press, 2013.

[124] F. Mandal, *Statistical physics*. John Wiley & Sons Ltd., 2 ed., 1971.

[125] J. Sethna, *Statistical mechanics: entropy, order parameters, and complexity*, vol. 14. Oxford University Press, 2006.

[126] R. Evans, "Density functionals in the theory of nonuniform fluids," *Fundamentals of inhomogeneous fluids*, vol. 1, pp. 85–176, 1992.

[127] R. M. Mazo, "On the theory of brownian motion. iii. two-body distribution function," *Journal of Statistical Physics*, vol. 1, no. 4, pp. 559–562, 1969.

[128] J. Deutch and I. Oppenheim, "Molecular theory of brownian motion for several particles," *The Journal of Chemical Physics*, vol. 54, no. 8, pp. 3547–3555, 1971.

[129] C. W. Gardiner, "Handbook of stochastic methods for physics, chemistry and the natural sciences," *Applied Optics*, vol. 25, p. 3145, 1986.

[130] H. Frusawa and R. Hayakawa, "On the controversy over the stochastic density functional equations," *Journal of Physics A: Mathematical and General*, vol. 33, no. 15, p. L155, 2000.

[131] P.-H. Chavanis, "Hamiltonian and brownian systems with long-range interactions: V. stochastic kinetic equations and theory of fluctuations," *Physica A: Statistical Mechanics and its Applications*, vol. 387, no. 23, pp. 5716–5740, 2008.

[132] A. J. Archer, B. Chacko, and R. Evans, "The standard mean-field treatment of inter-particle attraction in classical dft is better than one might expect," *The Journal of chemical physics*, vol. 147, no. 3, p. 034501, 2017.

[133] J. E. Darnell, H. F. Lodish, D. Baltimore, *et al.*, *Molecular cell biology*, vol. 2. Scientific American Books New York, 1990.

[134] C. N. Likos, "Effective interactions in soft condensed matter physics," *Physics Reports*, vol. 348, no. 4, pp. 267–439, 2001.

[135] D. A. Lenz, R. Blaak, C. N. Likos, and B. M. Mladek, "Microscopically resolved simulations prove the existence of soft cluster crystals," *Physical review letters*, vol. 109, no. 22, p. 228301, 2012.

[136] C. N. Likos, "Soft matter with soft particles," *Soft matter*, vol. 2, no. 6, pp. 478–498, 2006.

[137] B. M. Mladek, M. Fernaud, G. Kahl, and M. Neumann, "On the thermodynamic properties of the generalized gaussian core model," *Condensed Matter Physics*, 2005.

[138] I. Götze, H. Harreis, and C. Likos, "Tunable effective interactions between dendritic macromolecules," *The Journal of chemical physics*, vol. 120, no. 16, pp. 7761–7771, 2004.

[139] C. Likos and H. Harreis, "Star polymers: From conformations to interactions to phase diagrams," *Condensed Matter Physics*, 2002.

[140] A. Louis, P. Bolhuis, R. Finken, V. Krakoviack, E. Meijer, and J. Hansen, "Coarse-graining polymers as soft colloids," *Physica A: Statistical Mechanics and its Applications*, vol. 306, pp. 251–261, 2002.

[141] J. Dzubiella, A. Jusufi, C. Likos, C. von Ferber, H. Löwen, J. Stellbrink, J. Allgaier, D. Richter, A. Schofield, P. Smith, *et al.*, "Phase separation in star-polymer–colloid mixtures," *Physical Review E*, vol. 64, no. 1, p. 010401, 2001.

[142] A. Jusufi, J. Dzubiella, C. Likos, C. Von Ferber, and H. Löwen, "Effective interactions between star polymers and colloidal particles," *Journal of Physics: Condensed Matter*, vol. 13, no. 28, p. 6177, 2001.

[143] P. N. Werahera, L. M. Glode, F. G. La Rosa, M. S. Lucia, E. D. Crawford, K. Easterday, H. T. Sullivan, R. S. Sidhu, E. Genova, and T. Hedlund,

"Proliferative tumor doubling times of prostatic carcinoma," *Prostate cancer*, vol. 2011, 2011.

[144] J. Sherwood, F. Stagnitti, M. Kokkinn, and W. Williams, "A standard table for predicting equilibrium dissolved oxygen concentrations in salt lakes dominated by sodium chloride," *International Journal of Salt Lake Research*, vol. 1, no. 1, pp. 1–6, 1992.

[145] C. M. O'Connor, J. U. Adams, and J. Fairman, "Essentials of cell biology," *Cambridge: NPG Education*, 2010.

[146] P. J. Mohr, B. N. Taylor, and D. B. Newell, "Codata recommended values of the fundamental physical constants: 2010a)," *Journal of Physical and Chemical Reference Data*, vol. 41, no. 4, p. 043109, 2012.

[147] K. F. Riley, M. P. Hobson, and S. J. Bence, *Mathematical methods for physics and engineering: a comprehensive guide*. Cambridge university press, 2006.

[148] R. Courant and D. Hilbert, *Methods of mathematical physics [Methoden der mathematischen Physik, engl.] 1*. CUP Archive, 1965.

[149] A. J. Archer, M. Walters, U. Thiele, and E. Knobloch, "Solidification in soft-core fluids: Disordered solids from fast solidification fronts," *Physical Review E*, vol. 90, no. 4, p. 042404, 2014.

[150] A. C. Hindmarsh, "Odepack, a systematized collection of ode solvers," *Scientific computing*, pp. 55–64, 1983.

[151] A. C. Hindmarsh, "Serial fortran solvers for ode initial value problems," *URL: http://www. llnl. gov/CASC/odepack [cited October 18, 2005]*, 2002.

[152] R. L. Burden and J. D. Faires, "Numerical analysis. 2001," *Brooks/Cole, USA*, 2001.

[153] A. J. Archer, "Dynamical density functional theory: binary phase-separating colloidal fluid in a cavity," *Journal of Physics: Condensed Matter*, vol. 17, no. 10, p. 1405, 2005.

[154] A. Archer and R. Evans, "Binary gaussian core model: Fluid-fluid phase separation and interfacial properties," *Physical Review E*, vol. 64, no. 4, p. 041501, 2001.

[155] M. Derenzini, D. Trere, A. Pession, L. Montanaro, V. Sirri, and R. L. Ochs, "Nucleolar function and size in cancer cells.," *The American journal of pathology*, vol. 152, no. 5, p. 1291, 1998.

[156] A. J. Archer, M. C. Walters, U. Thiele, and E. Knobloch, "Generation of defects and disorder from deeply quenching a liquid to form a solid," in *Mathematical Challenges in a New Phase of Materials Science*, pp. 1–26, Springer, 2016.

[157] J. L. Willems, *Stability theory of dynamical systems*. Nelson, 1970.

[158] A. J. Archer, A. Rucklidge, and E. Knobloch, "Quasicrystalline order and a crystal-liquid state in a soft-core fluid," *Physical review letters*, vol. 111, no. 16, p. 165501, 2013.

[159] M. Marušic, Ž. Bajzer, S. Vuk-Pavlovic, and J. P. Freyer, "Tumor growthin vivo and as multicellular spheroids compared by mathematical models," *Bulletin of mathematical biology*, vol. 56, no. 4, pp. 617–631, 1994.

[160] A. Archer, C. Likos, and R. Evans, "Soft-core binary fluid exhibiting a λ-line and freezing to a highly delocalized crystal," *Journal of Physics: Condensed Matter*, vol. 16, no. 23, p. L297, 2004.

[161] I. Götze, A. J. Archer, and C. Likos, "Structure, phase behavior, and inhomogeneous fluid properties of binary dendrimer mixtures," *The Journal of chemical physics*, vol. 124, no. 8, p. 084901, 2006.

[162] A. Archer, C. Likos, and R. Evans, "Binary star-polymer solutions: bulk and interfacial properties," *Journal of Physics: Condensed Matter*, vol. 14, no. 46, p. 12031, 2002.

[163] S. Overduin and C. Likos, "Phase behaviour in binary mixtures of ultrasoft repulsive particles," *EPL (Europhysics Letters)*, vol. 85, no. 2, p. 26003, 2009.

[164] D. Drasdo, S. Hoehme, and M. Block, "On the role of physics in the growth and pattern formation of multi-cellular systems: What can we learn from individual-cell based models?," *Journal of Statistical Physics*, vol. 128, no. 1-2, pp. 287–345, 2007.

[165] M. Lefebvre, *Applied stochastic processes*. Springer Science & Business Media, 2007.